EVLA Memo 211
VLA Subreflector Alignment

Rick Perley, Ken Sowinski, Lucas Wilkins, and Sydney Andersen

June 29, 2021

Abstract

The VLA antennas' vertical axis primary beam response at high frequencies strongly degrades with decreasing elevation due primarily to an increasing misalignment of the subreflector with respect to the primary. The elevation dependence of the degradation has been measured using the holographic scanning modes. The VLA's offset cassegrain optics permits an effective cancellation of this degradation for feeds located near to the elevation axis by an elevation-dependent rotation of the subreflector. New coefficients for the rotation are determined and implemented, resulting in a considerable improvement of the forward gain and beam symmetry at all elevations for the high frequency bands. A prescription for quickly measuring offsets, using a single vertical cut, is provided for future adjustments.

1 Introduction

The VLA's antennas were designed for good performance below ∼15 GHz. Prior to 1990, with light observing pressure on the VLA's original Ku and K band receivers, there was little incentive to improve high frequency performance. With the installation of the Q-band receivers in the mid 1990s, and especially after the implementation of new high frequency wideband receivers brought by the EVLA Project, interest in, and use of, the high frequency receiver bands has greatly increased. These upgrades have required numerous changes in order to enable the VLA antennas to operate adequately at frequencies more than three times higher than that they were designed for.

Broadly speaking, these changes were in three areas: First, the antenna pointing was improved with implementation of a 'referenced pointing' regimen. In good weather conditions, this has allowed pointing accurate to ∼4 arcseconds, sufficient for most Q-band observing. Second, the antenna surfaces were adjusted using antenna holography, doubling the antenna efficiency at Q-band to ∼ 30%. High frequency antenna efficiency is now primarily limited by the panel accuracy. An EVLA Memorandum describing this program will be released soon. The third area of development, and the subject of this memo, is an improvement of the VLA antenna optics, primarily through improved alignment of the subreflector and feeds.

High fidelity synthesis imaging requires stable primary beams. In general, but especially for arrays designed for synthesis observing, azimuthally symmetric antenna beams which retain their characteristics over a wide elevation range are an important characteristic if computationally expensive post-processing of the data is to be avoided. Holographic images made of the VLA's antenna beams at the high frequency bands show that they become increasingly asymmetric along the vertical axis, with a large coma lobe developing on the upper side at low elevations. This is primarily the result of misaligned optics – the subreflector and/or feeds are not correctly positioned with respect to the main reflector. The sensitivity of the antenna beam shape to small misalignments is very high – millimeter-scale errors in subreflector positioning will cause significant primary beam shape asymmetry and gain loss at the highest frequencies now used by the VLA. Gaining the maximum benefit from the VLA's high frequency receivers requires well-aligned and stable optics.

Small alignment errors primarily affect the lower power levels of the primary beam. Most notably, such errors dramatically affect the strength and shape of the antenna sidelobes. The relative heights of the innermost pair of sidelobes of an antenna is an extremely sensitive measure of the optical misalignment of the system. Measurement of these sidelobes through orthogonal beam cuts provides an efficient and effective way of determining and correcting optics misalignments.

In this memo, we show that the vertical degradation of the beam, as quantified by the ratio of the power levels of the innermost sidelobes, is proportional to both the frequency and the cosine of the elevation, $\cos E$. We then show that the offset cassegrain optical design of the VLA permits effective cancellation of this degradation by an elevation-dependent rotation of the subreflector for feeds located near the horizontal axis.. For feeds located off the horizontal axis, this rotation introduces an elevation-dependent horizontal degradation. We derive an expression for the rotation which minimizes the net beam degradation.

The coefficients describing these effects are determined, and an improved implementation of the counter-rotation is described. Examples of the remarkable improvement in beam gain and profile due to this rotation are shown. A discussion of the possible origins of the beam degradation, based on the Ruze theory of small optics perturbations, concludes the memo.

2 The Elevation Dependency of the Primary Beam Shape

Pointing and holographic beamshape observations of the VLA antennas show two related changes as functions of elevation:

1. The beam center points to a lower elevation than commanded due to the torque from the weight of the quad legs, focus assembly, and subreflector not being fully offset by that of the counterweight. This mispointing has a $\cos E$ dependence whose coefficient is determined through regular pointing observations. The correction – less than one arcminute – is included in the antenna pointing model.

2. The shape of the primary beam becomes increasingly distorted along the vertical axis as the antenna elevation decreases. This is likely due to an increasing misalignment of the subreflector w.r.t. the primary reflector – caused either by a vertical displacement, or by a rotation ('tilt'), of the subreflector about a horizontal axis. While any pointing offset generated by the subreflector motion is absorbed into the pointing model correction, the distortion remains.

To illustrate these distortions, we show in Fig 1 normalized horizontal and vertical profile cuts, without any subreflector rotation, through the primary beam of ea07 at C, X, and Ku bands at four elevations, including one with the antenna pointed 'over the top' – i.e., $E > 90$. These beam profiles are made with the VLA's holography functions, which are described in detail in the soon-to-be-released holography memo. The top panels show the horizontal cuts at C band (left), X band (middle) and Ku band (right). The four elevations are color coded – low in black, middling in red, high in green, and blue for observations with the antenna 'over the top'. The lower panels show the data for the elevation cuts. Immediately apparent is that the horizontal beam profiles are nearly identical for all elevations at all three bands – differences are less than 1 dB, even at Ku-band. In contrast, the elevation cuts show a very strong dependency in the size of the inner sidelobes on elevation. Even at C-band, there is a change of more than 6 dB in the ratio of the innermost sidelobes between highest and lowest elevations. At Ku-band, the change in power ratio between the sidelobes between zenith and horizon is typically 15 dB. Note that despite the dramatic change in sidelobe structure, there is little change in the main beam profiles, at least above the -10 dB level – and hence little change in forward gain. However, this apparent independence does not remain true at the higher frequencies, where the distortions are many times worse. At Q-band, the effects are strong enough to decrease the forward gain by 50% or more at low elevations, with an accompanying significant distortion of the primary beamshape.

To quantify the beam distortion, we define a metric based on the ratio of the powers in the two innermost sidelobes. We call this the SideLobe Ratio – 'SLR', denoted hereinafter as S_ν, and define it as the power ratio, expressed in decibels, of these sidelobes. When the beam profiles are given in dB, the SLR is the difference of the peaks of the two sidelobes. The SLR is considered positive for the vertical cuts when the sidelobe on the upper side of the beam is greater than that on the lower and, for horizontal cuts, when the sidelobe on the right (higher azimuth) side (as seen from behind) is greater than the left.

Examination of the vertical profiles shown in Figure 1 shows that, for all antennas, a closely linear relation exists between the SLR and both $\cos E$ and observing frequency. An example is shown in the left panel of Figure 2, where the frequency-normalized SLRs $S = S_\nu/\nu_G$, where ν_G is the frequency in GHz, for antenna ea14 at C, X and Ku bands are shown plotted against $\cos E$. For the three bands shown, and over the entire elevation range of the antenna (8 to 120 degrees), the SLR is closely linear with $\cos E$, with the same (frequency-normalized) slope. Most antennas show equally good fits – those that do not are discrepant only for elevations greater than 90 degrees at Ku-band, where the sidelobe ratio exceeds 12 dB. Averaged over all antennas, the mean slope coefficients are -1.09, -1.05, and -1.03 dB/GHz at C, X, and Ku bands, respectively.

The linearity between the SLR and $\cos E$ shown in these measurements suggests a relation given by:

$$S = V_{90} - K\nu_G \cos E \qquad (1)$$

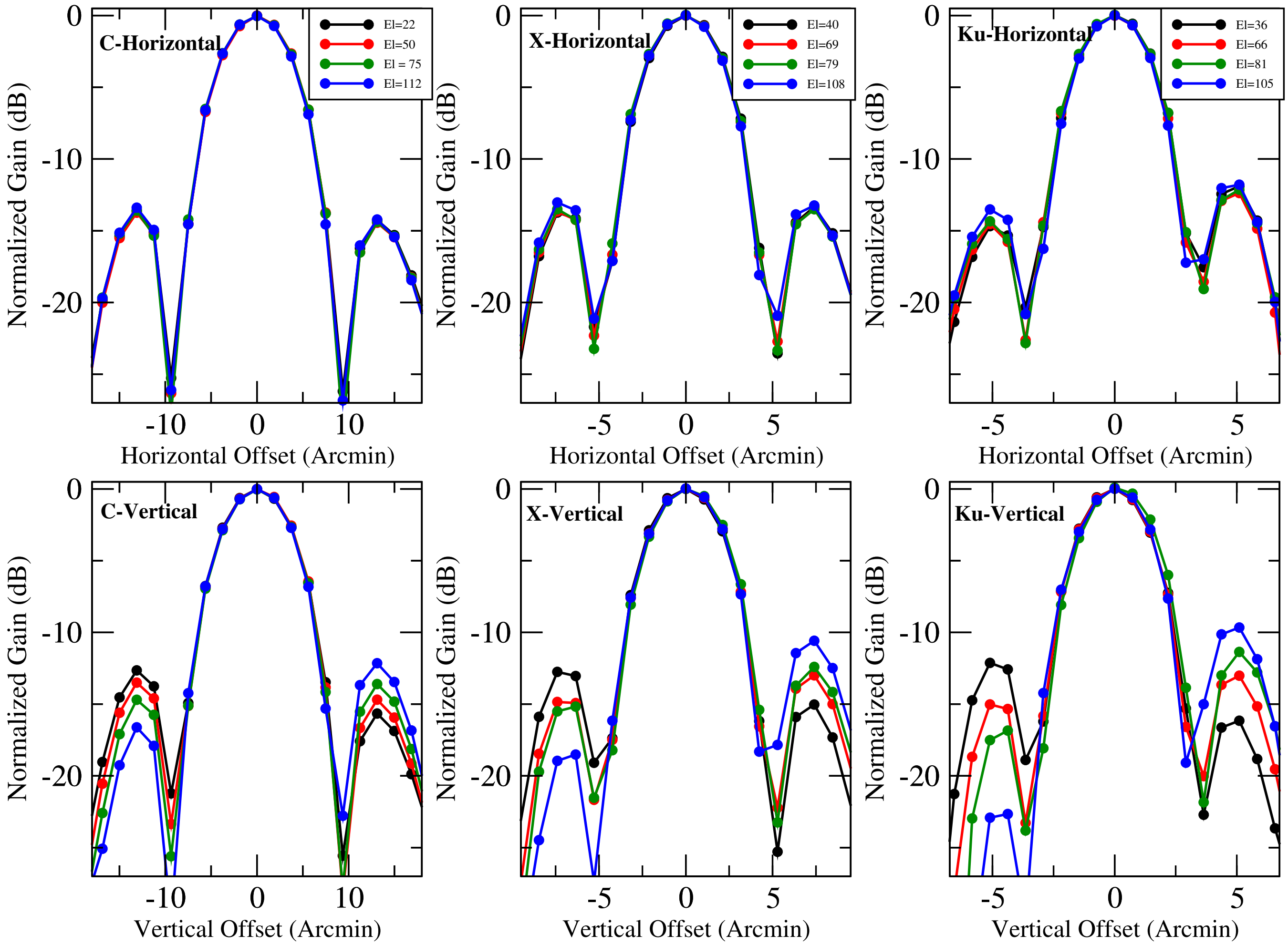

Figure 1: Normalized rrthogonal cuts through the beam of ea07 at C, X, and Ku bands, with no subreflector rotation applied, at four elevations. The horizontal cuts are shown in the top row, the vertical cuts in the bottom row. C-band cuts are on the left, X-band in the middle, Ku-band on the right. The four elevations include one at $E > 90$, shown in blue. The antenna beam shapes are very stable in the horizontal direction, but have a strong dependency on elevation in the vertical.

where $K = K_\nu/\nu_G$ is the frequency-normalized slope coefficient with a value close to 1.05 dB/GHz, and V_{90} is the SLR, at the frequency of interest, in the vertical cut at an elevation of 90 degrees. The choice of sign in equation 1 ensures that the slope coefficient K is positive. The linear relation is valid over a range of about -15 to +15 dB, outside of which it is both non-linear and difficult to measure as the weaker sidelobe disappears. Note that as the antenna points to lower elevations, the vertical profiles show an increasingly negative SLR – the large coma lobe is on the lower side of the main beam, and becomes larger as the elevation decreases.

Despite the lopsidedness of the observed profiles at the low power levels, the forward gain loss is small at the bands shown in the figure. The simulations reported on later in this memo indicate that the forward gain losses associated with the asymmetric beams are $\sim$ 1.5, 5.2, and 7.1% for 5, 10, and 15 dB sidelobe ratios, respectively[1]. From this, we can conclude that, for observations at frequencies up to 15 GHz, the effect of the beam asymmetry on observations is minor, and can normally be ignored. However, this is not so at the higher frequency bands, where gain losses of over 50% are expected, and observed.

2.1 Subreflector Counter-Rotation

In the early 1990s, with the implementation of the new Q-band (40 – 50 GHz) receiver system then underway, Peter Napier pointed out that the elevation-induced vertical beam distortion and gain loss could be offset by rotating the subreflector. This rotation induces a similar beam distortion to that due to a change in elevation,

[1]The loss of forward gain is difficult to measure directly, as different sources, whose flux densities are not accurately known, were used for these observations.

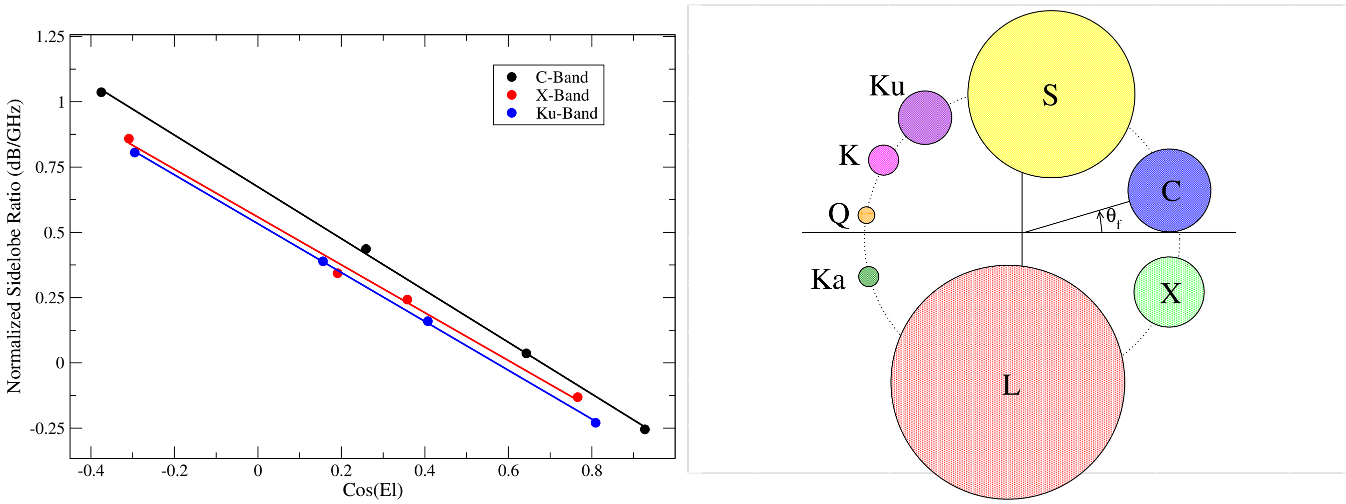

Figure 2: **Left** The frequency-normalized SideLobe Ratio $S = S_\nu/\nu_G$ for ea14 is a linear function of the both the cosine of elevation and the observing frequency. The slopes shown here are $-0.99, -0.92$ and -0.94 dB/GHz, for C, X, and Ku bands, respectively. **Right** The VLA's Cassegrain feed layout, as viewed from behind the antenna, looking outwards. The three highest frequency feeds are positioned close to the horizontal axis, allowing effects of subreflector misalignment to be offset by rotating the subreflector. The azimuth angle of the feed, θ_f is defined w.r.t the horizontal ('x') axis as shown for the C-band feed.

but along a direction orthogonal to the azimuth location of the feed on the cassegrain feed ring. Thus, for feeds positioned on or near the horizontal sides of the Cassegrain feed ring, the effect of an elevation-induced beam distortion can be largely removed by a suitable counter-rotation of the subreflector. Although this rotation changes the antenna's pointing, the relation between beam throw and rotation is easily determined, and can be utilized to accurately re-point the antenna. The Q-band feeds were subsequently mounted on the horizontal axis, and this method successfully implemented in January, 1996. This simple correction dramatically improved the Q-band performance at low elevations.

The method could not be applied to the existing K-band feed at that time, as this feed was mounted near the top of the feed ring. At this position, subreflector rotation has no vertical component, so the elevation-dependent asymmetry cannot be offset. However, with the EVLA project (starting in 2002 and completed in 2012) came new receivers and a new feed layout. All four high frequency bands (Ku, K, Ka, and Q) now have their receivers mounted on the left side of the secondary focus ring (as viewed from behind), allowing the implementation of subreflector rotation for all these bands. The EVLA feed layout is shown in the right panel of Fig. 2.

3 Beam Asymmetries Induced by Subreflector Rotation

The VLA antennas employ an offset cassegrain optics system. The subreflector is shaped so that the secondary focus is located at a radius of 1.05 m from the antenna axis. The motivation for this was to simplify changing frequency bands – rather than having to rotate the receivers to position the feeds at an on-axis secondary focus, the subreflector rotates the focal spot to illuminate the desired feeds, which are located around the focal ring.

As noted above, for feeds located near the elevation axis, the elevation-dependent beam distortions can be largely offset by a suitable counter-rotation of the subreflector along with a repointing of the antenna. The implemenation of this scheme requires determination of the pointing offsets and dependence of beam distortion as a function of subreflector rotation position.

3.1 Measuring the Asymmetry Dependency on Rotation

To determine the parameters describing the effects that rotation of the subreflector has on the primary beam properties, we developed a measurement regimen which took orthogonal beam cuts with the subreflector in three positions: (a) a small CW rotation by $-\Delta\phi$, (b) zero rotation, and (c) a small CCW rotation by $+\Delta\phi$. We adopt a convention that the sense of rotation is defined by looking outwards, and that a CCW rotation is positive. The small increment in rotation $\Delta\phi$ varied by observing band: 3.0, 1.5, 1.0, 0.75, and 0.5 degrees at X, Ku, K, Ka, and Q bands, respectively. From the three orthogonal beam cut pairs, we determined the rate of change of beam asymmetry as a function of rotation, the beam asymmetry with zero rotation, and the pointing offsets caused by the rotation. The first two inform us of the rotation required to offset the elevation-induced asymmetry, the last is used to correct the pointing.

Observations in this three-rotation mode were taken in the summers of 2017, 2018, and 2019, as shown in Table 1. This mode of observing was developed in July 2017, and the data taken that year were mostly for debugging the implementation. The vast majority of the useable data was taken in the following two summers.

Table 1: **Observing Log for 3-Rotation Measurements**

Date	Bands	RefAnt	El	Nature	Target	Conf	Comments
10-Aug-2017	X	3 4 9	55	3-Rot	3C273	C	Test of 3-Rot
11-Aug-2017	X	3 4 9	53	3-Rot	3C345	C	Test of 3-Rot
15-Aug-2017	U K	3 4 8	45	3-Rot	3C345	C	
17-Aug-2017	A Q	3 4 9	49	3-Rot	3C345	C	Incomplete
01-Jun-2018	U K	3 4 9	56	3-Rot	3C273	A	
02-Jun-2018	A Q	3 4 9	45	3-Rot	3C273	A	
07-Jun-2018	U Q	5 9 19	78	3-Rot	BLLac	A	
08-Jun-2018	K A	5 9 19	78	3-Rot	BLLac	A	
09-Jun-2018	U K	5 9 19	18	3-Rot	J0217	A	
10-Jun-2018	A	5 9 19	18	3-Rot	J0217	A	
11-Jun-2018	Q	5 9 19	18	3-Rot	J0217	A	
11-Sep-2018	U	3 4 9	43 52	3-Rot	3C273	A	
28-May-2019	K	5 9 19	49	3-Rot	J0217	B	
30-May-2019	U K	5 9 19	45	3-Rot	J0217	B	
30-May-2019	K	3 4 9	18 77	3-Rot	J0217,3C286	B	
31-May-2019	U	3 4 9	86	3-Rot	3C286	B	
01-Jun-2019	K	3 4 9	22	3-Rot	3C345	B	
01-Jun-2019	A	9 12 19	57 83	3-Rot	3C273,3C286	B	
03-Jun-2019	Q	9 12 19	22 57 84	3-Rot	3C345,3C273,3C286	B	
04-Jun-2019	Q	9 12 19	34 40	3-Rot	3C84,J1927	B	
06-Jun-2019	A	9 12 19	30	3-Rot	3C345	B	
07-Jun-2019	A	9 12 19	54 70	3-Rot	3C273,3C286	B	
19-Jun-2019	K	3 6 14	62	3-Rot	BLLac	B	
20-Jun-2019	K	3 6 16	50	3-Rot	BLLac	B	
21-Jun-2019	A	5 9	80	3-Rot	BLLac	B	
24-Jun-2019	A	3 6 16	26 49 77	3-Rot	J1153 J1927 BLLac	B	
24-Jun-2019	Q	3 6 16	68	3-Rot	3C84	B	
25-Jun-2019	Q	3 6 16	26 49 77	3-Rot	J1153,J1927,BLLac	B	
03-Jul-2019	K	3 6 16	23 71	3-Rot	3C84,3C454.3,BLLac	BnA	Rotation Off

Examples of the beam profiles produced by the three-angle regimen are shown in Figure 3 for three elevations, taken on ea12 at K-band. The upper row shows the azimuth cuts, the lower row the elevation cuts. Within each panel, the cuts for the three rotation values are color coded: black, red, and blue traces show the profiles with the subreflector rotated by -1, 0 and +1 degree, respectively, from the nominal position, where a positive value means a CCW rotation, as seen from behind.

It will be noted that there are elevation-dependent changes in both axes of the beam profiles shown here, while in Figure 1, the changes are seen in only the vertical axis. The reason for this that the profiles shown in Figure 1 are made with no subreflector counter-rotation, and thus represent the true elevation-dependent distortions. On the other hand, the profiles shown in Figure 3 were taken with the original implemenation of the elevation-dependent subreflector rotation applied which, as explained below, used a coefficient about half of the correct value. Hence, the elevation-dependent changes in asymmetry seen in the elevation profiles between the three columns represent the residual after about half of the actual elevation dependence is removed. The small elevation-dependent asymmetries seen in the azimuth cuts between the three columns are due to the rotation that has been applied to reduce the elevation distortion dependency, as the K-band feed is located at an angle of ~ 20 degrees from the horizontal axis. Thus, for feeds located off the elevation axis, the rotation applied to reduce the elevation dependency inevitably creates a horizontal beam distortion with an elevation dependency. Balancing these distortions is discussed at length in Section 3.2

Examination of the plots shows that for the high frequency bands, which are located on the left side of the

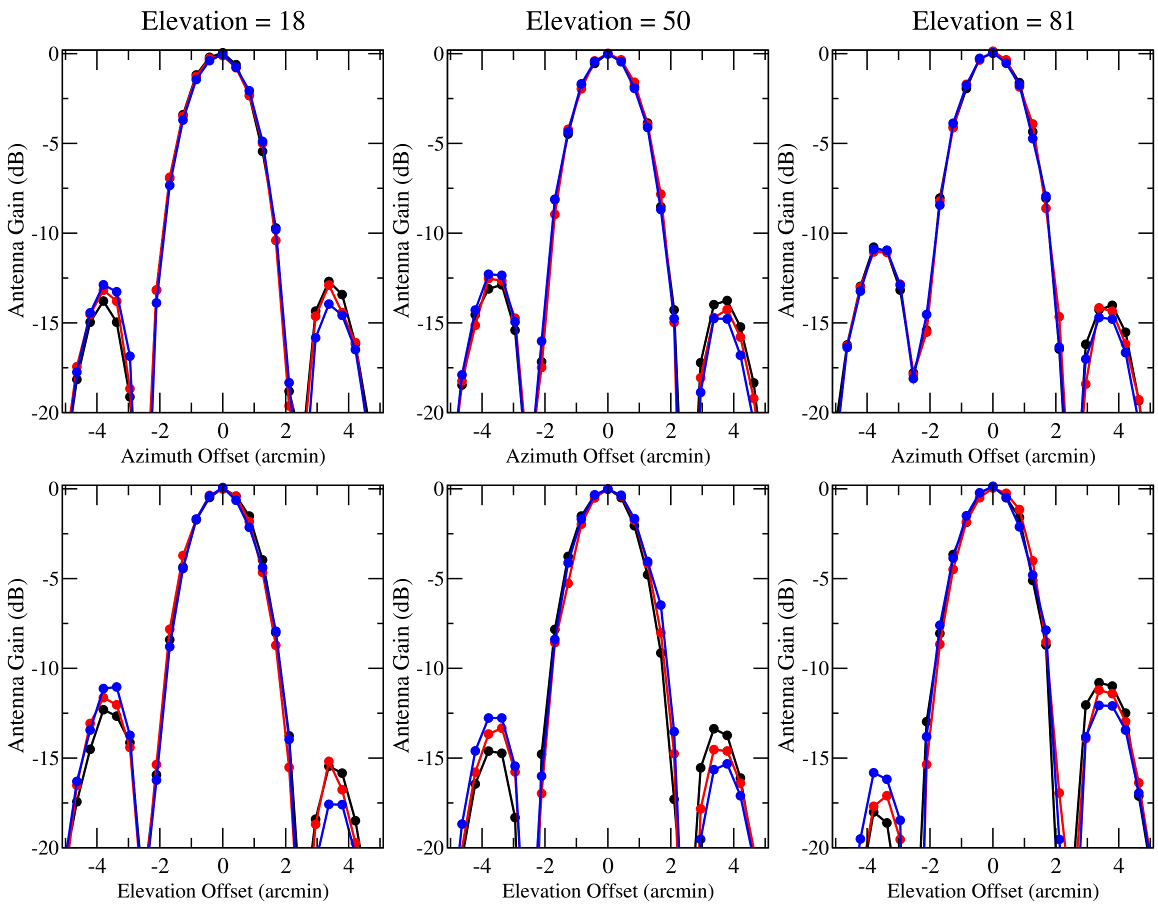

Figure 3: Results from the subreflector three-angle rotation observations for ea12 at K-band. The top row shows the azimuth cuts, the bottom row the elevation cuts. The left, center, and right columns show the cuts at 18, 50 and 81 degrees. The black, red, and blue traces show the cuts with -1, 0, and +1 degree subreflector rotation, respectively. Note that a positive subreflector rotation corresponds to a counter-clockwise rotation, as viewed from behind the antenna, looking outwards. A negative slope in the sidelobes indicates the subreflector is rotated too far counter-clockwise, a positive slope indicates the subreflector is rotated too far clockwise.

cassegrain feed ring (as viewed from behind), a negative subreflector rotation (i.e., a CW change) causes the SLR to become more positive – the higher-elevation sidelobe increases in strength. Hence, as an antenna is pointed to lower elevations, causing the SLR to become more negative, a negative (CW) rotation of the subreflector will offset the elevation-induced asymmetry. For feeds located on the opposite side of the feed ring (C and X bands), a positive (CCW) rotation is required to offset the increasing SLR with decreasing elevation.

3.1.1 Three-Rotation Calibration Results

As described above, the three-rotation measurements allow measurement of the rate of change of SLR with rotation. As the feeds are located in different azimuths around the feed ring, the beam distortions will be seen in both elevation and azimuth cuts, with a ratio given by the tangent of the feed azimuth.

Accurately determining these coefficients required many observations, as the great majority of these were taken in summertime, and in the extended (A and B) configurations – a combination which generally ensures poor phase stability. Additionally, we often utilized weak calibrators for the low elevation cuts, resulting in poor SNR for much of the high frequency data. To improve accuracy, and to allow an estimate of the measurement errors, 10 to 14 observations were taken at each of the high frequency bands, as shown in Table 1.

From each three-angle triplet, the rate of change of SLR with subreflector rotation was estimated for both horizontal and vertical cuts, and the results averaged over all observations for all antennas. The results from this are given in Table 2. The key results are shown in columns 3, 4, and 5. Column 5 gives the rate of change with angle in the normalized SLR in dB/(deg·GHz). As expected, there is good consistency in the values over

Table 2: **Conversion Constants for SLR Measurements**

Band	$\Delta\phi$	Az Coef	El Coef	NormRotCoef	Feed Az	RotConv	OffConv
	Deg	dB/Deg	dB/deg	dB/(GHz·deg)	Deg	Deg·GHz/dB	cm·GHz/dB
X	3.0	$0.32 \pm .02$	$0.81 \pm .01$	$0.104 \pm .002$	-22	9.62	5.15
Ku	1.5	$-1.01 \pm .01$	$-1.06 \pm .02$	$0.103 \pm .002$	136	9.71	5.20
K	1.0	$-0.88 \pm .02$	$-1.70 \pm .04$	$0.098 \pm .003$	152	10.2	5.36
Ka	0.75	$1.06 \pm .04$	$-2.68 \pm .09$	$0.089 \pm .003$	201	11.2	5.99
Q	0.5	–	$-4.27 \pm .12$	$0.102 \pm .003$	180	9.80	5.24

the bands, except at Ka-band, where the value is 10% lower than the others. No clear explanation has been found. The average over the highest three frequencies, which we adopt in the following discussion, is $L = 0.095$ dB/(GHz·deg). L is the rotation coefficient, and is band-independent. With the SLR and angle definitions defined earlier, the horizontal and vertical changes in the rotation-induced SLR for a given frequency band are given by

$$\delta S_H = -L_\nu \phi \sin\theta_f \quad (2)$$

$$\delta S_V = L_\nu \phi \cos\theta_f \quad (3)$$

where θ_f is the feed azimuth, and $L_\nu = L\nu_G$ is the frequency-dependent rotation coefficient. Note that for the Ku, K, and Q band feeds, a positive subreflector rotation induces a negative increase in both axes of the beam profiles, while for the X-band feed, a positive rotation induces a positive increase in both beam axes.

The three-angle observations were taken over a wide range of elevations, allowing a search for a dependence of the rotation coefficient on elevation. None was found.

These data give us another way of estimating the feed azimuth. The ratio of the horizontal and vertical SLR ratios (columns 3 and 4 in the table) will directly depend on the azimuth location of the feed, since the direction of rotation is orthogonal to the feed azimuth radius. The derived azimuths are given in the sixth column of the table, and are in good agreement with the EVLA project book values shown in the following table. There is no azimuth offset measurement at Q-band – this feed is only six degrees from the horizontal axis, and the SNR of the observations at this band was not sufficient to detect the small horizontal motion resulting from the small rotation of the subreflector.

Two additional useful constants are given in the 7th and 8th columns. The former – simply the inverse of the coefficient L – allows conversion of any individual SLR observation to the rotation required to remove the observed imbalance, while the latter converts this rotation to the equivalant offset in the feed position. This last value is derived from the known radius of the cassegrain focal ring.

3.1.2 Beam Throw Results

The relation between subreflector rotation and antenna pointing offset ('beam throw') was derived from the results of the referenced pointing solutions determined for each of the orthogonal beam cut measurements. The value of the small rotation, $\Delta\phi$, chosen for each band, must be large enough to generate an appreciable change in the SLR, yet small enough that the beam throw due to the rotation is not larger than that which can be measured by the referenced pointing[2]. These offset pointing solutions can also be used to determine another independent measure of the feed location on the secondary focal ring, as the ratio of the offsets in azimuth and elevation are determined by the tangent of the feed location angle w.r.t. the horizontal axis.

The referenced pointing solutions from the observations were averaged over all antennas, and the results are displayed in Table 3.

The key value is in the far right column – the beam pointing is moved by 0.58 arcminutes per degree of subreflector rotation, $\sim 5\%$ higher than the value of 0.5537 currently utilized by the on-line software. We are considering observations to check which of these values is correct. The azimuth and elevation components of the beam throw are determined by the position of the feed around the secondary focus ring. For feeds located in the second quadrant (Ku, K, and Q), a positive rotation (CCW) moves the beam to the right (higher azimuth) and up – all directions again defined from behind, looking outwards. Also shown are the derived azimuths of

[2] At Ka and Q bands, due to the additional global antenna pointing errors, the pointing offsets can exceed the maximum offset that referenced pointing can solve for. For these bands, the script included an initial scan, utilizing referenced pointing at X-band, with the appropriate rotation applied with opposite sign (because the X-band feed is located on the opposite side of the feed ring).

Table 3: **Beam Throw as a Function of Subreflector Rotation**

Band	Increment	Az Offset	El Offset	Angle	PB Angle	Beam Throw	
	Degrees	Arcmin	Arcmin	Degrees	Degrees	Arcmin	Arcmin/Deg
Ku	1.5	0.670	0.565	130	132	0.876	0.587
K	1.0	0.282	0.510	151	154	0.582	0.582
Ka	0.75	-0.117	0.410	196	197	0.426	0.568
Q	0.5	0.026	0.295	175	175	0.296	0.592

the feeds (fifth column), determined from the ratio of the observed horizontal and vertical offsets. These are in excellent agreement with those defined the EVLA Project Book (sixth column).

3.2 Minimizing the Beam Asymmetry

The subreflector rotation required to cancel the elevation-induced asymmetry can be made via straightforward analysis. In the following it is assumed that a zero sidelobe imbalance represents the optimum alignment which gives the maximum forward gain and primary beam symmetry.

3.2.1 One-Dimensional Analysis

We first analyze the simplest geometry – in which the feed lies on the horizontal axis, so that $\theta_f = 0$ or 180 degrees. In this case, only the vertical asymmetry component need be considered. In the following, to avoid repetitive appearance of the frequency term, we do the analysis using the frequency dependent coefficients $K_\nu = \nu_G K$ and $L_\nu = \nu_G L$.

From the observations, we know that the (vertical) SLR varies with elevation as

$$S(E) = V_{90} - K_\nu \cos(E) \tag{4}$$

where V_{90} is the observed sidelobe asymmetry at E = 90, and K_ν is the frequency-dependent elevation slope coefficient, equal to $\sim 1.05\nu_G$ dB. This distortion is solely in the vertical direction, and is of a sense that the lower elevation sidelobe grows as the elevation decreases – the SLR decreases as $\cos E$ increases.

The results of the three-angle measurements indicate that the SLR varies linearly with rotation ϕ as

$$S(E, \phi) = S(E, 0) + L_\nu \phi \tag{5}$$

where $L_\nu = 0.095\nu_G$ dB/deg is the frequency-dependent coefficient for the SLR with rotation. (The sign of the second term on the RHS is appropriate for a feed on the right side of the focal ring, for which $\cos\theta_f > 0$. It is negated for a feed on the opposite side.) $S(E, 0)$ is the sidelobe asymmetry at a given elevation with the subreflector in its nominal (zero-rotation) position.

Equations 4 and 5 are then combined to give the variation in asymmetry as a function of elevation and rotation:

$$S(E, \phi) = V_{90} - K_\nu \cos(E) + L_\nu \phi \tag{6}$$

We desire to balance the sidelobes at all elevations, so set $S(E, \phi) = 0$. This results in

$$\phi = \frac{K_\nu}{L_\nu}\cos E - \frac{V_{90}}{L_\nu} \tag{7}$$

The required rotation ϕ consists of a rotation offset, $\phi_0 = -V_{90}/L_\nu$, which balances the sidelobes at the reference elevation $E = 90$, and an elevation-dependent rotation $\Delta\phi = K_\nu \cos E/L_\nu$ which maintains the balance at other elevations. The ratio $K_\nu/L_\nu = \chi$ is the full subreflector rotation between $E = 90$ and $E = 0$. As both K_ν and L_ν are linearly dependent on frequency, the ratio χ is frequency-independent. With the values of K and L determined earlier, we find that $\chi \sim 11$ degrees.

3.2.2 Two-Dimensional Analysis

The preceding analysis is appropriate for feeds on the horizontal axis, for which $\theta_f = 0$ or 180. Only the Q-band feed is sufficiently close to the horizontal axis for this analysis to apply. For those bands with feeds significantly off the horizontal axis, we must include both the effect of the subreflector rotation on the horizontal beam asymmetry, and on the reduction of the asymmetry offset in the vertical component due to the rotation.

The simplest approach would be to apply the preceding analysis, taking into account the angle θ_f, describing the location of the feed around the feed ring. The result is

$$\phi = \left(\frac{K_\nu}{L_\nu}\cos E - \frac{V_{90}}{L_\nu}\right)\sec\theta_f \tag{8}$$

– the required rotation is increased by a factor of $\sec\theta_f$ for feeds off the horizontal axis. Although this rotation will indeed remove the vertical asymmetry, it will also increase the horizontal asymmetry, due to the horizontal component of the rotation, which scales with $\sin\theta_f$. For feeds more than 45 degrees away from the horizontal, the induced horizontal motion is greater than the vertical, so that the reduction in vertical asymmetry is more than offset by an increase in horizontal asymmetry. Clearly, an optimized rotation must include both components.

To analyze this situation, we write for the vertical and horizontal sidelobe ratios:

$$\begin{aligned} S_V(E,\phi) &= V_{90} - K_\nu\cos(E) + L_\nu\phi\cos\theta_f && (9)\\ S_H(\phi) &= H_{90} - L_\nu\phi\sin\theta_f && (10)\end{aligned}$$

where V_{90} and H_{90} are the measured (frequency-dependent) sidelobe asymmetries, without rotation, at the zenith in the vertical and horizontal cuts, and K_ν and L_ν are the frequency-dependent elevation and rotation asymmetry slope coefficients.

The horizontal and vertical asymmetries can be considered the cartesian components of a circular asymmetry function: $S^2 = S_V^2 + S_H^2$. The rotation angle ϕ_{opt} corresponding to the minimum asymmetry in S is found by setting the derivative $dS/d\phi = 0$. The resulting optimum rotation is given by

$$\phi_{opt} = \chi\cos\theta_f\cos E + \frac{H_{90}}{L_\nu}\sin\theta_f - \frac{V_{90}}{L_\nu}\cos\theta_f \tag{11}$$

which reduces to eqn 7 for $\theta_f = 0$.

The optimum rotation again comprises two parts – an offset value $\phi_0 = (H_{90}\sin\theta_f - V_{90}\cos\theta_f)/L_\nu$, and an elevation dependent term $\Delta\phi = \chi\cos\theta_f\cos E$. As expected, the optimum rotation for feeds off the horizontal axis is reduced, by a factor of $\cos^2\theta_f$, from that value appropriate for a full negation of the elevation asymmetry. We must accept a less than perfect cancellation of the vertical asymmetry in order to prevent an excessive increase in the horizontal asymmetry caused by the subreflector rotation.

Substituting the optimum rotation expression into the asymmetry equations (9) and (10) provides us with an expression giving the minimum asymmetry as a function of elevation, with the optimum rotation applied:

$$S'_{min} = V_{90}\sin\theta_f + H_{90}\cos\theta_f - K_\nu\sin\theta_f\cos E \tag{12}$$

where the prime indicates a post-correction value. It can be shown that the minimum asymmetry is always less than that which occurs with no correction:

$$S_{nocor} = \sqrt{(V_{90} - K_\nu\cos E)^2 + H_{90}^2} \tag{13}$$

so that, even for feeds located far off the horizontal axis, the application of the subreflector rotation given by equation (11) is always beneficial in reducing the sidelobe asymmetry. However, note that the efficacy of the counter-rotation is much reduced for feeds located more than ~ 30 degrees from the horizontal axis.

The offset rotation ϕ_0 changes the values of the zenith offsets to

$$\begin{aligned} V'_{90} &= V_{90}\sin^2\theta_f + H_{90}\cos\theta_f\sin\theta_f && (14)\\ H'_{90} &= V_{90}\cos\theta_f\sin\theta_f + H_{90}\cos^2\theta_f && (15)\end{aligned}$$

With these new offsets, the observed vertical and horizontal offsets are given by:

$$\begin{aligned} S'_V &= V'_{90} - K_\nu\sin^2\theta_f\cos E && (16)\\ S'_H &= H'_{90} - K_\nu\sin\theta_f\cos\theta_f\cos E && (17)\end{aligned}$$

Note that, except for feeds on the horizontal axis, the resulting vertical and horizontal profiles are functions of elevation.

Equation 12 also shows that for a feed on the horizontal axis, $S_{min} = H_{90}$ – the vertical asymmetry is exactly removed, leaving only the horizontal component, and that for a feed on the vertical axis, $S_{min} = V_{90} - K_\nu\cos E$ – the horizontal asymmetry is exactly removed, leaving the vertical component unchanged.

3.2.3 Vertical Minimization at a Fiducial Elevation

The preceding analysis presumes that the horizontal zenith asymmetry H_{90} is a fixed quantity. However, this need not be true, as a horizontal offset of the subreflector or feed will change the beam profile. There is thus the likelihood that this asymmetry can be reduced by translation of the subreflector or feed. This subject is discussed in a later section.

During the course of this investigation, it was realized that the rotation coefficient which had been employed for many years – and which was utilized in our observations – was too low by more than a factor of two – the value used was $\chi_0 = 5.2$ degrees, while the initial results from our investigations clearly indicated that a value $\chi \sim 11$ is correct. The use of the smaller coefficient resulted in a much reduced efficacy of the correction, particularly at low elevations.

In July 2019, with the issue of how to manage the horizontal offset unresolved, and the need to utilize the correct rotation coefficient and offset for science observing, we elected to implement an alternate correction method which ignores the horizontal offset. This method utilizes the optimal elevation dependency of the rotation derived above, and sets the rotation offset such that the vertical asymmetry is zero at a fiducial elevation of $E = 60$, a value chosen as it lies halfway between the zenith and horizon in the projected $\cos E$ coordinate. The rationale was that implementing this 'quick fix' would reasonably optimize the elevation portion of the asymmetry, allowing us to address the horizontal component at a later time. There is nothing preventing subsequent implemenation of the formally optimal solution given in equation 11. It is to be noted that implementation of the subreflector rotation parameters is done in software and is hence straightforwards to implement, while physical offsets of the subreflector or feeds is a complicated procedure, executed by the antenna crew, and involving many individuals.

In the following, the analysis is done for vertical beam symmetry at a fiducial elevation E_0. In this approach, we express the applied rotation as

$$\phi = \chi \cos\theta_f \cos E + \phi_o \tag{18}$$

where ϕ_o is the rotation required to balance the resulting vertical asymmetry (only) at the fiducial elevation of $E = E_0$. Substitution of Eq 18 into Eq 9, and setting $S_V = 0$ when $E = E_0$ gives

$$\phi_o = (\chi \sin^2\theta_f \cos E_0 - V_{90}/L_\nu) \sec\theta_f . \tag{19}$$

With this offset, the residual elevation and azimuth asymmetries become

$$\begin{aligned} S'_V &= K_\nu \sin^2\theta_f (\cos E_0 - \cos E) && (20)\\ S'_H &= H_{90} + \tan\theta_f [V_{90} - K_\nu(\sin^2\theta_f \cos E_0 + \cos^2\theta_f \cos E)] && (21) \end{aligned}$$

A reasonable optimum reference elevation is $E_0 = 60$, as this balances the asymmetries about the mean value of $\cos E$. With this reference elevation, the residual vertical asymmetry has a maximum amplitude, at E = 0 and 90, of $K_\nu \sin^2\theta_f/2$. The residual horizontal offset at E = 60 has the curious value of $H_{90} + (V_{90} - K_\nu)\tan\theta_f$. The horizontal asymmetry diverges at large feed azimuth since there is in general no value of ϕ_o which permits balancing of the vertical profiles.

By defining new zenith offset values:

$$\begin{aligned} V'_{90} &= K_\nu \sin^2\theta_f \cos E_0 && (22)\\ H'_{90} &= H_{90} + \tan\theta_f (V_{90} - K_\nu \sin^2\theta_f \cos E_0) && (23) \end{aligned}$$

the resulting beam profiles have the same form as with the 'optimum' rotation:

$$\begin{aligned} S'_V &= V'_{90} - K_\nu \sin^2\theta_f \cos E && (24)\\ S'_H &= H'_{90} - K_\nu \sin\theta_f \cos\theta_f \cos E && (25) \end{aligned}$$

as expected, as both methods use the same cosine-dependent rotation correction.

3.2.4 Vertical Minimization with No Elevation-Dependent Rotation

There is a third optimization option. At the lower frequency bands (C, and X), the beam asymmetries are modest, and it may be considered sufficient to not employ the subreflector rotation mechanism at all. However, sidelobe balance at a central reference elevation E_0 is still desirable. For this, a simple offset rotation is required. Analysis shows that the rotation is

$$\phi_f = (\chi \cos E_0 - V_{90}/L_\nu) \sec\theta_f . \tag{26}$$

With this correction, the resulting horizontal and vertical residual asymmetries are

$$S'_V = K_\nu(\cos E_0 - \cos E) \tag{27}$$

$$S'_H = H_{90} + \tan\theta_f(V_{90} - K_\nu \cos E_0) \tag{28}$$

As in the preceding case, at the optimum elevation of $E_0 = 60$, the maximum vertical asymmetry is $K_\nu/2$, seen at E = 90 and E = 0. Note that this residual is always larger by a factor of $\csc^2\theta_f$ than that obtained by optimizing about $E_0 = 60$ with the elevation-dependent correction turned on. The horizontal asymmetry can be worsened by the application of this correction, due to the addition of the term in $\tan\theta_f$, and depending on the amplitude of the vertical offset V_{90}.

3.3 Illustrating Q and Ku Band Relations

The effectiveness of the subreflector rotation is a strong function of feed azimuth and the horizontal and vertical offsets, H_{90} and V_{90}. The dependency on the vertical offset can be discounted, as the zero-point rotation offset will normally be employed to balance the vertical profiles about the fiducial elevation. Implementing this offset changes the horizontal offsets, however – whether this improves or degrades the overall balance depends on the magnitude and sign of the horizontal offset. Given our decision to defer action on the horizontal offsets until after implementation of the offsets to balance the vertical profiles, the following illustrations, which assume balanced vertical profiles, is appropriate.

We show here two plots to illustrate the effect of the horizontal offsets for two bands – Q-band, whose feed is only 5 degrees from the horizontal, and Ku-band, where the feed is located 44 degrees from the horizontal. Both plots show the residual asymmetries with three values of the horizontal offset – one at zero and two others of opposite sign, and magnitude equal to about the largest that we actually see.

In Fig. 4 we show the residual SLR values at Q-band for vertically balanced cuts (so V_{90} = 20 dB), with H_{90} = 10, 0, and -10 dB. The Q-band feed location is just 5 degrees from the horizontal axis, so we expect the subreflector rotation to be highly effective in removing the elevation-dependent asymmetry. This is indeed the case – the uncorrected maximum in vertical asymmetry of $\pm$20 dB is reduced to about 2dB. Due to the feed positioning, the effect of the horizontal offset is very small – the small slopes seen in the corrected horizontal cuts (middle column) reflect the horizontal motion introduced by the subreflector rotation.

The major takeaways for this band are:

- The subreflector rotaton is highly effective in removing the strong elevation SLR dependency. This is shown by the horizontal blue and red solid lines in the left panel, which are both within 1 dB of zero in every panel.
- Both optimization schemes induce a small elevation-dependence in the horizontal asymmetry – caused by the subreflector rotation and the slight offset of the feed from the horizontal axis. The span of this introduced asymmetry is about 4 dB, approximately balanced about the intrinsic value.
- The residuals in both axes are essentially the same for both optimization schemes.

The situation is rather different for bands whose feeds are significantly off the horizontal axis. The clearest example is Ku-band, shown in Fig. 5, as the feed is nearly 45 degrees of the horizontal axis. Here we show the same information, with a smaller value of the horizontal offset (7.5 dB), which matches the largest value we actually see. As in the preceding plot, the black lines show the uncorrected vertical (left column) SLR, S_V, horizontal (center column) SLR, S_H, and 'radial' (quadratic sum of the two orthogonal cuts) in the right column for three different horizontal offsets. The red lines show the resulting SLRs after optimal correction, the blue lines the SLRs after optimization in elevation alone, with the fiducial angle E_0 = 60 degrees. With optimal rotation (red traces), the net (radial) offsets are always improved, although the improvement is negligible over certain elevation ranges, depending on the value of the horizontal offset. With optimization based on the vertial alone (blue traces), balanced about E = 60, there can be actual degradation in the radial offset (blue lines above the black lines in the right-hand column), although in these cases, there is considerable improvement at other elevations. Note that for zero horizontal offset, there is no significant difference between the two proposed corrections systems (central row).

Conclusions are:

- The optimum rotation mechanism (red traces) always improves the SLR values, although the improvements in some scenarios where the horizontal offsets are significant are not large, and are limited to about half

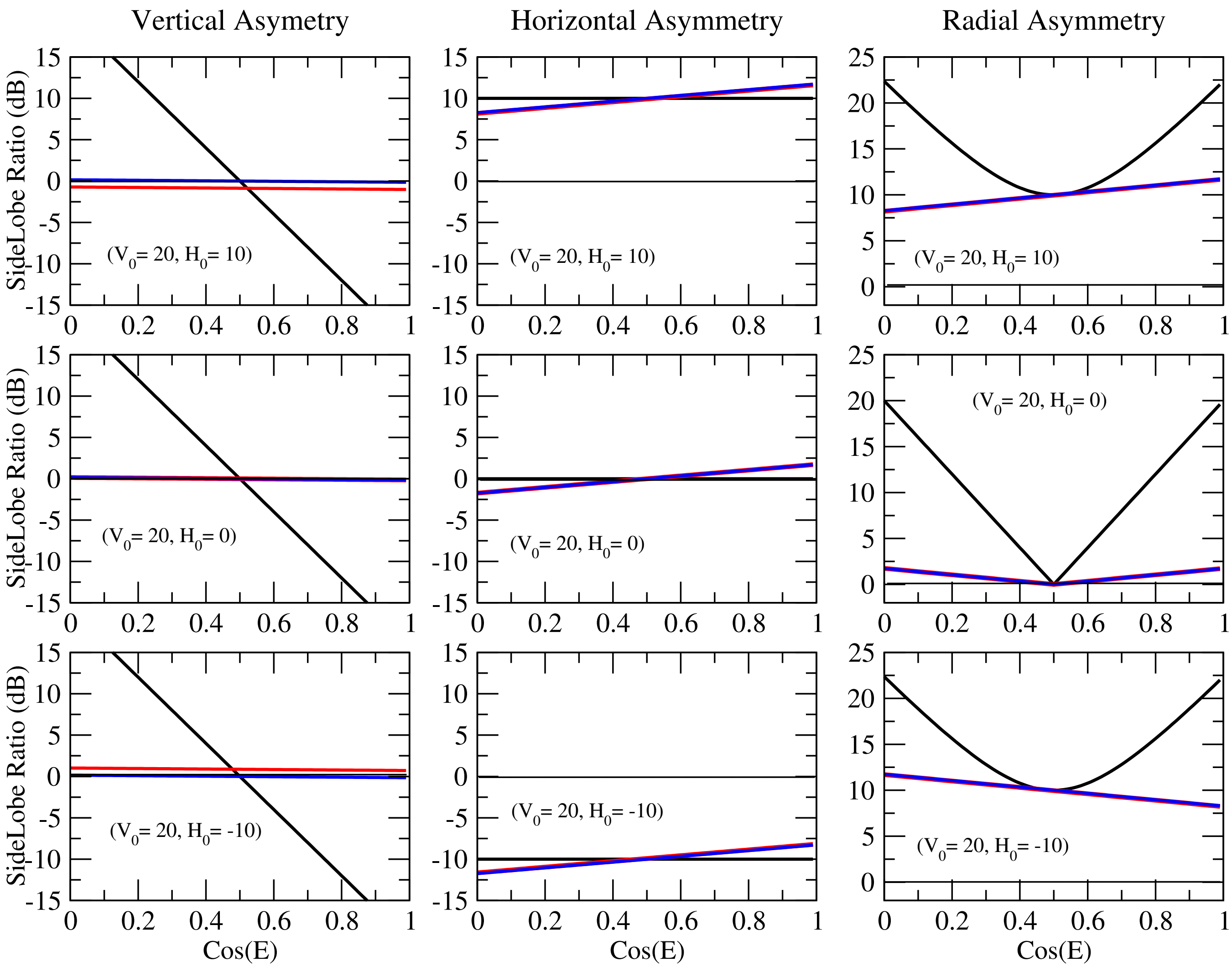

Figure 4: Showing the improvement in SLR at Q-band in the vertical axis (left column), horizontal axis (central column) and the 'radial' (quadratic sum of the orthogonal cuts) for three values of the horizontal offset. It is assumed that the vertical profiles are balanced about E = 60 degrees. The black traces show the uncorrected asymmetries, red the residual after optimal rotation including the horizontal offset, while blue shows the residual after optimization based on zero vertical asymmetry at E = 60. The values for V_{90} and H_{90}, in dB, are written in each panel. The overall improvement is dramatic, while the effect of the rotation on the horizontal offset is minor.

the elevation range. In this case, since the elevation-dependent rotation is on, the slope of the vertical SLR is reduced, but at the cost of introducing an elevation-dependent change in the horizontal offset which can be larger than the uncorrected horizontal offset.

- The E = 60 vertical optimization, with subsequent elevation-dependent rotation (blue traces), always gives the best correction in the elevation profiles (left column), but at the cost of a worsened horizontal profile over half the elevation range.

In all cases, the best optical alignments are with the horizontal offset removed.

4 Determining the Model Coefficients

Although the results of the three-rotation methodology are sufficient for rough determination of the rotation coefficient and offsets, a more accurate determination method was actually employed. This makes use of single beam cuts, combined with the measured rotation coefficient of 10.5 deg·GHz/dB to convert the observed SLR to

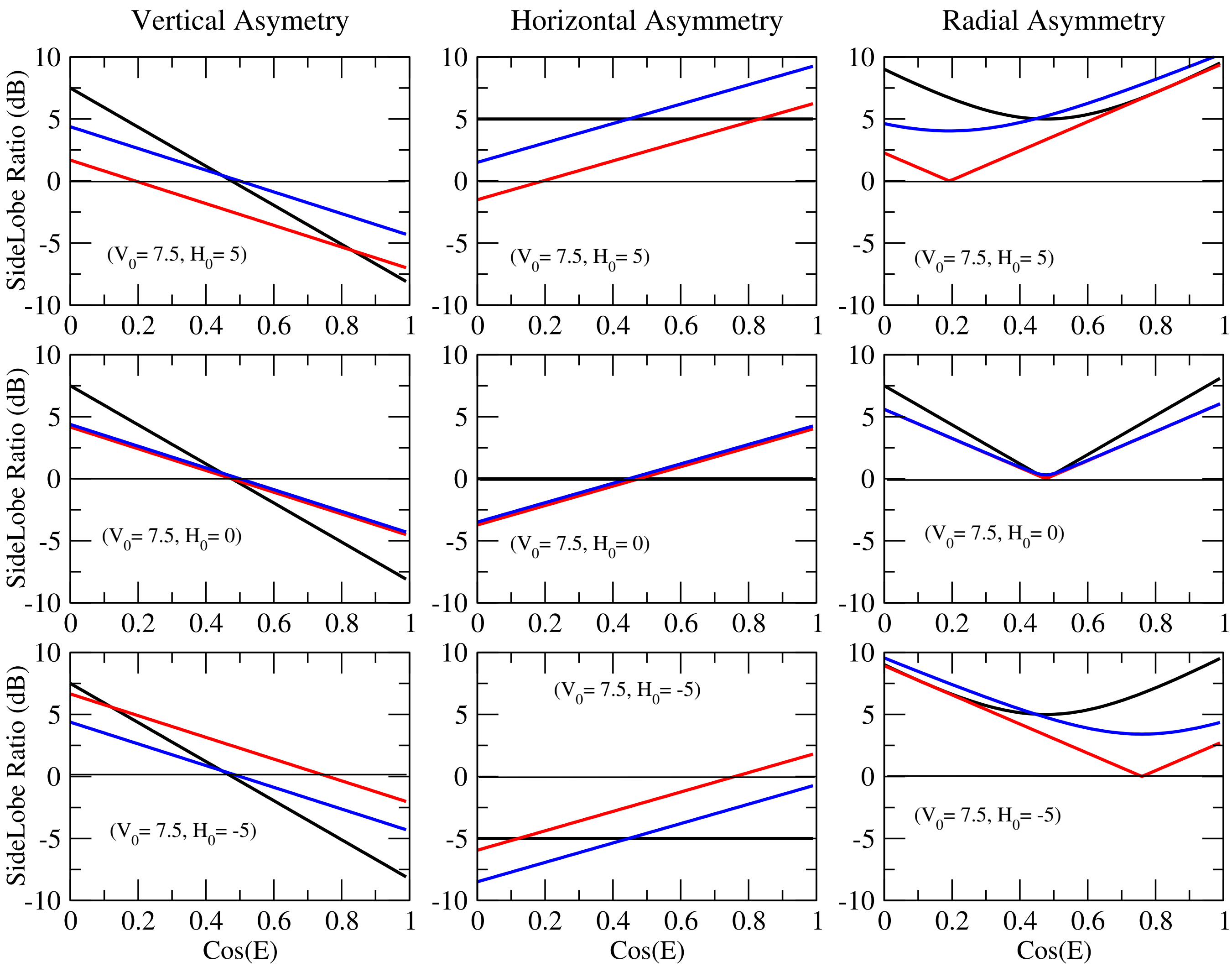

Figure 5: Showing the improvement in SLR at Ku-band for horizontal offsets of -7.5, 0, and 7.5 dB, for the two optimization scenarios. Black traces shows the uncorrected asymmetries, red the residual after optimal rotation including accounting for both offsets, and blue shows the residual after optimization based on zero vertical asymmetry at E = 60. The values of (V_0, H_0 utilized are written in each panel. While there is usually an improvement with the correction turned on, the improvement is usually small, and highly dependent on the value of the horizontal offset.

the subreflector rotation required to remove the observed imbalance. This allows use of both the three-rotation data and the single-cut data.

4.1 Observations

The additional beam cut observations are shown in Tables 4 and 5. The first table shows the observations taken before 18 July, 2019, the latter for data taken from that date through to the present. In these tables, the fifth column describes the observation type: 'Az' indicates a single cut in azimuth, 'El' a single cut in elevation, and 'Az+El' indicates both cuts were taken.

An important result is that the rotation coefficient used to offset the increasing beam asymmetry with decreasing elevation was incorrect. The old value, $\chi = 5.2$, used for the beam cut observations at Ku through Q bands, is about half of the correct value. The correct coefficient, $\chi = 11.0$ was implemented on July 18, 2019. Observations taken subsequent to this change are shown in Table 5.

All data were edited and calibrated using standard methods for delay, bandpass, and gain. The data from the cuts were extracted for analysis by the AIPS program UVHOL. Details of the use of this program are given in the holography memo.

Table 4: **Observing Log for Az+El Observations before 18 July 2019**

Rotation Coefficient $\chi_0 = 5.2°$ applied at Ku, K, Ka, and Q bands.

Date	Bands	RefAnt	El	Nature	Target	Conf	Comments
25-Jul-2017	C,X,U	1 9 23	64	Az+El	3C345	C	
28-Jul-2017	C,X,U,K,A,Q	6	52	Az+El	3C345	C	Subr. Rotation Off
28-Jul-2017	C,X,U,K,A,Q	6	30	Az+El	3C345	C	
01-Aug-2017	C,X,U,K,A,Q	many	28	Az	J0217	C	Prep for Nudge Tests
02-Aug-2017	C,X,U,K,A,Q	many	42	Az	3C84	C	ea20 sub 8mm left
02-Aug-2017	C,X,U,K,A,Q	many	57	El	J1220	C	ea20 sub 8mm down
04-Aug-2017	X, U	many	58	Az+El	3C84	C	check sub return
10-Aug-2017	C,X,U,K,A,Q	3 4 9	45	Az+El	3C345	C	
18-Aug-2017	A Q	3 4 9	47	Az+El	3C345	C	
		ACU Upgrade on ea07, ea16 and ea28					
31-May-2018	C X U K A Q	5 9 19	50	Az+El	3C273	A	
		ACU Upgrade on ea24 and ea27					
		ea05 subreflector moved 3.5 mm left					
01-Jul-2019	U K A Q	3 4 6 7	24 78	El	J0217, 3c345	BnA	
04-Jul-2019	K	11 13 16	var	El	var	BnA	
05-Jul-2019	K A	2 12 17	21 74	El	J0555 J1927	BnA	
17-Jul-2019	U K A Q	3 6 16	many	El	many	BnA	Seven elevations

Table 5: **Observing Log for Observations taken after 17 July, 2019**

Rotation Coefficient of $\chi = 11.0$ degrees applied at K, Ka, and Q bands.

Date	Bands	Refants	El	Nature	Target	Conf	Comments
18-Jul-2019	U K A Q	3 6 16	var	El	var	B→A	
18-Jul-2019	U K A Q	11 13 23	53	El	3C84	B→A	
23-Jul-2019	X U K	9 13 16	25	Az+El	3C84	B→A	Oversampled
25-Jul-2019	X U K A Q	9 13 16	var	El	3C84	B→A	
29-Jul-2019	X U K A Q	11 24	var	Az+El	3C84 3C273	B→A	Q Oversampled
30-Jul-2019	X U K A Q	11 24	48	Az+El	3C273	B→A	Q Oversampled
		ea09 and ea19 ACU Upgraded					
27-Jan-2020	X U K A Q	11 24 27	57	Az+El	3C273	D	
30-Jan-2020	X U K A Q	10 21 25 28	58	Az+El	3C273	D→C	
26-Feb-2020	X U K A Q	10 25 28	58	Az+El	3C273	C	
20-Mar-2020	U K A Q	21 25 28	25	Az+El	3C273	C	
29-Mar-2020	U K A Q	21 28	82	Az+El	3C345	C	
29-Mar-2020	U K A Q	21 25 28	58	Az+El	3C273	C	
23-Apr-2020	U K A Q	7 8 11	57	Az+El	3C273	C	Zero-Points Adjusted
17-May-2020	U K A Q	4 13 16	50	Az+El	3C454.3	C	Zero-Points Adjusted
11-Jul-2020	U K A Q	20 23 26	55	Az+El	3C345	B	
		ea03 ACU Upgraded					
22-Nov-2020	C X U K A Q	13 17 21	30	Az+El	3C84	B→A	
25-Nov-2020	C X U K A Q	13 17 21	80	Az+El	3C84	B→A	
30-Nov-2020	C X U	13 17 21	108	Az+El	3C84	B→A	
03-Dec-2020	K A Q	13 17 21	102	Az+El	3C84	B→A	
20-Feb-2021	U K A Q	7 8 11	58	Az+El	3C273	A	
25-Feb-2021	U K A Q	17 24 27	58	Az+El	3C273	A	
04-Mar-2021	C X U K A Q	1 14 20	56	Az+El	3C273	A→D	
09-Mar-2021	C X U K A Q	1 14 20	57	Az+El	3C273	A→D	
10-Mar-2021	U	3 16 17	30,58,83	Az+El	3C273,3C286,J0217	A→D	
15-Jun-2021	C X U K A Q	10 11 28	57	Az+El	3C273	C	

4.2 Determining the Model Parameters

To enable optimum correction of the asymmetry, we need to measure the three model parameters: the rotation coefficient, $\chi = K_\nu/L_\nu$, and the horizontal and beam sidelobes asymmetries at the zenith: (H_{90}, V_{90}). To do this, vertical and horizontal beam cuts were taken through the antenna beams over a wide elevation range. Each cut provides a value of the SideLobe Ratio (SLR). Plotting these against $\cos E$ provides a slope and intercept which are converted into the rotation values needed through the conversion of 10.5 deg·GHz/dB.

4.2.1 Parameter Analysis

The beam cut data used for the parameter analysis were taken with three different subrotation rotation applications – (i) No rotation: $\chi = 0$, (ii) The original rotation model, with $\chi = 5.2$, and no change in the rotation offset, and (iii) the updated model, with $\chi = 11.0$ and an updated rotation offset. Specifically:

- **No Rotation**: All C-band and X-band data, and the Ku-band data taken after July 17 2019, had no elevation-dependent subreflector rotation applied. The Ku-band data had an updated offset rotation applied.
- **Original Model**: All Ku, K, Ka, and Q band data taken before July 18, 2019 had an elevation-dependent rotation applied with coefficient $\chi_0 = 5.2$ degrees. No changes were made to the rotation offset.
- **New Model**: All K, Ka, and Q band data taken after July 17, 2019 had the new elevation rotation coefficient $\chi = 11.0$ degrees, and an updated rotation offset, to set the vertical SLR $S_v = 0$ at E = 60 degrees, applied.

The analysis of the beam cut data is somewhat complicated by the application of the rotation, which must be accounted for in the derivation of the model parameters. The analysis is straighforwards.

We start by repeating the basic relations between SLR, $\cos E$, and the subreflector rotation ϕ, (equations 9 and 10):

$$S_V(E,\phi) = V_{90} - K_\nu \cos E + L_\nu \phi \cos\theta_f \tag{29}$$
$$S_H(\phi) = H_{90} - L_\nu \phi \sin\theta_f \tag{30}$$

where V_{90} and H_{90} are the observed frequency-dependent vertical and horizontal asymmetries at the zenith, and K_ν and L_ν are the frequency-dependent slopes in the relation between the SLR and $\cos E$ and ϕ, respectively. The effect of applying a partial correction, with rotation coefficient $\chi_0 = 5.2$, and no change in the rotation offset, is to rotate the subreflector by an angle $\phi_o = \chi_0 \cos\theta_f \cos E$. With this correction applied, the observed asymmetries become

$$S_V(E,\phi) = V_{90} - (K_\nu - K_0 \cos^2\theta_f) \cos E \tag{31}$$
$$S_H(\phi) = H_{90} - (K_0 \sin 2\theta_f \cos E)/2 \tag{32}$$

where $K_0 = L_\nu \chi_0$ is the effective vertical sidelobe asymmetry reduction due to the application of the old coefficient.

The observed vertical and horizontal SLR data were plotted against $\cos E$, and a linear LSQ fit made. The measured slopes (m_v and m_h) and intercepts (b_v and b_h) are then related to the desired model coefficients by

$$K_\nu = K_o \cos^2\theta_f - m_v \tag{33}$$
$$V_{90} = b_v \tag{34}$$
$$H_{90} = b_h \tag{35}$$
$$\sin(2\theta_f) = -2m_h/K_0 \tag{36}$$

Note that the last of these relations provides no new information, as θ_f and K_0 are known quantitites. The observed slope in the horizontal beam cut asymmetry vs. $\cos E$ is due to the rotation. In essence, this relation provides a 'reality check' on the model – we expect the feed position angle derived from the horizontal slope to match that known from the antenna feed placement.

For feeds close to the horizontal axis, equation 33 reduces to $K_\nu = K_0 - m_v$ – the coefficient is simply the sum of the (negated) measured slope and the applied value.

An example of the data and fits for ea04 at X through Q bands is shown in Figure 6. Note that these data are the normalized SLR values ($S = S_\nu/\nu$), which allows plotting with the same vertical axes. The observed data are shown by the solid dots, the LSQ fits by solid lines. The black points show data taken before 18 July 2019 – using the original rotation coefficient of $\chi_0 = 5.2$ degrees with no change in the rotation offset at Ku through Q bands, and without any rotation correction at X band. Data taken after 17 July, using the new coefficient $\chi = 11.0$ degrees at K, Ka, and Q bands, and a new rotation offset at Ku, K, Ka, and Q bands, are in red. Some detailed comments follow:

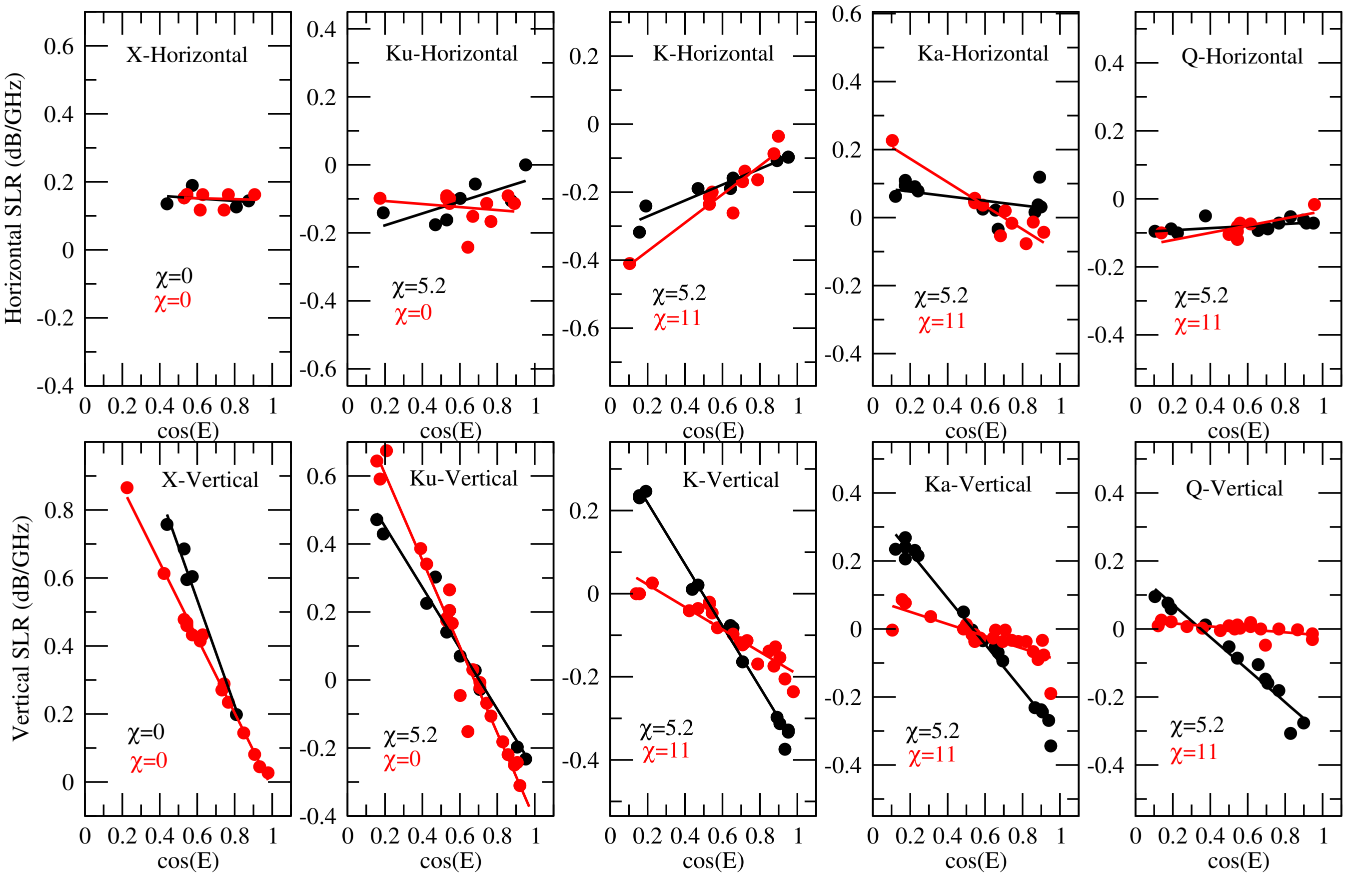

Figure 6: Showing typical sidelobe asymmetry fits to the beam cuts from ea04, arranged by band from X (leftmost panels) to Q (rightmost panels). All plots are on the same vertical scale. The horizontal cuts are in the upper row, the vertical cuts in the lower. The data are normalized by dividing the observed SLR values by the frequency in GHz. The solid lines show the LSQ fits. Black points and lines are from data taken prior to July 18, 2019, red points and lines show data taken after July 17, 2019. Data were taken with different subreflector rotation coefficients – those used are written in each panel. The new data shown in red at Ku through Q bands have a rotation offset applied which zeros the imbalance at $\cos E = 0.5$. The dramatic improvement in the elevation-dependent asymmetry at these three bands due to the new rotation coefficient and offset is apparent.

- All data at X-band, and the recent data at Ku-band were taken without any subreflector rotation. The horizontal cuts for these show no significant dependence on elevation, while the vertical dependence is large – the Ku-band vertical SLR data vary by more than 15 dB between the zenith and horizon. This span is much higher than that seen with the correction applied, as shown in the models in Figure 5. The different slopes at X-band between the old and new data – which should be same – are due to a single, low-elevation point in the older data, which is likely erroneous. The data remaining after excluding this point span too small a range in elevation to provide a robust estimate of the slope.
- The older data (shown in black) at Ku through Q bands show the effect of an insufficient rotation correction – a significant elevation dependence remains in the vertical, and a small, induced, dependence is seen in the horizontal.
- The new data (shown in red) at K, Ka, and Q band show the benefit of the full rotation correction. At Q-band, whose feed is only 6 degrees off the horizontal axis, near-perfect balance is seen in the vertical, while a small and constant imbalance is seen in the horizontal. At K and Ka bands, an increased imbalance in the vertical is seen – a result of the $\cos\theta_f$ dependence of the rotation correction, which is needed to reduce the induced change in asymmetry in the horizontal cuts. Application of the correct coefficient $\chi = 11$ gives a good balance – the range in residual asymmetries are about equal in each dimension. This is the best that can be done. At Ku-band, the absence of the rotation correction worsens the vertical asymmetry. Application of the correction will significantly reduce the spread, but at the cost of increasing the spread in the horizontal cuts.

- The rotation offset has placed the vertical asymmetry near zero at $\cos E = 0.5$ for Ku through Q bands. (No offset was attempted at X-band – and the vertical offset remains large). The horizontal offsets can only be addressed by physical displacement of the subreflector or feed. This work remains to be done.

4.2.2 Derived Coefficients – Slope Parameter

Asymmetry data for each antenna and band were analyzed using the method described above to derive the (band-independent) rotation coefficient $\chi = K_\nu / L_\nu$. The results are shown in Table 6.

Table 6: **Rotation Coefficient Determination**

Errors in individual entries are from the fits. Errors in the average values are from the dispersions.

Band	X	Ku		K		Ka		Q	
RotCoef	$\chi_0 = 0$	$\chi_0 = 5.2$	$\chi_0 = 0$	$\chi_0 = 5.2$	$\chi_0 = 11$	$\chi_0 = 5.2$	$\chi_0 = 11$	$\chi_0 = 11$	
Antenna	Derived Rotation Coefficients								Average
1	11.4±0.6	11.9±0.7	12.7±0.3	11.2±0.3	11.0±0.3	12.7±0.4	13.3±0.5	12.1±0.7	12.0±0.3
2	10.8±0.3	13.0±1.0	11.7±0.5	15.0±0.5	11.7±0.4	10.5±0.2	10.8±0.3	12.2±0.6	12.0±0.5
3	9.8±0.7	10.5±0.3	9.9±0.5	10.2±0.5	9.9±0.3	11.5±0.2	12.5±0.8	10.5±0.2	10.6±0.3
4	11.5±0.3	11.1±0.7	11.6±0.6	12.1±0.3	11.8±0.3	12.3±0.2	11.9±0.3	11.3±0.1	11.7±0.1
5	10.2±0.6	9.9±0.9	10.6±0.7	11.4±0.4	11.6±0.8	11.1±0.5	11.7±0.5	12.0±0.6	11.1±0.3
6	9.1±0.3	7.7±0.8	10.3±0.4	10.1±0.3	10.3±0.5	9.3±0.3	10.8±0.3	11.4±0.3	9.9±0.4
7		9.9±1.8	10.3±0.4	12.3±0.3	10.5±0.2	12.2±0.4	10.9±0.4	11.0±0.3	11.0±0.3
8	10.6±0.3	11.4±0.9	10.6±0.5	11.1±1.7	9.9±0.4	7.7±2.1	10.7±0.4	11.0±0.3	10.4±0.4
9	15.4±2.2	10.3±0.5	9.6±0.8	10.8±0.4	9.5±0.7	9.3±0.3	9.2±0.3	10.4±0.9	10.6±0.7
10	10.4±0.2	9.8±0.6	10.4±0.3	10.0±0.4	10.2±0.2	9.0±0.4	10.4±0.3	10.2±0.2	10.0±0.2
11	10.4±0.2	10.5±0.4	12.0±0.3	12.2±0.3	11.6±0.2	11.5±0.2	12.4±0.2	12.6±0.3	11.6±0.3
12	11.3±0.2	10.3±0.4	10.8±0.3	11.6±0.3	11.6±0.2	10.8±0.2	10.9±0.2	11.0±0.3	11.1±0.1
13	10.5±0.4	9.3±0.4	9.6±0.3	10.3±0.2	9.8±0.3	11.1±0.3	11.0±0.2	11.3±0.4	10.4±0.3
14	9.9±0.2	10.4±0.5	10.4±0.3	10.6±0.8	10.5±0.2	10.0±0.2	10.0±0.6	10.3±0.6	10.3±0.1
15	15.8±0.5	14.6±0.4	16.9±0.8	16.8±0.5	15.0±0.7	16.5±0.7	15.9±0.3	13.6±0.2	15.6±0.4
16	9.3±0.6	10.8±1.8	11.7±0.6	11.9±1.3	11.2±0.3	11.5±0.7	9.3±1.2	11.2±0.2	10.9±0.3
17	11.3±0.3	12.6±1.2	12.0±0.4	11.6±0.4	11.8±0.2	13.0±0.6	12.5±0.3	11.3±0.2	12.0±0.2
18	14.3±0.4	14.4±0.9	12.6±0.5	12.5±0.4	12.5±0.3	12.8±0.2	12.8±0.2	13.2±0.3	13.2±0.3
19		13.9±0.5	11.7±0.6	13.2±0.3	10.7±0.9	11.7±0.2			12.2±0.4
20	9.8±0.2	11.1±0.4	11.9±0.3	11.2±0.1	11.0±0.3	11.5±0.2	12.2±0.3	12.2±0.4	11.4±0.3
21	11.5±0.6	11.1±0.8	12.8±0.6	12.0±0.3	12.9±0.4	10.8±0.2	11.9±0.4	12.0±0.4	11.9±0.3
22	11.7±0.2	11.5±0.6	12.8±0.6	12.2±0.3	12.3±0.3	12.2±0.4	12.9±0.3	12.1±0.4	12.2±0.2
23	10.4±0.2	11.0±1.4	11.3±0.4	12.0±0.4	12.2±0.5	11.6±0.3	12.2±0.3	11.0±0.3	11.5±0.2
24	9.6±0.2	10.5±0.8	12.3±0.6	10.9±0.3	11.3±0.4	10.3±0.3	11.8±0.1	12.3±0.3	11.1±0.3
25	10.5±0.3	10.8±0.5	11.8±0.6	10.4±0.3	11.1±0.5	10.3±0.2	12.4±0.4	11.7±0.2	11.1±0.3
26	10.7±1.6	10.5±0.9	9.9±0.3	11.5±0.8	10.0±0.4	11.1±0.6	10.8±0.7	11.2±0.8	10.7±0.2
27	10.0±0.5	10.2±1.6	11.7±0.4	11.6±1.0	11.5±0.3	11.3±0.7	11.9±0.5	11.7±0.2	11.3±0.2
28	9.7±0.2	9.8±1.5	9.9±0.3	9.7±0.5	10.6±0.4	10.3±0.4	11.1±0.3	11.3±0.3	10.3±0.2
Avg	11.0±0.5	11.0±0.3	11.4±0.3	11.7±0.3	11.2±0.3	11.2±0.3	11.6±0.5	11.6±0.2	11.4±0.2

The derived rotation coefficients are very consistent between antennas and bands. The right-most column shows the average over all bands, the row at the bottom shows the average over all antennas for a single band. This latter quantity shows no significant variation with observing band, and suggests an optimum value of $\chi = 11.4$ degrees. There are statistically significant variations between antennas, as shown in the right-most column. However, for only two antennas – ea15 and ea18, are the derived values more than $\sim 3\sigma$ from the overall mean. Both of these antennas have long been known to have especially poor beam shape responses at low elevations. It is likely that the deviant values of the elevation coefficient are due to the change in beam shape– most low elevation profiles for these two antennas at high frequencies have no sidelobes to measure, as the astigmatism has washed out the first nulls. This astigmatism is likely due to elevation-dependent warping of the reflector shape – an issue that cannot be addressed by our simple models.

It will be noted that the table does not include the Q-band data taken with the old coefficient of $\chi_0 = 5.2$. This is because the derived values are significantly smaller than all other measures (the average coefficient is 9.6), as is evident in the flatter slope seen in the black data in the bottom right panel of Figure 6. This may also be due to the extremely warped vertical beam profiles seen at this band, when utilizing the old coefficient, at low elevations. Certainly the reason is related to the uncorrected asymmetry at high frequencies and low elevations, as application of a coefficient closer to the true value results in an especially accurate determination.

4.2.3 Derived Parameters – Offset Rotation Values

The horizontal and vertical zenith asymmetries provided by the fits are utilized in generating the desired rotation offsets. As discussed earlier, there are three possible values – one which optimizes the beam asymmetry accounting for both horizontal and vertical assymetry, one which optimizes the vertical asymmetry alone, using the condition of balancing the asymmetry at a fiducial elevation of 60 degrees after applying the elevation-dependent rotation, and one which balances the vertical profiles at E = 60, with no elevation-dependent rotation. The resulting values are given in Table 7. Note that the values for Ku through Q bands are derived from data taken after March 2019, and include the zero-point adjustments made prior to that date. The listed values are changes to those utilized in the observations. The adjustments shown in the table have been implemented.

Table 7: **Subreflector Offset Rotation Changes (deg)**

Ku, K, Ka and Q band data taken between March, 2019 and December 2020. ϕ_{opt}: Optimum rotation including horizontal offset. ϕ_o: Vertical profiles balanced at E = 60, with subreflector rotation. ϕ_f: Vertical profiles balanced at E=60, with no subreflector rotation.

Bnd	C			X			Ku			K		Ka		Q	
Ant	ϕ_{opt}	ϕ_o	ϕ_f	ϕ_{opt}	ϕ_o	ϕ_f	ϕ_{opt}	ϕ_o	ϕ_f	ϕ_{opt}	ϕ_o	ϕ_{opt}	ϕ_o	ϕ_{opt}	ϕ_o
1	4.2	0.9	5.4	-4.8	-2.1	3.1	3.5	0.6	2.5	-0.8	-0.3	2.6	1.5	1.0	1.2
2	0.3	-0.8	3.8	-3.3	-2.6	2.7	9.1	4.8	-0.5	-0.8	-0.3	1.2	0.9	0.9	0.9
3	-7.2	-8.8	-4.0	-9.1	-8.9	-4.5	0.4	3.1	0.2	-2.6	-1.1	0.6	0.2	0.1	0.3
4	-10.7	-12.6	-7.4	-11.7	-12.5	-6.3	2.1	5.5	-0.3	-2.0	-0.8	0.0	0.3	0.3	0.4
5	-8.6	-8.8	-3.9	-7.9	-8.4	-3.3	1.9	4.8	-0.3	-1.0	-0.4	0.1	0.3	0.7	0.8
6	-4.5	-3.7	1.3	-2.5	-2.7	1.7	5.6	4.3	-0.9	-0.7	-0.3	1.7	1.4	1.7	1.8
7	-5.3	-5.9	-1.2	-4.8	-4.7	-0.1	5.5	5.0	-0.4	-1.2	-0.9	0.7	0.6	0.4	0.5
8	-10.2	-9.1	-2.5	-6.2	-7.5	-1.6	7.8	6.9	-0.9	0.9	0.0	0.6	0.5	0.8	0.8
9	-3.9	-4.9	-0.1	-5.6	-4.7	1.1	5.4	5.4	-0.8	0.3	-0.6	-0.4	-0.4	-0.1	-0.2
10	-8.1	-10.0	-5.0	-8.1	-8.1	-3.2	2.2	5.4	-0.7	-2.8	-1.0	-0.1	-0.3	-0.3	-0.1
11	-5.3	-5.4	-0.2	-4.5	-4.7	0.5	7.4	6.7	-0.7	-0.1	-0.6	0.4	0.1	0.1	0.1
12	-9.5	-11.3	-5.5	-11.5	-12.0	-6.3	3.7	5.1	-0.6	-1.1	-0.6	0.5	0.7	0.1	0.2
13	-7.5	-8.8	-1.9	-5.6	-5.4	0.1	5.2	4.8	-0.5	-1.0	-0.6	0.5	0.5	-0.2	0.0
14	-6.9	-8.0	-3.2	-5.5	-5.6	-0.9	2.5	4.2	-0.6	-2.1	-0.8	0.5	0.2	-0.3	-0.2
15	-5.1	-4.3	1.6	-3.5	-4.3	2.9	11.2	7.6	-1.0	3.0	1.9	2.3	2.6	1.8	1.7
16	-9.4	-11.2	-5.8	-9.2	-9.7	-4.4	4.8	5.5	-0.6	-0.1	0.1	0.3	0.7	0.6	0.6
17	-11.1	-11.9	-4.0	-8.1	-8.4	-2.6	3.3	5.6	-0.8	-1.0	-0.3	-0.7	-0.4	-0.1	0.0
18	-1.7	-0.9	4.9	0.0	0.1	6.8	11.3	5.1	-0.4	1.6	0.2	1.2	0.7	0.6	0.5
19	-8.8	-8.1	-2.0	-6.1	-6.9	-1.1	7.0	5.9	-0.6	2.1	1.0	0.7	1.4	1.1	0.9
20	-7.6	-8.4	-2.9	-7.4	-7.8	-2.4	4.0	4.6	-0.2	-0.3	0.2	1.0	1.2	0.8	0.9
21	-4.7	-6.8	-1.1	-8.0	-7.9	-1.9	7.2	6.7	-1.4	-0.1	-0.6	0.9	1.4	0.6	0.6
22	-7.1	-8.7	-4.7	-8.3	-8.5	-2.4	4.5	6.4	-1.1	-0.8	-0.2	0.9	0.7	0.0	0.1
23	-5.8	-5.8	-0.6	-5.3	-5.9	-0.8	6.7	3.6	-0.4	0.7	-0.6	-0.7	0.0	0.8	0.5
24	-5.4	-6.2	-1.1	-5.4	-5.6	-0.7	7.9	5.7	-0.6	-0.7	-1.4	-0.9	-0.7	0.4	0.3
25	-11.1	-11.8	-6.3	-8.4	-9.2	-3.8	1.2	3.5	-0.4	-0.8	-0.1	0.5	0.4	0.9	0.9
26	-4.4	-4.4	0.7	-4.5	-4.8	-0.2	7.7	5.6	-1.0	0.8	0.3	0.3	0.6	0.7	0.7
27	-6.0	-7.1	-2.5	-4.9	-4.8	0.1	2.6	4.5	-0.4	-2.2	-0.3	0.9	0.4	-0.2	0.0
28	-3.1	-5.8	-0.9	-7.6	-6.6	-1.6	6.0	2.7	0.1	-0.2	-0.2	0.8	0.7	-0.3	-0.2

The table includes all three rotation offsets for C, X, and Ku bands. It has now been decided to re-implementelevation-dependent rotation at Ku-band, while at C and X bands, no such rotation has been implemented. For the three highest frequency bands, only the two offsets which include elevation-dependent rotation are included, as there is no question that this will be employed.

Some comments on the values in the table are warranted:

- The offset values for C and X bands are large as there has been no initial offsets applied. The values are almost all negative (indicating a CW rotation is required to balance the sidelobes), suggesting a global error in the zero-point setting of the subreflector. All offsets are of a similar magnitude.
- The offset values for Ku-band reflect the zero-point rotations that were implemented in the Spring of 2020. At that time, it was decided to not implement the elevation-dependent rotation. The results of this are reflected in the table – the values of ϕ_f are near zero, while those relevant to applying the rotation are all positive, and about half of the full zenith-to-horizon rotation.
- The offset values for the high frequencies (K, Ka and Q bands) are all very small, as the zero-point values have been applied prior to the observations from which these values were derived.

As noted above, the zero-point adjustments have been implemented at all bands, and elevation-dependent rotation is applied at Ku-band and above.

4.3 Zero-Point Rotation Adjustments from Single Cuts

Once initial adjustments have been made, it is prudent to repeat observations with the new cofficients to ensure that the applied values are correct. Further, once antenna come out of maintenance, it is important to check for changes in subreflector alignment. It is clearly wasteful to take beam cuts over a wide range of elevations since the rotation coefficient, χ, is well known. With the known elevation correction, it is straightforwards to determine any incremental offset from a single cut at a given elevation, E.

The analysis depends on whether the subreflector rotation is implemented or not. Note that in the following equations, the system constant $\nu_G L \cos\theta_f = -2.0, -1.2, 1.1, 0.5, 0.3$, and 0.25 at C, X, Ku, K, Ka, and Q bands, respectively.

The changes calculated by the following expresions are to be added to those existing in the 'parmenator'.

4.3.1 No Rotation – C, X Bands

At a given elevation, E, the vertical SLR is given by

$$S_{V,E} = V_{90} - K_\nu \cos E \tag{37}$$

We desire this to be zero at a fiducial elevation E_0, so

$$0 = V_{90} - K_\nu \cos E_0 + L_\nu \Delta\phi \cos\theta_f \tag{38}$$

where $\Delta\phi$ is the additional subreflector rotation required to achieve the balance. Subtracting these two, we find for the incremental rotation

$$\Delta\phi = \left[\frac{-S_{V,E}}{L_\nu} + \chi(\cos E_0 - \cos E)\right]\sec\theta_f \tag{39}$$

4.3.2 Rotation Applied – Ku, K, Ka and Q Bands

With rotation turned on, the observed vertical SLR at a given elevation, E is

$$S'_{V,E} = V'_{90} - K_\nu \sin^2\theta_f \cos E \tag{40}$$

We want the rotation offset, $\Delta\phi$ which makes the profile equal zero at the fiducial elevation:

$$0 = V'_{90} - K_\nu \sin^2\theta_f \cos E_0 + L_\nu \Delta\phi \cos\theta_f \tag{41}$$

From the difference, we find, for $\Delta\phi$:

$$\Delta\phi = \left[\frac{-S'_{V,E}}{L_\nu} + \chi \sin^2\theta_f(\cos E_0 - \cos E)\right]\sec\theta_f \tag{42}$$

With these expressions, (equations 39 and 42) any single vertical cut at a known elevation will give the required subreflector rotation offset needed to balance the profiles at the fiducial elevation (normally, 60 degrees). If the cuts are arranged to be taken at or near the fiducial elevation (E = 60 degrees), the corrections are especially simple – and are given by the first term in these expressions.

4.3.3 Rotation Off to Rotation On

A third possibility exists – the beam cuts were taken with the rotation off, but we wish to apply the results to those needed when the rotation is on. The simplest approach is to use the vertical cut at elevation E to derive the corresponding value for V_{90}: $V_{90} = S_{V,E} - K_\nu \cos E$, and use this value in equation 19 (for balance at the fiducial elevation), or equation 11 (for optimal balance). In the former case, we get

$$\Delta\phi = \left[\frac{-S_{V,E}}{L_\nu} + \chi(\sin^2\theta_f \cos E_0 - \cos E)\right] \sec\theta_f \tag{43}$$

and, for the case of optimal sidelobe imbalance,

$$\Delta\phi = \frac{H_{90}}{L_\nu} - \left(\frac{S_{V,E}}{L_\nu} + \chi \cos E\right) \cos\theta_f \tag{44}$$

4.4 Examples of Improvements

Implementation of the new rotation coefficient alone is highly successful in reducing the beam asymmetry and loss in gain at high frequencies at low elevations. In Fig 7 we show vertical profiles cuts through ea09 at K-band at various elevations. The left panel shows two elevation cuts with no subreflector rotation. The strong elevation dependence on the profile is obvious. The middle panel shows four cuts with the old coefficient of $\chi_0 = 5.2$ degrees applied. The vertical dependence is much reduced, but not eliminated, indicating the applied coefficient was too low. Four cuts with the new coefficient of 11.0 (but with no accounting for the horizontal offset) is shown in the right-hand panel. The elevation dependence is virtually eliminated.

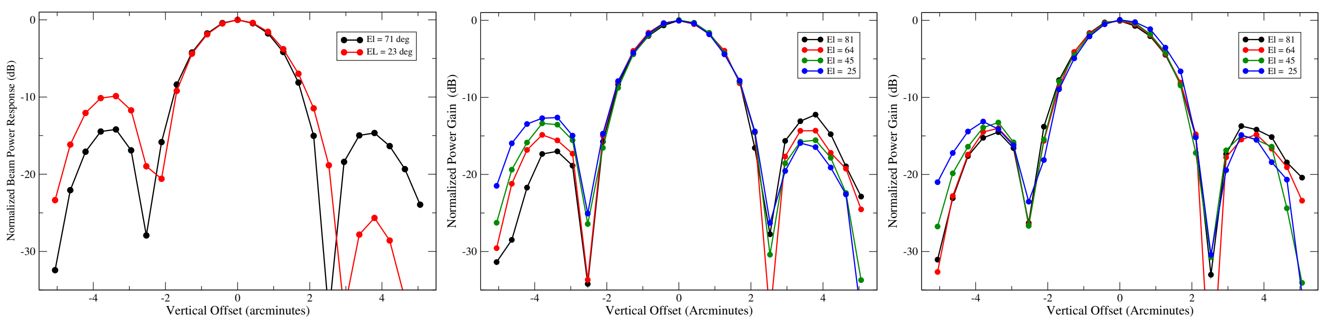

Figure 7: K-band vertical beam profiles of ea09. (Left) With no subreflector rotation correction. (Center) With the old coefficient of 5.2. (Right) With the new coefficient of 11.0. The new coefficient gives well balanced responses over a wide range of elevation.

The improvement is more dramatic at Q-band. In Fig 8 are shown vertical cuts through antenna ea04 with the old cofficient (left) and the new coefficient (right). A dramatic improvement is seen in the beam symmetry.

Signs are always a problem, so in order to check our conventions, a simple rotation offset to ea19 at Q-band was done. The results are shown in Fig 9, where we show vertical cuts through the beam of ea19 at Q band, before and after a +1.6 degree rotation of the subreflector. Both observations were taken at nearly the same elevation.

5 Final Adjustments – 2020/2021

As described earlier, the decision was made in July 2019 to implement the correct elevation coefficien ($\chi = 11$), and a subreflector rotation offset which did not utilize the horizontal offset H_0, while the rotation at Ku-band was turned off. (Ku-band rotation was restored in March 2021). Optimization was based on balancing the vertical beam profile alone at E = 60 degrees. Due to the generally poor quality of the summertime data, it was accepted that subsequent adjustments would be required to optimize the response. In adddition, the question of how to manage the horizontal offsets was left open – these can only be fully addressed by movement of the subreflector or feed.

In this section, we describe the observations made in 2020 and 2021, and the subsequent adjustments made on the basis of the results.

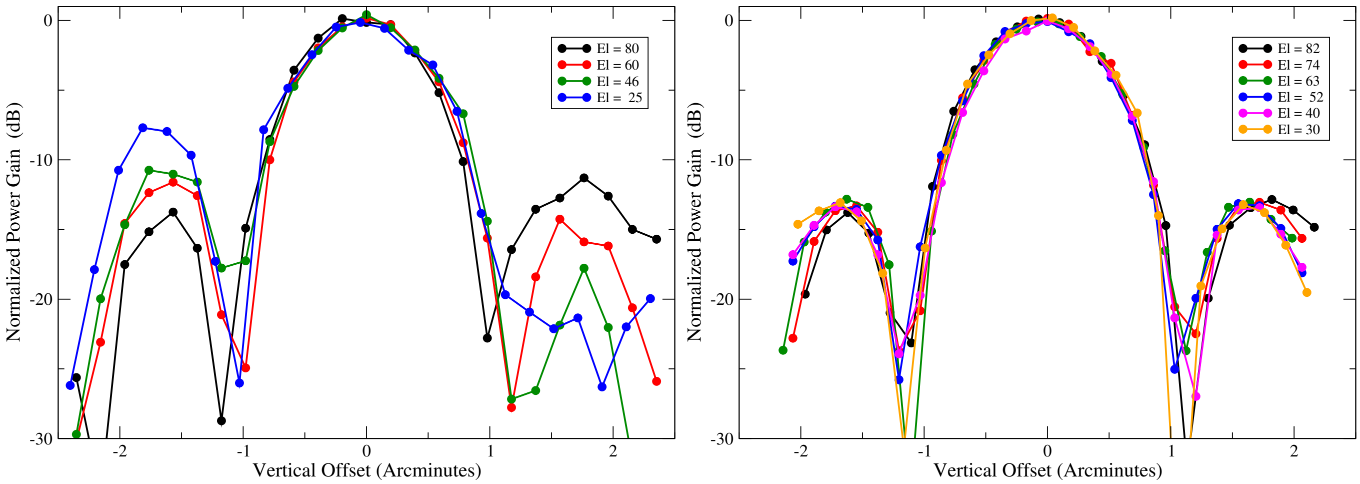

Figure 8: Q-band vertical profiles of ea04 with the old and new elevation coeffients. (Left) With the old coefficient of 5.2. (Right) With the new coefficient of 11.0. The new coefficient gives well balanced responses over a wide range of elevation.

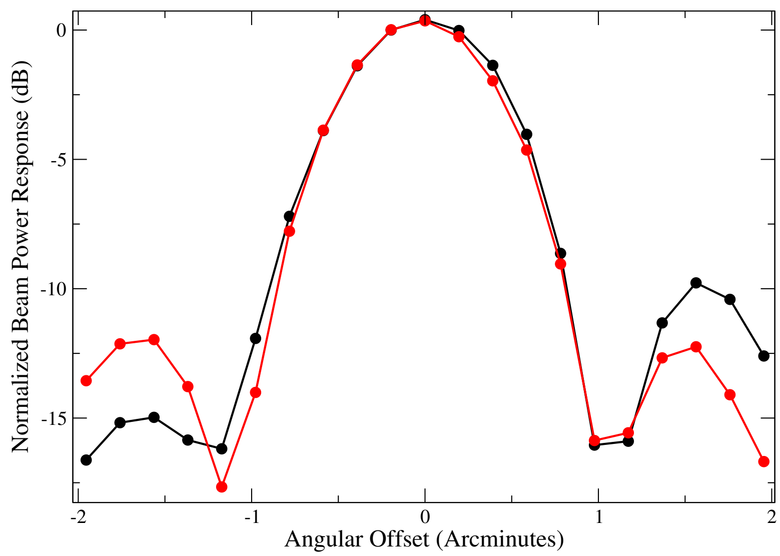

Figure 9: Showing the effect of rotating the zero-point of subreflector on ea19 at Q-band. The black curve is with the existing default, the red curve after a positive (CCW) rotation of 1.6 degrees. Both observations were taken at an elevation of about 55 degrees.

5.1 Observations

The 2020/2021 observation log is shown in the lower portion of Table 5. All observations comprised a single pair of orthogonal cuts, using only the strongest calibrator sources (3C 84, 3C273, 3C345, and 3C454.3), in excellent weather while in compact configurations (except for the most recent data taken after October 2020). The quality of the data is very good.

Between February and April 2020, offsets in the zero-point in the subreflector rotation parameter were made to balance the observered SLR at an elevation of 60 degrees for Ku, K, Ka and Q bands. The observations made after April provide a final check on the stability of the adjustments.

After a summer hiatus (during which all of the data taken in the program were reanalyzed, the the bulk of this memo was written), observations were taken during the 2020/2021 winter to further improve the subreflector offset positions, and to test possible implementation of the rotation at Ku, X, and C bands. While rotation at X and C bands has not been implemented, it was decided to restore rotation at Ku band, starting in March 2021.

5.2 Horizontal Offsets – What to do?

The beam cut data taken after March 2020 also provide estimates of the horizontal offsets needed to balance the beam. Because of the application of the rotation mechanism, the measured offset is in general a function of elevation. In order to best balance the beam profiles, any horizontal adjustments should be made after first balancing the horizontal profile at the fiducial elevation – currently 60 degrees. The horizontal imbalance at that elevation can only be removed by horizontal motion of the subreflector or feed.

To calculate the needed subreflector offset, we need the conversion between subreflector translation and beam asymmetry. To determine this, observations were made with the subreflector moved laterally by known amounts. These are described in Section 9.2, and the results are shown in the right-hand panel of Figure 24. The resulting relation is

$$\Delta x = \frac{-21}{\nu_G} S_{H,60} \quad \text{mm} \tag{45}$$

This empirical relation matches that predicted by the Ruze model, as explained in Section 7.

The suggested offset values, in millimeters, are shown in Table 8, utilizing data taken in June, 2021. These offset values are very stable, with changes of less than 1 millimeter between earlier observations taken in March 2021, and these.

Table 8: **Suggested Subreflector Horizontal Offsets in mm, rounded to 0.5 mm** A positive value indicates move the subreflector to the right, as seen looking outwards. Data taken in June 2021.

Antenna	C	X	Ku	K	Ka	Q	Avg Ka+Q	Avg K+Ka+Q
1	21	19	-7	-3	6	3	4.5	2.0
2	13	3	-12	-4	2	-1	0.5	-1.0
3	2	5	6	4	5	4	4.5	4.5
4	-2	1	6	4	-2	2	0.0	1.0
5	-3	-1	5	1	-2	0	-1.0	0.0
6	-2	-4	-5	0	2	2	2.0	1.0
7	2	0	-4	0	1	1	1.0	0.5
8	-8	-9	-7	-4	1	0	0.5	-1.0
9	7	6	-2	-3	-1	-3	-2.0	-2.5
10	5	3	3	6	2	4	3.0	4.0
11	1	-2	-7	-2	2	1	1.5	0.5
12	1	4	0	2	0	3	1.5	2.0
13	2	0	-3	0	1	3	2.0	1.0
14	2	-1	2	5	2	4	3.0	4.0
15	-2	-10	-18	-10	-1	-4	-2.5	-5.0
16	1	-1	-2	0	-2	1	-0.5	0.0
17	-1	-2	1	2	-2	1	-0.5	0.0
18	2	-6	-21	-9	2	-2	0.0	-3.0
19	-5	-6	-12	-8	-5	-6	-5.5	-6.0
20	-1	-2	-2	-1	-1	0	-0.5	-1.0
21	5	2	-7	-2	-3	0	-1.5	-1.0
22	1	-1	11	9	5	8	6.5	7.0
23	-2	-5	-7	-4	-4	-6	-5.0	-5.0
24	3	-1	-10	-4	0	-2	-1.0	-2.0
25	-6	-2	7	6	1	2	1.5	3.0
26	-1	-3	-9	-3	-2	-2	-2.0	-2.0
27	3	0	3	5	3	4	3.5	4.0
28	13	9	-7	-1	2	1	1.5	1.0

A positive offset means the subreflector must be moved to the right (as seen from behind) to correct the alignment. The formal $(1-\sigma)$ errors in the offset determinations are typically 0.5 mm, and as noted above, the repeatability, over timescales of at least a year, is better than 1 mm.

The table shows considerable scatter between the bands for most antennas. This indicates that the misalignments causing the horizontal asymmetries are not solely due to misplacement of the subreflector. However, there is also commonality in the offsets, particularly for the three highest-frequency bands. As these are the most affected by misalignments, a displacement based on the average over the upper frequency bands is appropriate. In the rightmost pair of columns are the suggested offsets, in millimeters. Keep in mind that any subreflector offsets will be reflected at all bands.

A test offset of +3.5 mm to the subreflector of antenna ea05 in June 2019 demonstrated that this interpretation, and our signs, are correct. The values in the table are the residuals, after the move. Antenna ea01 is a very special case. Notable for this antennas is that the offsets are large (except at K-band), and very different between the low frequency and high frequency bands. It is not possible to correct these offsets through moving the subreflector – the problem must lie in the horizontal positioning of the feeds.

Antenna 1 is not the only one with significant discrepancies in horizontal offset between receiver bands. Other antennas show notable differences as well. These can only be addressed by horizontal movement of the feed horn itself. The suggested motions are large – due to the magnification, there is a ten times multiplication of feed horn translation to match that of the subreflector. Hence, the suggested offset motions in the table are in cm, when considering feed motions. Note that no measurements of the effect of feed translation on sidelobe asymmetry have yet been made to confirm this interpretation.

A ranked list of suggested horizontal offsets has been prepared and sent to VLA operations.

5.2.1 Offset Correction Criteria

In this section, we discuss the criteria to decide whether a subreflector horizontal adjustment is warranted. The gain loss and beam distortion values are based on the simulation results shown in Section 8.

We can imagine two different criteria to decide the minimum correction threshold. The first is based on loss of forward gain. If we take a 5% loss in gain as the criterion, then Figure 23 tells us that the correction need only be applied to antennas whose offset is greater than 0.75λ. This corresponds to $\sim$3.5mm at the highest frequency of 50 GHz. Based on this criterion, only six antennas (ea01, 03, 19, 22, 23, and 28) need adjustment.

A much tighter criterion is based on beam symmetry. Good imaging with a synthesis array requires data taken over an extended period, over which it is important that the beam parameters remain constant, and circular. Lateral offsets in the subreflector position introduce ellipticity in the beam, particularly at the lower levels. Setting, for example, a criterion of keeping the first sidelobe ratio to less than 3dB imposes (from Figure 18) a maximum offset of 0.25λ, corresponded to 1.5mm at the maximum frequency. By this criterion, 18 antennas (based on the average of Ka and Q bands) need horizontal offset adjustments.

However, it is likely that this is too stringent a criterion, as the asymmetries seen in Figure 7 occur at very low levels – below -20 dB. This is confirmed by reference to Figure 25, showing that the broadening of the beam is barely perceptible at the -6 and -10 dB levels, out to 0.5λ. It is doubtful that beam symmetry at such a low level will ever be needed, as full-beam imaging at high frequencies will likely be limited by variations in pointing and tracking. A good compromise might be to correct the offsets when they exceed 0.5λ, or 3mm at the highest frequency. By this criterion, eight antennas should be adjusted.

5.3 Rotation On or Off at Ku-band?

As has been noted earlier, the subreflector rotation regimen is only really effective in removing the elevation beam distortion for feeds located hear the horizontal axis of the Cassegrain feed circle. Three of the four high frequency feeds are located within 20 degrees of this axis, and the results clearly show the benefit of the rotation. For Ku-band, however, the efficacy of the correction is far from clear. The feed location of 132 degrees means that the feed motion introduced by the rotation has nearly equal components in the vertical as horizontal, so that any reduction in the vertical distortion must be accompanied by a roughly equal growth of distortion in the horizontal. On the basis of this argument, we elected to turn off the rotation correction in July, 2019.

However, in terms of the radial distortion defined in section 3.2.2, there is a benefit in implementing the rotation. The plots shown in Figure 5 indicate a small advantage in retaining the rotation. Essentially, the partial reduction of the moderately large vertical distortion slightly outweighs the small increase in distortion in the horizontal induced by the rotation.

Consequently, the rotation correction was restored on March 09, 2021. An example of the beam cuts with, and without, the rotation is shown in Figure 10. As expected, the elevation-dependent vertical asymmetry is reduced, while a moderate horizontal asymmetry is introduced.

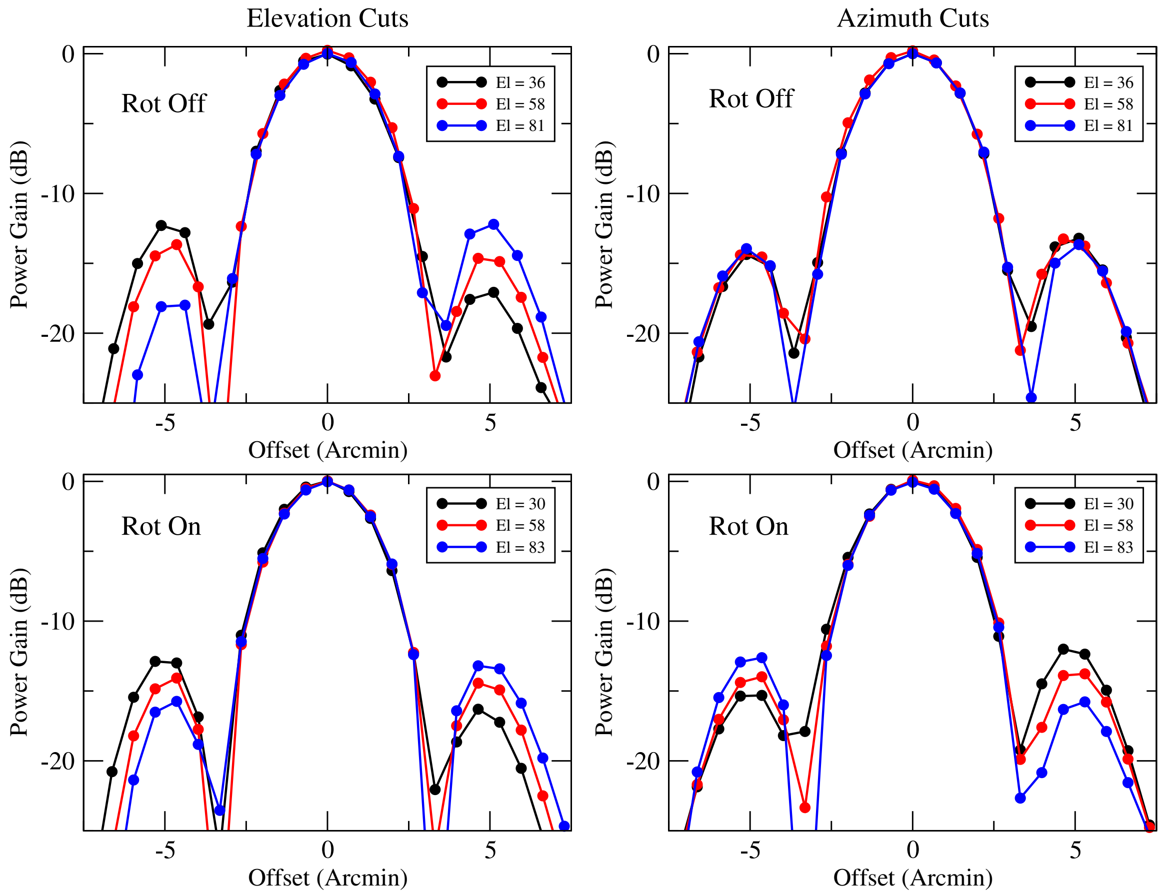

Figure 10: Showing the small improvement that subreflector rotation provides at Ku-band. Shown are the orthogonal cuts for ea20, with the rotation off in the upper row, and rotation on in the lower row. With rotation off, there is a significant asymmetry elevation dependency in the vertical (upper left panel), and no elevation dependency in the horizontal (upper right). With rotation on, a modest, and equal elevation dependency is seen in both dimensions (lower panels). In terms of the radial distortion function $S = \sqrt{S_V^2 + S_H^2}$, there is a small advantage in having the rotation applied.

6 Examples of Corrected Beam Cuts – A Discussion

As the adage says – 'The proof of the pudding is in the eating'. In this section, we show the successes – and some failures – of the improved performance provided by the updated adjustments.

In Figure 11 we show some examples of post-corrected beam cuts. These were taken in late 2020, with the correct rotation coefficient and rotation offset to ensure the vertical beams were balanced at E = 60. The figure shows orthogonal cuts at three elevations (∼30 degrees in black, ∼60 degrees in red, ∼ 80 degrees in blue), for ea11 at K band, ea12 at Ka band, and ea05 at Q band. These antennas were selected as they show clean profiles at all three elevations, and have a very small residual horizontal offset. Without the subreflector rotation, the span in vertical SLR would be ∼ 20, 30 and 40 dB at K, Ka, and Q bands, respectively. With the rotation, this has been nearly perfectly removed. The improvement in gain is about 10% for an SLR of 15 dB, and 30% for an SLR of 30 dB.

Currently, subreflector rotation is not applied at X and C bands. Typical profiles are shown in Fig. 12. Again, the chosen antenna (ea20) was selected for having good balance in both cuts at $E = 60$. This figure shows the expected elevation-independent horizontal cuts, while a small, but clear elevation dependence of the vertical cuts is visible. For C and X bands, the expected gain loss due to the imbalance is trivial – less than 1%. For Ku-band the loss can reach 5% for antennas with large offsets in the horizontal or vertical offsets, but is more typically 1 – 3%.

The preceding plots show antennas which behave well. Most antennas are similar to these. But some are rather different. Ea15 and 18 are notable in that they have a significantly larger elevation rotaton coefficient than the others. They also have curiously different – and large – horizontal offsets between the bands.

We show in Fig 13 the orthogonal cuts at Ku through Q bands for ea15. ea18 is very similar at most bands.

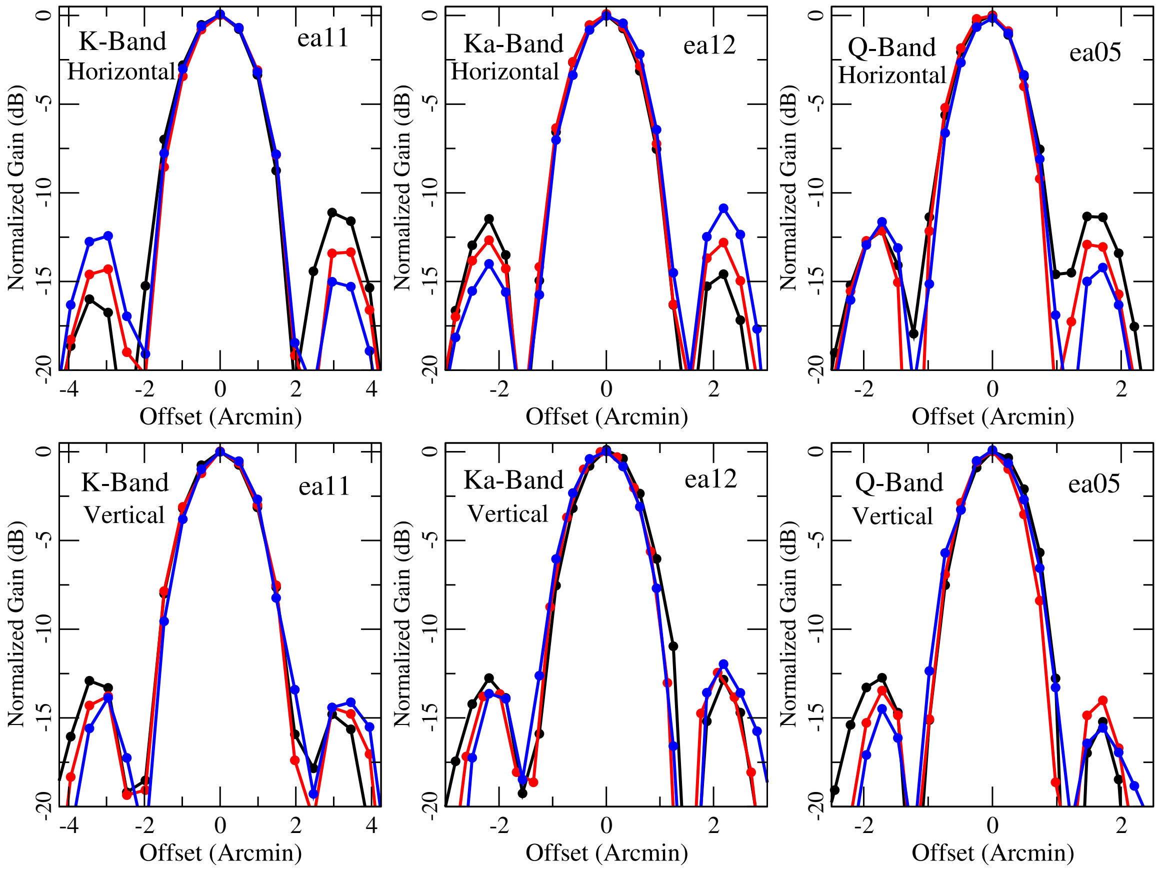

Figure 11: Orthogonal cuts with subreflector rotation applied at K, Ka, and Q bands. The antennas shown were selected for minimal imbalance at $E = 60$. The black trace was taken with $E \sim 30$ degrees, the red trace near $E \sim 60$ degrees, and the blue trace near $E \sim 80$ degrees. The variation in vertical SLR with elevation is almost completely removed, at the cost of a small dependence of horizontal SLR on elevation.

The horizontal profile at Ku-band (top left) is notable for the very high SLR – this can only be due to a horizontal displacement of the subreflector or feed. If the former, it correspondes to a 17 millimeter shift to the left. The same sense of asymmetry is seen at K and Q bands – however, due to the higher frequencies, the suggested shifts are much less – 8 and 3 millimeters, respectively. Note however, that Ka-band has a nearly perfect balance in the horizontal profiles – no shift at all is needed. Any attempt to adjust the Ku-band horizontal profile will inevitably greatly degrade the Ka-band profile. It is thus clear that the origin of the varying profiles is not the subreflector position. However, if we are to identify the feed itself as the origin of the variance – an offset of nearly *17 centimeters* is needed to correct the imbalance. This seems implausibly (even impossibly) large – yet we have no other suggestion for the variance between bands in these profiles.

The vertical cuts (lower row) also show unusual features. The Ku-band profile (taken without subreflector rotation) has a much larger elevation dependency than other antennas. The rotation coefficient for this antenna is 15.6 degrees – fully 4.2 degrees larger than the median, and larger than any other antenna, by far. This high coefficient is seen at all bands – it is truly a characteristic of this antenna. The large coefficient is responsible for the large residual dependency on elevation seen at K, Ka, and Q bands, where the subreflector rotation has been turned on, using the median coefficient of $\chi = 11$ degrees. At Q-band (lower right) we find another common phenomenon – apparent astigmatism. The smoothed profiles, with much diminished, or absent inner nulls, is seen in most antennas at this band, especially at elevations below 40 degrees. The probable cause is a large-scale distortion, in the vertical direction, of the main reflector. However, if this is the case, we would expect to see similar, but less, filling of the inner null at Ka-band, whose observing frequency is about 75% of that for Q-band. But – no such degradation is seen.

We have used the term 'astigmatism' to describe profiles whose first nulls are greatly minimized, or entirely absent. These are only seen in the vertical cuts, but do not have a simple relation to band, other than Q-band being the most affected. Because the horizontal cuts do not show this, the cause cannot be a focus error (which would 'fill in' the nulls equally for both cuts). Indeed, some antennas (ea06 is a notable example), strong

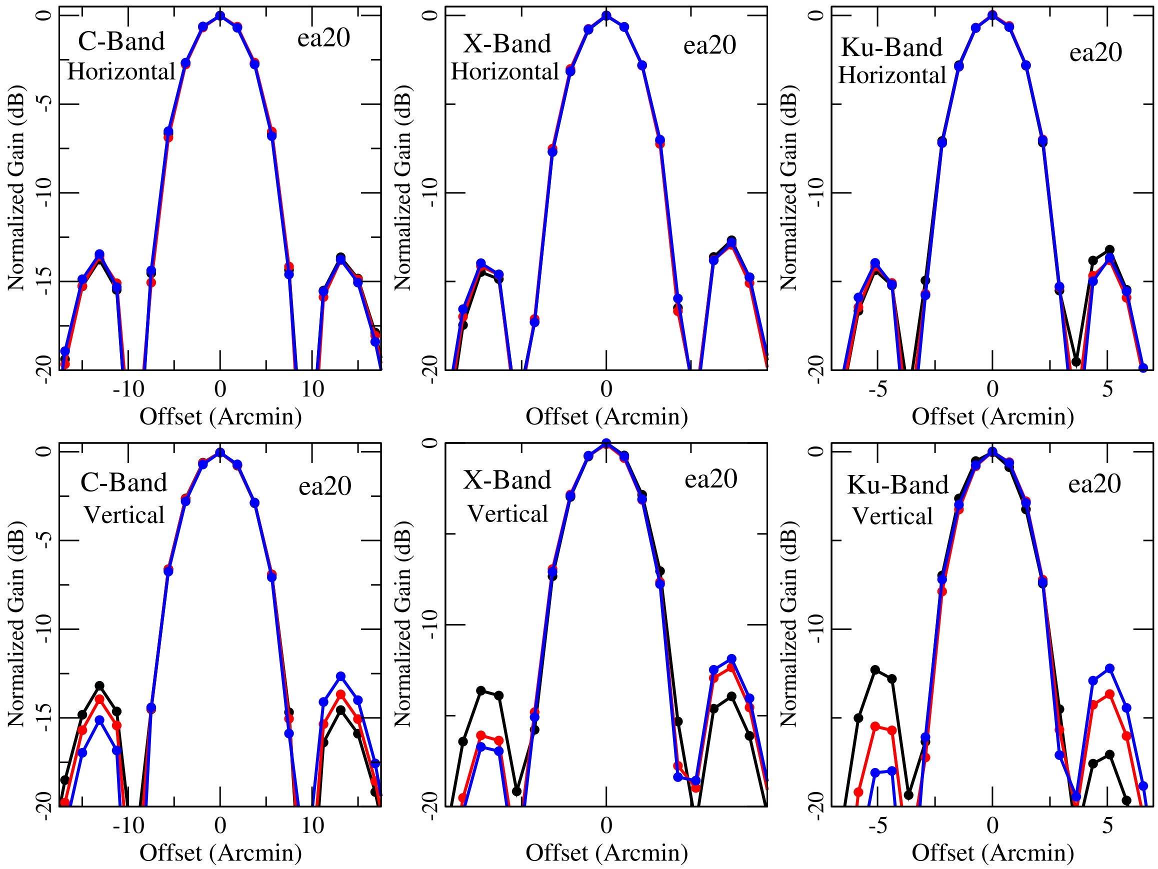

Figure 12: Orthogonal cuts without subreflector rotation applied at C, X, and Ku. The antenna shown (ea20) was selected for minimal imbalance at $E = 60$. The black trace was taken with $E \sim 30$ degrees, the red trace near $E \sim 60$ degrees, and the blue trace near $E \sim 80$ degrees. The variation in vertical SLR is now quite notable, while there is no elevation dependence in the horizontal cuts.

'astigmatism' is seen at Ku and K bands, but is entirely absent at Ka-band. An explanation based on reflector distortion is not tenable with such behavior, which can only be caused by issues related to the feed.

6.1 Normalized Beam Cuts

Although all VLA antennas were constructed to be identical, differences exist, resulting in small but perceptible differences in their beam patterns. Here we show some antenna patterns for selected antennas, chosen to display the range. We plot the normalized patterns – the horizontal axis is expanded by a factor ν_G, (so the patterns could be considered the 'equivalent 1 GHz profiles'), so that all bands are plotted in the same graphs.

In Fig 14 we show these normalized patterns for ea04, ea06, and ea15. Note that the profiles for ea04 show sharp nulls at all bands in both orthogonal cuts, indicating excellent alignment of the subreflector and minimal distortions. Antenna ea06 shows some variations in the nulls in the vertical dimention, notably strongest at middle frequency bands. Antenna ea15 shows significant variations in both cuts at some – but not all – frequencies.

6.2 The Problem with ea01

ea01 is different than all the others – its horizontal profiles are far more deviant than ea15 and ea18. Here we show the problem, and what we have attempted to do to repair it. As with ea15 and 18, it is clear that the problem cannot be repaired by subreflector setting alone. There is more going on.

The performance of ea01 at high frequencies has always been poorer than the other antennas. Email from the 1990s reveal that this problem was recognized at that time, and that the subreflector was moved as far to the left as it would go, in order to improve the performance. Despite this, the high frequency performance of this antenna, from the mid 1990s through to Spring 2020, remained worse than the others. Beginning in March 2020, a series of changes to subreflector positioning was implemented, with only partial success in correcting the

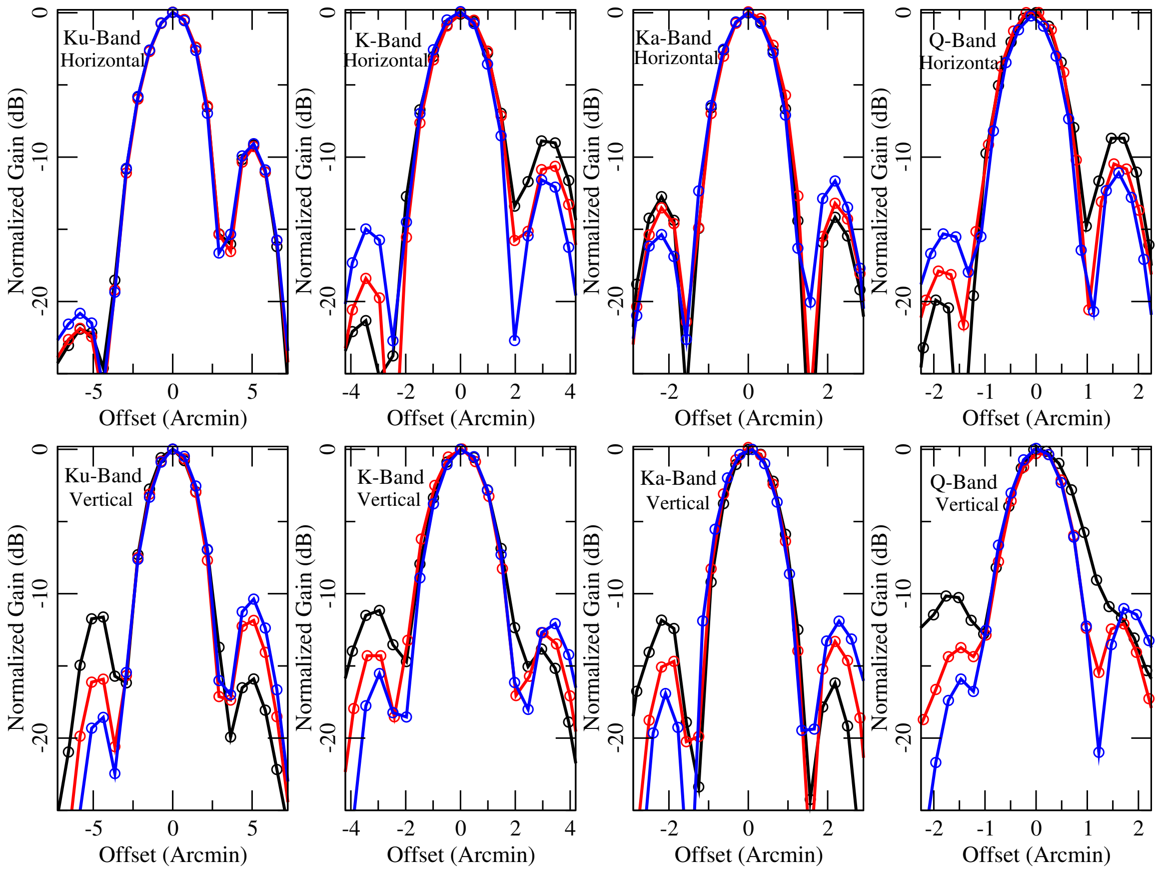

Figure 13: Orthogonal cuts through ea15, at Ku through Q bands. The colors indicate the elevation: black is $\sim$ 30 degrees, red $\sim$ 60 degrees, and blue $\sim$ 80 degrees. This antenna shows a large horizontal offset at Ku, K, and Q bands – but none at Ka-band. The elevation SLR dependency is much larger – $\chi = 15.6$ than any other antenna. The Q-band elevation cuts show strong astigmatism – a feature seen in most antennas at Q-band.

high frequency response. In Figure 15 we show the horizontal cuts through ea01, tracking the evolution of the high frequency performance after making various changes to the subreflector position.

We describe here in some detail the series of operations, resulting in the profiles shown in Fig 15.

- The top row shows horizontal cuts taken in late January 2020. These represent the antenna performance from the mid 1990s through to 2020. Three bands (Ku, K, and Q) show greatly asymmetric profiles, while at Ka-band, the profile is good. If interpreted in terms of subreflector offset, a motion of 15 to 20 mm, to the left, is suggested. But when the antenna mechanics attempted to do this, it was found that the subreflector was already moved to its limit in that direction. A review of emails from the mid 1990s revealed that this asymmetry was noted then, and the subreflector was moved in an attempt to improve the response. As we could not now move the subreflector any further without major changes to the subreflector mount, it was decided to rotate the subreflector. As shown in the following section, a small CCW rotation of the subreflector is equivalent to a leftward shift, in terms of modifying the phase paths.

- The second row shows the response after a CW rotation by 0.5 degrees. In fact, there were two sequential rotations. The analysis based on the Ruze expressions (see the next section) suggested a CCW rotation of 0.5 degrees. But when this was implemented, the profiles – even at Ku-band, showed no effective beam at all. It was then realized that the Ruze expressions presumes the the rotation axis is located at the prime focus. However, for the VLA, the only possible place to insert a shim was at the base of the mounting barrel, located more than 1 meter above the subreflector. The result of this was a rightward shift – in the wrong (positive) direction, in addition to the desired rotation. A rough calculation indicated that the appropriate rotation, taking account of the long lever arm, was by -0.5 degrees from the original position. The profiles shown in the second row of Fig 15 indicated that the rotation was successful, but has overcorrected the originating problem. It was then decided that a positive horizontal shift should complete the changes.

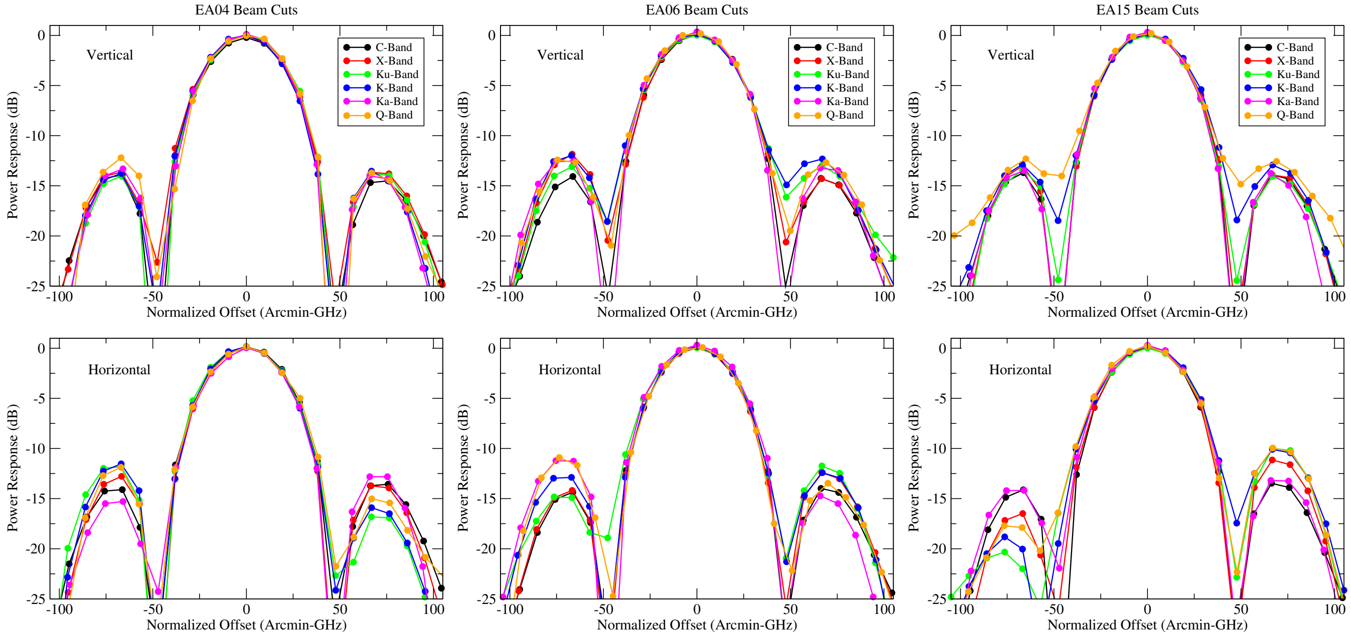

Figure 14: **Left**The vertical (top) and horizontal (bottom) beam profiles for ea04. This antennas has very similar profiles at all bands. **Middle** The profiles for ea06. For some bands, the first nulls are quite shallow. **Right** The profiles for ea15. This antennas has a notable variation in horizontal asymmetry between the bands.

- The third row shows the responses after a +6mm shift of the subreflector to the right. Again, this was done in two states – a 12 mm shift, which clearly overcorrected the problem, and a subsequent -6mm shift, resulting the profiles shown in the third row. The Ku and K-band responses are now close to optimum, while the Ka and Q bands have recognizeable sidelobes, albeit with a large sidelobe ratio. Note also that the main beam profiles at these two bands are far too wide. It is clear that the fundamental alignment issue, responsible for the poor response, remains unknown.

- The bottom row shows the current response, taken in late November, 2020. There are no changes from the profiles taken in July.

In summary, these changes have certainly improved the beam symmetry in ea01 at Ku and K bands – the formerly highly distorted horizontal profiles have been corrected. Unfortunately, at Ka-band, the profile is now much worse than before, while at Q-band, the former asymmetry has been reversed in sign. For both Ka and Q-bands, the primary beam remains far too wide, showing the shape normally associated with a coma lobe. However, the small rightward shift suggested by the observed sidelobe asymmetry will likely not improve the main beam performance.

For all bands, the vertical cuts in ea01 are completely normal – the problem addressed here is associated with the horizontal axis. Although not shown here, the C and X band cuts are also warped, suggested a large (20 mm) rightward shift in the subreflector positioning.

So how can we have such large differences between the bands? The only explanation that we are aware of is in the positioning of the secondary focus feeds. But note that it take a much larger motion of these feeds to balance the beam response than that for the subreflector. Roughly speaking, it is an order of magnitude, so that, for instance, the feed offsets required to balance the beams at C and X bands are of order 20cm! It seems highly implausible that these could be mis-positioned by such an amount.

7 Cassegrain Antenna Optics Basics

To this point, the analysis has been based solely on the observed data – the change in beam characteristics observed as a function of elevation, and of subreflector rotation. No appeal, or connection, to antenna optics has been made. Various physical origins for the observed elevation-dependency can be contemplated – two are suggested in Section 2. In one sense, the identification of the physical origin is not important – the prescription for offsetting asymmetry, and it is very effective in removing the dependency, and restoring the optimal beam

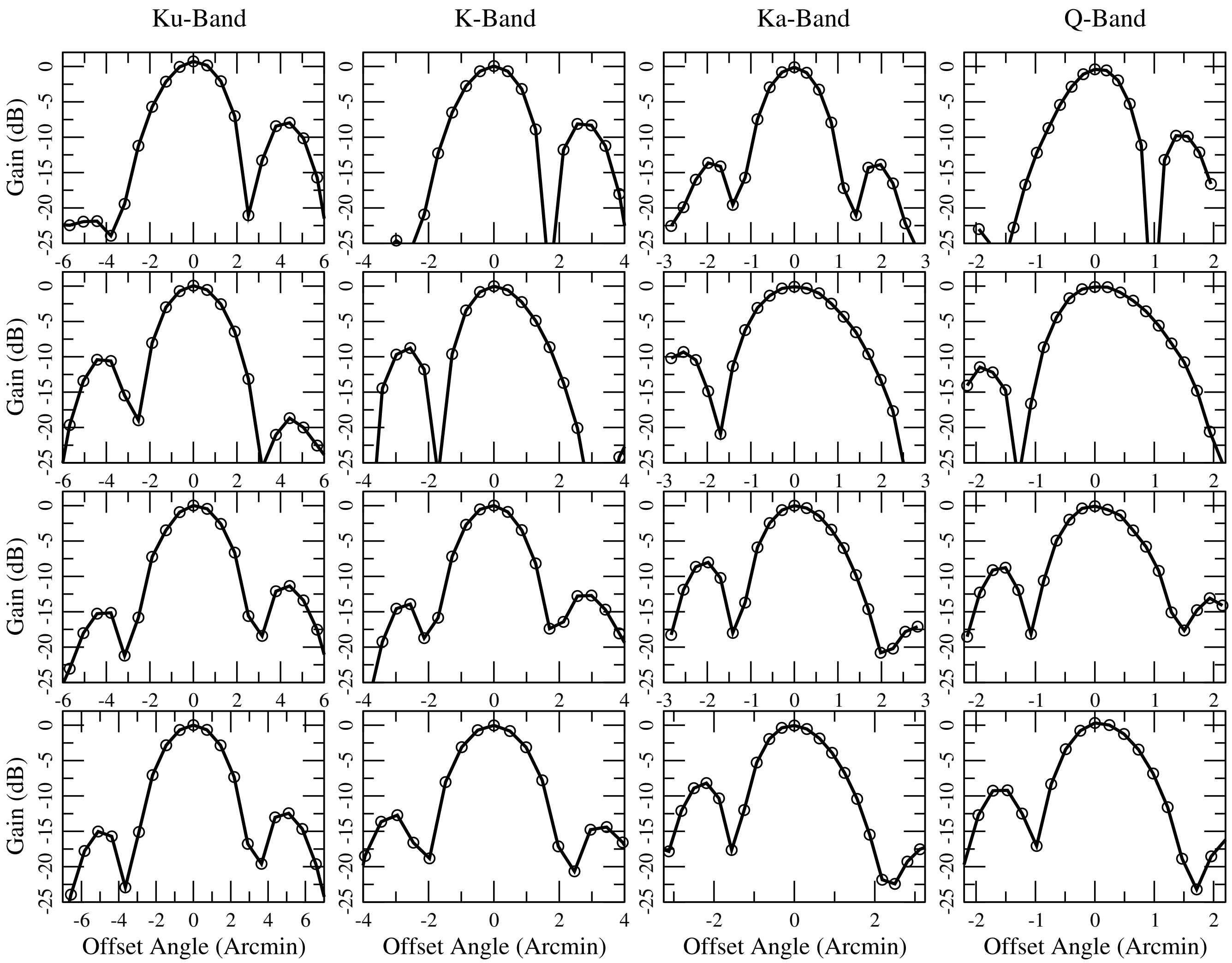

Figure 15: Horizontal cuts through the beam of ea01 at Ku, K, Ka, and Q bands. The rows track the changes resulting from changes to the subreflector positioning. **Top Row** Response prior to 03 Mar 2020. **Second Row** Response following subreflector rotation of -0.5 degrees, mid April, 2020. **Third Row** Response following a horizontal shift of 6mm, to the right, mid-July, 2020. **Bottom Row** Current response, late November, 2020.

characteristics for the high frequency bands. Yet, it is satisfying to understand the origin of the problem at a fundamental level. Here, we utilize John Ruze's theory of the effect of small displacements in the optical elements of a parabolic antenna to show that the two suggested origins of the asymmetry mentioned in the introduction to Section 2 are both highly plausible causes.

The VLA utilizes cassegrain optics, employing a paraboloid main reflector, hyperboloid subreflector, and feed located at the lower (hyperbolic) focus. In the classical design, both reflectors are axisymmetric. The VLA, however, employs a non-axisymmetric subreflector, such that the secondary focus is located 1.06 meters off the paraboloid axis. The purpose of this is to permit location of eight fixed receivers around a circle of that radius. Changing frequency bands is then accomplished by rotation of the subreflector – a much simpler operation than rotating a plotform with eight receivers. In addition, the VLA employs shaped optics – both the subreflector and main reflector deviate slightly (~ 2 cm) from their idealized forms in order to increase the main beam forward gain – at the cost of higher sidelobes.

In a memorandum dated 1969, John Ruze provided an analysis for calculating the phase distributions over the reflecting surface of a paraboidal antenna due to small displacements of the feed and subreflector. His formulations included primary focus-fed systems, as well as cassegrain and gregorian optics systems. Here we use his expressions for cassegrain systems. When combined with a model of the electric field amplitudes over the aperture, these expressions can be utilized to generate synthetic antenna beam responses, whose properties can be compared to those actually measured. The analysis uses simple ray optics, and as such is only valid for wavelengths much smaller than any of the physical structures. As the effects of optics errors are most strongly seen at high frequencies, where the wavelengths are of order 3 cm or less, we expect the use of simple geometric optics to be sufficient.

The classic paraboloid/hyperboloid cassegrain design is defined by three quantities: the focal length of the paraboloid, f, the distance between the two hyperbolic foci, $2c$, and the y-axis intercept of the upper hyperboloid from the mid-point between the foci, a. We show in figure 16 a scale drawing of a symmetrized version of the VLA's geometry, showing these quantities. Utilizing a cartesian coordinate system with the origin at the bottom

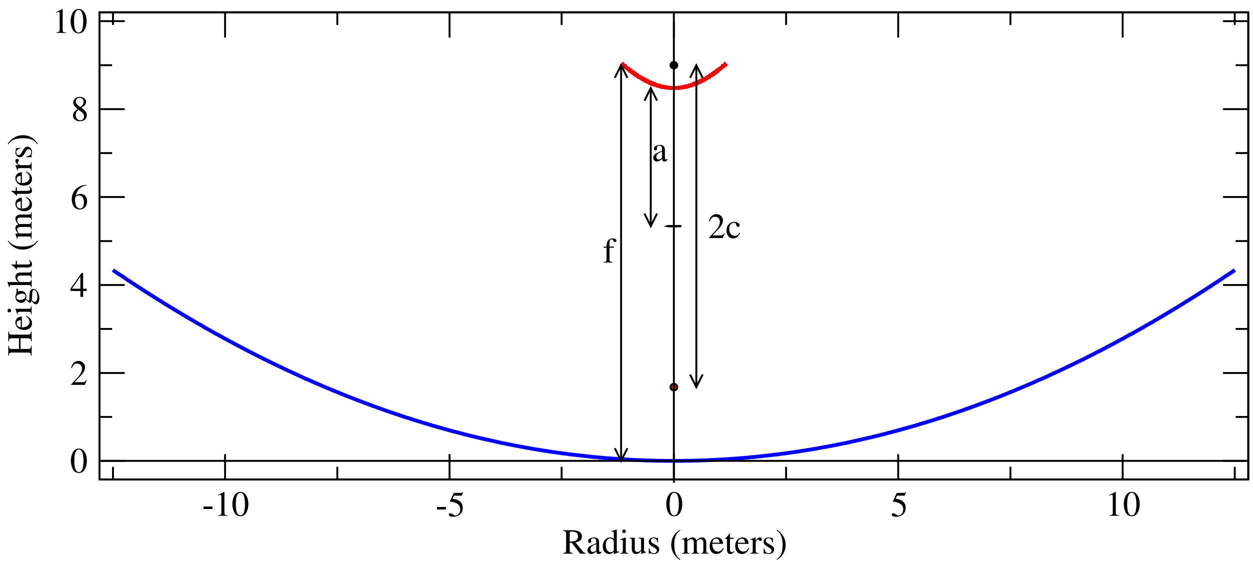

Figure 16: A scale drawing of the VLA's equivalent geometry. For this antenna, f = 9.0, a = 3.140, c = 3.662 – all in meters. The two black dots on the vertical axis identify the upper and lower (primary and cassegrain) foci. The horizontal hash mark on this axis marks the midpoint between the foci.

of the parabolic reflector, the equations for the main and subreflector are given by:

$$y_{main} = \frac{r^2}{4f} \tag{46}$$

$$y_{subr} = f - c + a\sqrt{1 + \frac{r^2}{c^2 - a^2}} \tag{47}$$

where r is the radial offset from the antenna center. For the VLA, $f = 9.0$ meters, $a = 3.140$ meters, $c = 3.662$ meters. From this, the ellipticity $e = c/a = 1.166$, and the magnification, $M = (c + a)/(c - a) = 13.04$.

We now repeat the results by Ruze. To better illustrate the geometrical quantities, a lower-magnification system is more useful than the VLA's geometry. We reproduce Ruze's example system – with M = 7/3 – in figure 17.

Using the following definitions,

$$q = \frac{r}{2f} \tag{48}$$

$$Q = \frac{r}{2Mf} \tag{49}$$

$$h = fq^2 \tag{50}$$

$$e = c/a \tag{51}$$

$$M = \frac{c+a}{c-a} = \frac{e+1}{e-1} \tag{52}$$

Ruze shows that the angles and lengths identified in Fig. 17 are given by:

$$\cos\theta_p = \frac{1-q^2}{1+q^2} \tag{53}$$

$$\sin\theta_p = \frac{2q}{1+q^2} \tag{54}$$

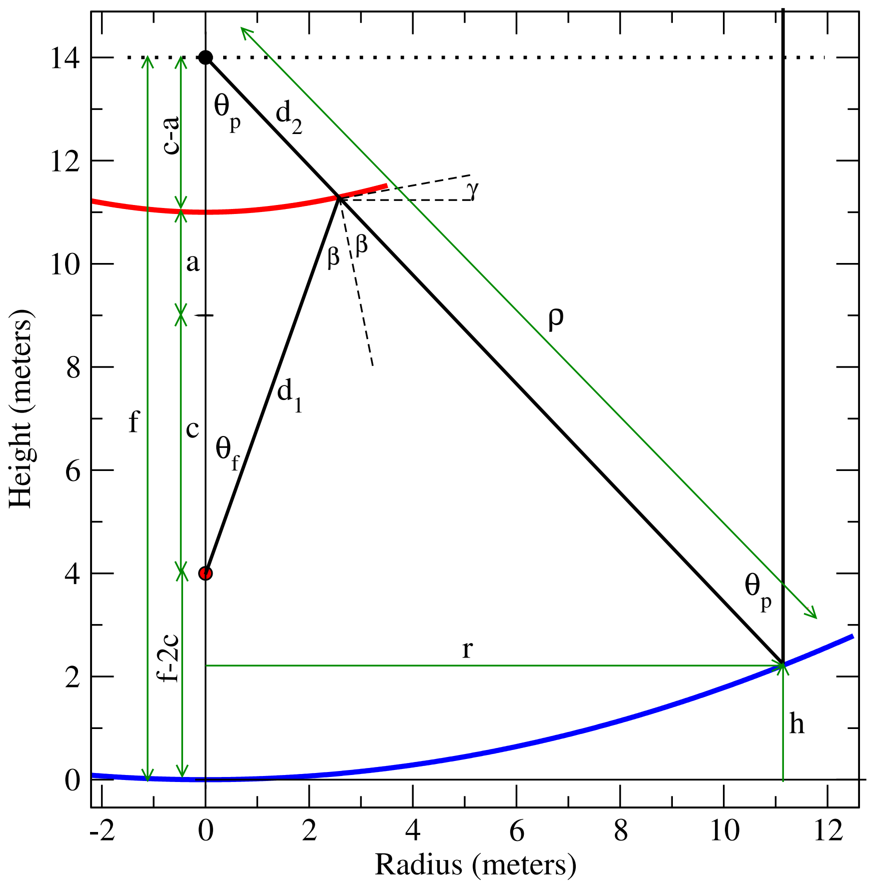

Figure 17: A hypothetical antenna, chosen to illustrate the geometry for perturbations, with f = 14, a = 2, c = 5, so M = 2.33 and e = 2.5.. The black and red dots on the vertical axis identify the upper and lower (primary and cassegrain) foci. The thick black line represents the ray path for on-axis incidence. The horizontal dotted line through the upper (prime) focus is the focal plane, representing the phase reference plane for incoming on-axis radiation.

$$\cos\theta_f = \frac{1-Q^2}{1+Q^2} \tag{55}$$

$$\sin\theta_f = \frac{2Q}{1+Q^2} \tag{56}$$

$$\gamma = \frac{\theta_p-\theta_f}{2} \tag{57}$$

$$\beta = \frac{\theta_p+\theta_f}{2} \tag{58}$$

$$d_1 = \frac{a(1-e^2)}{1-e\cos\theta_f} \tag{59}$$

$$d_2 = \frac{a(e^2-1)}{1+e\cos\theta_p} \tag{60}$$

$$\rho = f+h \tag{61}$$

Note that the length ρ is the entire distance from the antenna surface to the primary focus.

In Figure 17, the horizontal dotted line passing through the focus, and perpendicular to the antenna axis, represents the phase front of an incoming EM wave. It is easily shown that the distance along the ray path from this surface to the primary (upper) focus is constant for all radial offsets r, and is equal to

$$D_1 = 2f \tag{62}$$

while the distance for all rays to the secondary (lower) focus is also constant for all offsets r, and equal to

$$D_2 = 2(f + a). \tag{63}$$

With this model, and employing scalar plane wave theory, Ruze (1969) provides convenient expressions for the path length differences resulting from small displacements of the subreflector and feeds, for prime focus, cassegrain, and gregorian systems. For the Cassegrain geometry of our simplified (axisymmetric) VLA antenna model, the relationships are given in Table 9, both in terms of the ray angles θ_p and θ_f, (defined in figure 17), and in terms of the normalized radial coordinates $q = r/(2f)$, and $Q = r/(2Mf)$. The first two rows in the Table show the path length perturbations due to displacements of the cassegrain feed. The central three rows show the perturbations due to subreflector offsets. The bottom two rows show the perturbations due to displacements of a prime focus feed, and are present only for comparison to our cassegrain system. The variable Δz represents an upwards vertical (focus) offset, while Δx represents a transverse displacement to the right, as viewed from behind. The tilt $\Delta\alpha$ is the rotation of the subreflector about an axis perpendicular to the bore-sight direction. The azimuthal angle ϕ is defined with respect to an axis defined by the direction of positive transverse displacement Δx or tilt $\Delta\alpha$.

Table 9: **Path Length Errors for Cassegrain and Prime Focus Optics**

Offset Error	**Path Length Change**	**Path Length Change**
Cassegrain Feed Vertical Offset (Focus)Δz	$-\Delta z \cos\theta_f$	$-\Delta z \frac{1-Q^2}{1+Q^2}$
Casegrain Feed Lateral Offset Δx	$-\Delta x \sin\theta_f \cos\phi$	$-2\Delta x \left(\frac{Q}{1+Q^2}\right) \cos\phi$
Subreflector Vertical Offset (Focus)Δz	$\Delta z(\cos\theta_f + \cos\theta_p)$	$\Delta z \left(\frac{1-Q^2}{1+Q^2} + \frac{1-q^2}{1+q^2}\right)$
Subreflector Lateral Offset Δx	$\Delta x(\sin\theta_f - \sin\theta_p)\cos\phi$	-2$\Delta x \left(-\frac{Q}{1+Q^2} + \frac{q}{1+q^2}\right) \cos\phi$
Subreflector Tilt $\Delta\alpha$	$\Delta\alpha(c-a)(\sin\theta_p + M\sin\theta_f)\cos\phi$	$2\Delta\alpha(c-a)\left(\frac{q}{1+q^2} + \frac{q}{1+Q^2}\right)\cos\phi$
Prime Focus Feed Vertical Offset Δz	$\Delta z \cos\theta_p$	$\Delta z \left(\frac{1-q^2}{1+q^2}\right)$
Prime Focus Feed Lateral Offset Δx	$-\Delta x \sin\theta_p \cos\phi$	$-2\Delta x \left(\frac{q}{1+q^2}\right) \cos\phi$

The variable q is the scaled radial offset: $q = r/2f$, where f is the focal length. The variable $Q = q/M$, where M is the magnification. For the VLA, $f = 9.0$ meters, $M = 13.0$

The magnitudes of these errors are shown in Fig. 18, for 1 cm displacement in the feed (both prime focus and cassegrain) and subreflector[3].

Some comments are appropriate at this point:

- *Vertical (Focus) Displacements* These are shown in blue in Figure 18. The path length error due to a 1cm upwards subreflector focus displacement (offset by 2 cm) is shown in solid blue. For comparison, the path length error for a 1cm upward prime focus vertical displacement is shown (offset by 1cm) in dashed blue, and is indistinguishable from that of a 1cm displacement of the subreflector for Cassegrain optics. In contrast, a 1 cm upward displacement of the secondary focus feed, (offset by 1cm), shown in the dot-dash blue, causes a very small path length error in the radial distribution, a result of the antenna magnification, which greatly extends the depth of the focal spot.

- *Lateral Offset Errors* These are shown in red. The dot-dash line shows the nearly planar slope due to a horizontal offset in the cassegrain feed position. The dashed red line shows the path length change induced by an offset in the prime focus. The change due to a lateral offset in the subreflector position is shown in the solid red line. It is slightly less than, but similar in shape to, the perturbation due to a prime focus offset.

- *Pointing Offset Adjustment* In all cases, the first-order effect of a lateral shift is a pointing offset, a result of the first-order expansion (mean slope) of the path perturbation. In practice we remove the pointing error caused by a lateral shift of the subreflector by tilting the antenna pointing position by the beam offset.

[3]In this figure, the vertical offset pathlength errors have been offset to zero at zero radius. This is not an issue for the calculation of the beam patterns, as a phase offset is removed in calibration, and does not affect the beam shapes.

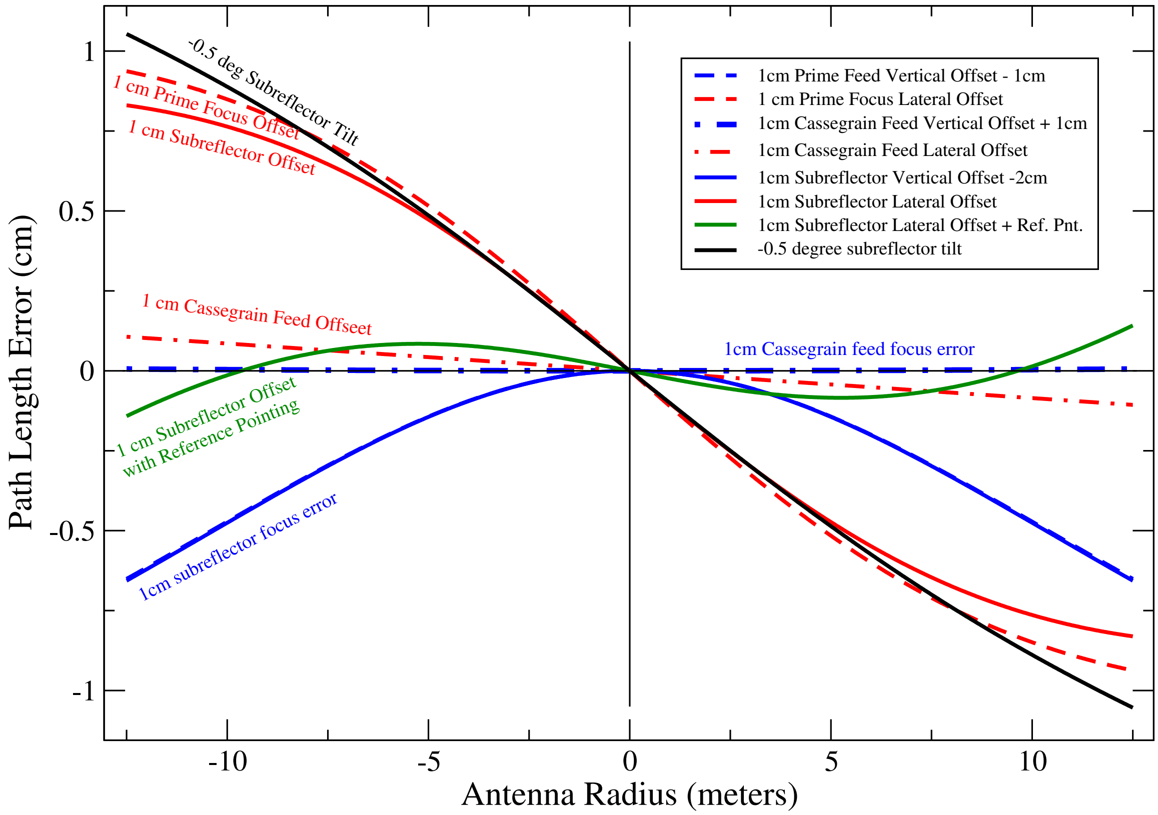

Figure 18: The excess path lengths due to a displacement of 1 centimeter for a prime focus feed, Cassegrain focus feed, and subreflector, for a VLA antenna using the approximations of Ruze. The dashed lines show the dependencies on prime focus displacements, the dot-dash lines show the dependencies on Cassegrain feed displacements, and the sold lines show the dependencies due to subreflector displacements. Red denotes lateral offsets, blue denotes vertical (focus) offsets. The sold black line shows the effect of a -0.5 degree subreflector tilt, and the solid green line shows the net path length perturbations after removal of the first-order term from repointing the beam. These plots show that the required positioning accuracy of the Cassegrain feeds is much less than that of the subreflector – by a factor close to the magnification factor M for a lateral error and M^2 for the focus.

The effect on the aperture phase is to remove a linear slope, leaving the higher-order curvature terms. The residual in the path difference is shown by the solid green line. It is the anti-symmetric curvature in this function which creates the asymmetric sidelobes of the antenna beam.

- *Cancelling Effects* The effects of these perturbations can offset, or augment, one another. For example, a 1 cm horizontal offset, with a +0.5 degree subreflector tilt, will essentially cancel the first-order term (they have the same initial slope in Figure 18), resulting in no observed pointing errors. However, as the curvature terms are different, the observed beam asymmetry will be reduced, but not eliminated. Similarly, if, due to simple torque imbalance between the vertex mass and the counterweight, the antenna mispoints, the resulting linear path length slope could remove part, or all, of the linear portion of the subreflector sag or tilt path perturbation, leaving only the third-order term.

The radial path-length dependencies shown in Fig 18 are one-dimensional – cuts across the two-dimensional aperture along the axis of maximum effect. As the beam is formed from the two-dimensional distribution of electric field amplitude and phase over the aperture, it is more informative to view the path errors over the full two-dimensional aperture. To illustrate these, we show in Figure 19 the excess path length distributions, now in terms of phase at $\lambda = 9.28$mm, for a 1cm displacement of the subreflector in focus, and a similar offset in lateral offset. The left panel shows the phase distribution (offset to zero at the dish center) due to a subreflector focus offset. The 1cm error results in a $\sim$25 degree phase differential over the antenna equivalent radiating surface. The middle panel shows the effect of a 1 cm horizontal displacement of the subreflector. A strong gradient, with nearly two turns of phase from rim to rim, is generated. The first-order effect of this is to shift the beam response angle. After removal of this first-order term (a slope of 70% of the phase derivative at the antenna center), corresponding to a 2.5 arcminute pointing offset correction, the resulting phase distribution is shown in the right panel. This non-symmetric distribution is responsible for the observed beam asymmetries.

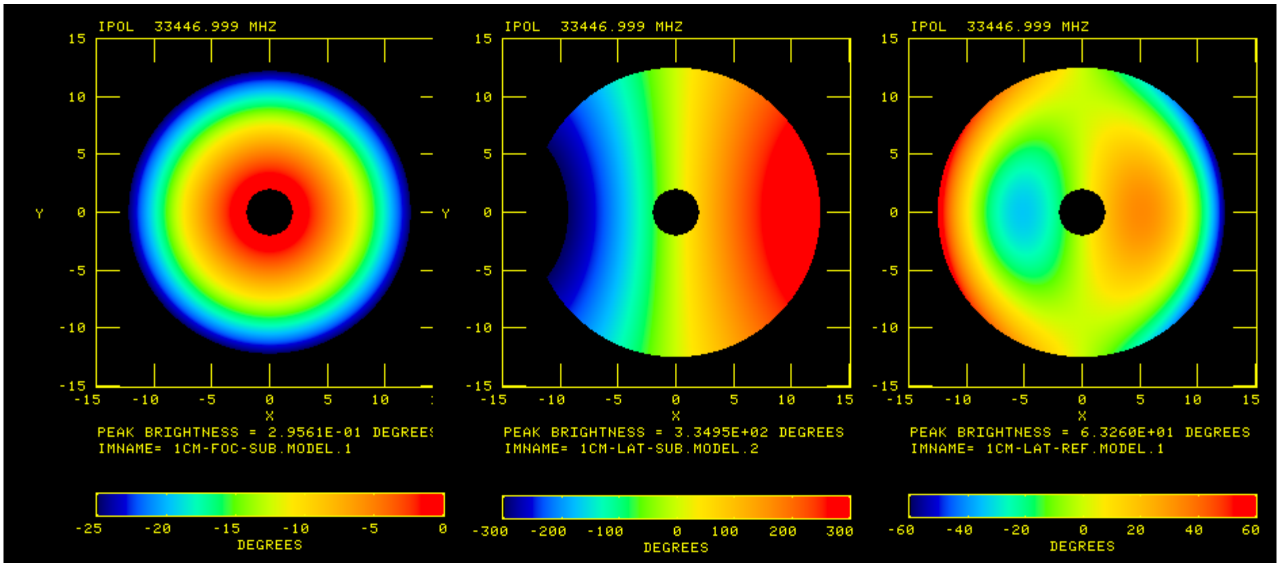

Figure 19: **(Left)** The aperture phase distribution over a VLA antenna caused by a 1cm focus displacement of the subreflector at $\lambda = 9.28$mm. **(Middle)** The aperture phase error distibution from a 1cm lateral offset of the subreflector in the azimuthal direction.**(Right)** the aperture phase distribution from a 1 cm transverse displacement, with the antenna repointed by 160 arcseconds to shift the primary beam to the center. The axis values are in meters. The central black hole represents the unpaneled area populated by the cassegrain feeds.

Figure 18 shows that the first-order (linear) term of the induced phase gradient for a 0.5 degree tilt is about the same as that of a 1 cm lateral shift. Hence, a 0.1 degree tilt, or a 2 mm shift, of the subreflector, is expected to cause a ~ 30 arcsecond offset of the beam. However, the third-order curvature, and thus the sidelobe asymmetry and loss of forward gain, due to a tilt is seen from Figure 18 to be much less than that due to the horizontal translation resulting in the same beam offset. Hence, the beam asymmetry, for a given pointing offset, will be less for a 'tilt' than a shift.

8 Synthesizing the Beam Pattern Response

The path length variations created by small misalignments in the antenna optics lead to easily recognized changes in the antenna sidelobe response. Measurement of these will provide us a simple means for determining the needed positional offsets in the subreflector and feeds.

The discussion in the previous section gives the fundamentals. To better demonstrate the expected effects on the antenna beam of small focus errors, we have generated simulated beams with known focal errors. To do this, a modified version of the `AIPS` task 'HOLOG' was generated. In standard useage, 'HOLOG' produces images of the illumination phase and amplitude distributions over the antenna aperture by Fourier transformation of holography data. Included in the program is an estimation of the subreflector alignment errors, derived through fitting the observed aperture phase distribution to the Ruze model. These optics-induced errors need to be removed from the holography data before an accurate model of the antenna surface can be derived.

For this memo, HOLOG was modified to reverse the process – to permit calculation of the phase perturbations across the antenna aperture caused by a known offset of the subreflector or secondary focus. These perturbations are calculated using the Ruze expressions summarized in Table 9. We generated predicted antenna beam images by taking using the holographic data from a 49 x 49 raster sampling of ea02 at 32 GHz, retaining the voltage amplitudes, and replacing the observed phases with the perturbations predicted by the Ruze model. The predicted beam is then generated by Fourier transform of the modified data. By doing this, the effects of the aperture amplitude weighting, including the presence of the central unpanelled area (2 meter radius), and shadows of the quadrupod support legs are accounted for.

8.1 Focus Offsets

In Fig 20 we show the effect on the primary beam of a progressive increase in the subreflector focus error, in steps of 0.11λ, from 0 through 0.53λ. The major effects of a focus error are the filling in of the first null, a decrease in the forward gain, and a rise of the first sidelobes w.r.t. the main beam. Note that primary beam width – as measured by the FWHM, (relative to the defocussed maximum) is hardly affected by a focus error.

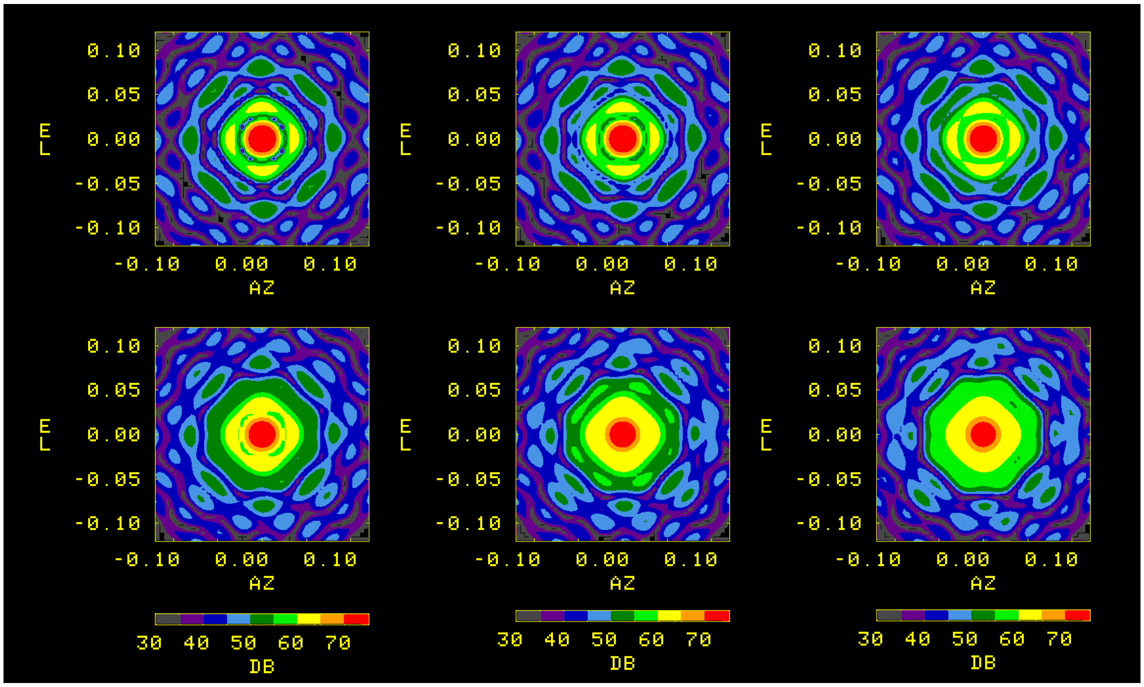

Figure 20: Simulations of the VLA's power beam, as a function of increasing subreflector focus (vertical) position in steps of 0.11λ, from zero through 0.53λ. The most striking effect is the filling in of the first null, and its replacement with a broad plateau (yellow) of increasing gain. The FWHM of the beam is hardly affected by these modest focus errors. The color scale is adjusted to approximately that of the forward gain in DBi at a wavelength of 9.28 mm.

The loss of forward gain, and the rise of the first sidelobes are shown as functions of the focus offset in Fig 21. The simulations show that small subreflector focus errors can cause a notable loss of gain – a 0.3λ offset creates

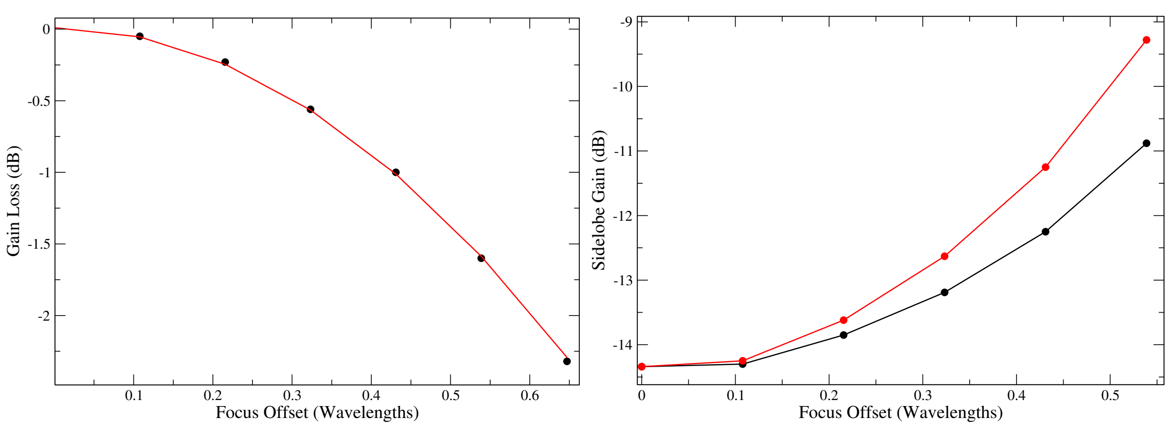

Figure 21: (Left) The beam power loss, in dB, as a function of subreflector focus offset. The data are well fitted by $\Delta P_{dB} = -5.5(\Delta z/\lambda)^2$ (red curve). (Right) The ratio of the first sidelobe power gain to that of the main beam, in dB, as a function of the subreflector focus error. The black curve is the ratio to the main beam with zero focus offset. The red curve is the ratio to the peak of the defocussed beam.

a 10% loss, and a 0.5λ error gives a 30% loss in forward gain. At the VLA's highest frequency, this corresponds to 2 and 3 mm, respectively. Although the FWHM of the antenna beam is hardly affected by the misfocus, the effect on the inner sidelobes and nulls is dramatic – relative to the peak, the first sidelobe rapidly rises, and the chracteristic null between the main beam and first sidelobe rapidly disappears.

It needs to be emphasized that subreflector focus errors give both a large phase change to the antenna phase, and a large phase gradient across the beam. A perturbation of Δz changes the antenna phase by $\sim 600\Delta z/\lambda$ degrees. If stable between observations of the target and calibrator source, this will be removed by calibration. More serious is the phase *gradient* introduced by the error. The center-to-edge phase difference across the antenna suface, due to an error of Δz is $\sim 260\Delta z/\lambda$ degrees – even a 1 mm error at 1cm wavelength – which has negligible effect on the antenna gain – will generate a 26 degree gradient across the primary beam. This cannot be removed by basic calibration and, if all antennas have different residual delay errors, will severely restrict image fidelity of bright, extended objects.

The effect on the antenna gain of a vertical (focus) error in the cassegrain feed position is very much reduced compared to that of the subreflector, by roughly a factor of M^2 – roughly a factor of 170 for the VLA.

8.2 Lateral Subreflector Offsets

Similar calculations were made of the effect of a lateral offset of the subreflector, as shown in Fig 22. For these simulations, the subreflector was offset from 0 to 2.16λ, in steps of 0.27λ, at a frequency of 32 GHz.

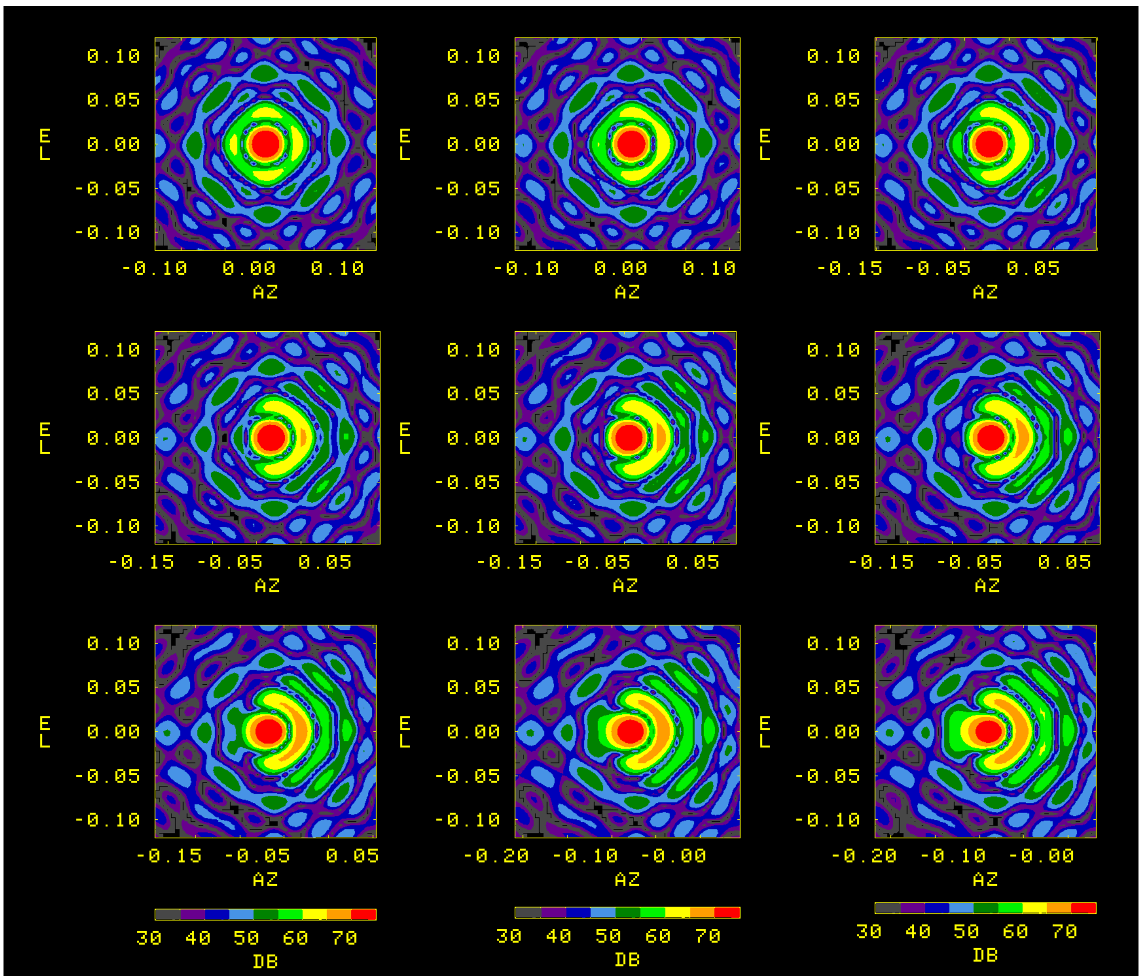

Figure 22: The simulated beam shapes for positive (to the right, looking outwards) subreflector horizontal offsets of 0 through 2.16λ, in increments of 0.27λ, from upper left through lower right. The beam center shifts to lower azimuth (to the left). These pointing offsets of the beam center have been removed in the panels so the beam appears to stay centered. A large coma lobe develops on the side of the beam between the offset maximum and the zero-offset beam position – on the right side in our case. The color scale is appropriate for the gain at 9.28 mm wavelength. The axis labelling is in degrees.

The spatial phase perturbation over the antenna aperture due to a horizontal offset consists of odd powers of the radius. The dominant term is the first which, being a phase ramp, results in an angular offset of the antenna response pattern. Such a pointing offset is removed by the referenced pointing methodology, so the effective phase perturbation over the aperture has the linear term removed, resulting in the distribution shown in Fig. 19. Due to the two-dimensional aperture, the observed beam offset is less than that corresponding to the phase slope at zero radius shown in Figure 18. The calculations by Ruze, and the observations reported below, indicate that the effective two-dimensional phase slope over the aperture is ∼70% of the geometric offset of the subreflector as seen from the center of the main reflector.

The offset of the main beam due to the horizontal misalignment is shown in Figure 23. The left panel shows

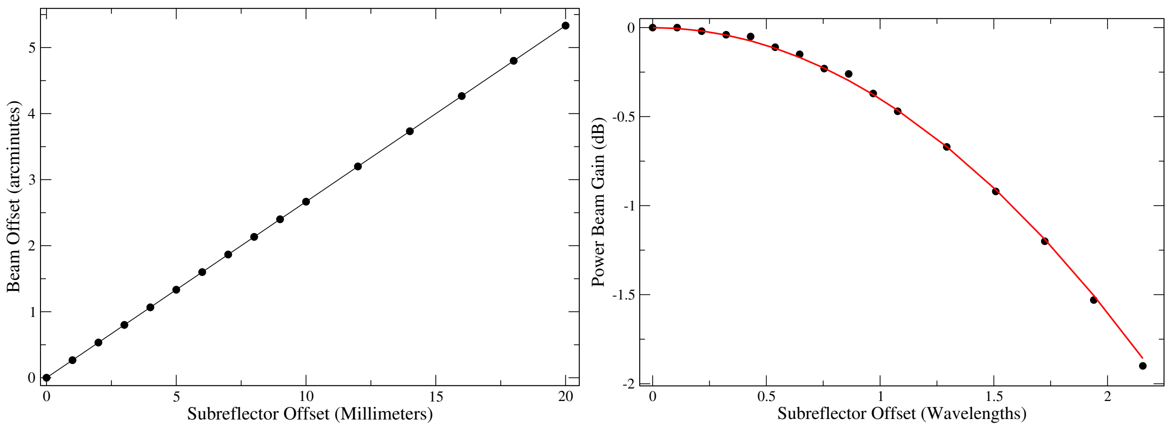

Figure 23: (Left) The calculated beam throw as a function of horizontal subreflector offset. The relationship is linear, at 16 arcseconds per millimeter of offset. Observations with an 8mm offset (described below) gave an offset of 120 arcseconds. (Right) The loss of forward gain as a function of subreflector offset displacement, in wavelengths. The red line shows the fit $\Delta P_{dB} = -0.40(\Delta x/\lambda)^2$.

that for subreflector misalignments of up to at least 2 centimeters, the beam pointing offset is 16 arcseconds per millimeter of subreflector offset. This is 70% of the geometric angle of 1/9000 radian, or 22 arcseconds per millimeter of offset. The difference is due to the illumination taper of the feed, the two-dimensional aperture, which reduces the effective weight of the signals from the outer parts of the main reflector, and the third-order path length curvature, due to the f/d ratio. The right panel shows the loss of forward gain associated with the subreflector offset. Note that this gain roll-off is much less severe than that due to a focus offset of similar magnitude. The gain loss, in dB, is well modeled by $\Delta P = -0.40(\Delta x/\lambda)^2$. Note that the direction in which the beam is moved due to a lateral offset is opposite to the offset direction – an offset of the subreflector to the right (as seen from behind the antenna) results in a beam offset to the left (lower azimuth). This is true for offsets in the prime focus, subreflector, and cassegrain feed.

The odd-symmetry path errors, following the removal of the first-order linear slope, are responsible for the asymmetry in the sidelobe response. The dominant effects for the VLA antennas are the rapid growth of one sidelobe (the coma lobe), and a rapid diminishment of the opposite sidelobe. In Fig 24 we show the growth of the coma lobe, and of the ratio of the innermost sidelobes on each side of the main beamn as a function of the subreflector offset. The sidelobe assymetry ratio (right panel in Fig 24) is a very strong function of the misalignment of the subreflector. The black points are from the model, the colored points are actual measurements, described in Section 9. The relation between sidelobe asymmetry and subreflector offset is approximately linear out to an offset of $\sim 0.8\lambda$, with a slope of 14 dB per offset in wavelengths. A displacement as small as 0.1λ (less than 1 mm at our two highest frequency bands) causes an easily measured sidelobe difference of more than 1 dB – 25%. It is this sensitivity which enables us to define a simple method of determining subreflector positional errors.

8.3 Subreflector Tilt Effects

We have also applied the Ruze expressions to simulate the beam response for subreflector tilts. The results are similar in form to those for subreflector offsets, but with different coefficients. We find the sidelobe ratio (SLR) increases at a rate of 15 dB/$\Delta\theta_{deg}\lambda_{cm}$ where $\Delta\theta_{deg}$ is the tilt in degrees,λ_{cm} is the wavelength in centimeters. The forward gain loss declines with as $\Delta P_{dB} = -0.5(\Delta\theta_{deg}/\lambda_{cm})^2$ dB, and the beam offset (pointing error) is 6.7 arcminutes per degree of tilt.

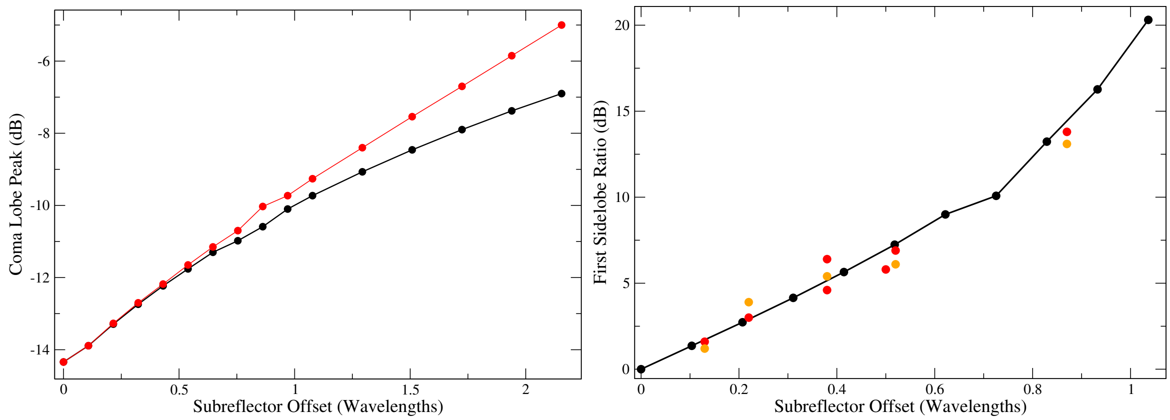

Figure 24: (Left) The growth of the coma lobe as a function of the subreflector offset in wavelength. The black curve is the ratio of the coma lobe gain to that of the main beam with zero offset. The red curve is the ratio of the coma lobe to the main beam of the perturbed beam. (Right) The ratio of the sidelobes on each side of the main response as a function of subreflector offset. The diminished sidelobe vanishes for offsets greater than $\sim 1\lambda$. Plotted on this curve are the actual measurements made with horizontal (red) and vertical (yellow) offsets. These are described later in this report. The slope in the linear region is 14 dB/wavelength of offset.

8.4 Subreflector Rotation Effects

The Ruze model, based on an axisymmtric antenna geometry, does not give predictions of the phase distortion due to a rotation of the VLA's subreflector. Hence, the distortions introduced by such rotations must be measured directly, as described in Section 3.1.2.

8.5 Beam Width Changes

A displacement of the subreflector also results in a widening of the beamwidth, most sensitively at the lower levels. Shown in Fig 25 are the beamwidths at the -3, -6, and -10 dB levels (relative to the maximum), normalized to the full width at half maximum (FWHM) for a perfectly focussed system. For both the transverse

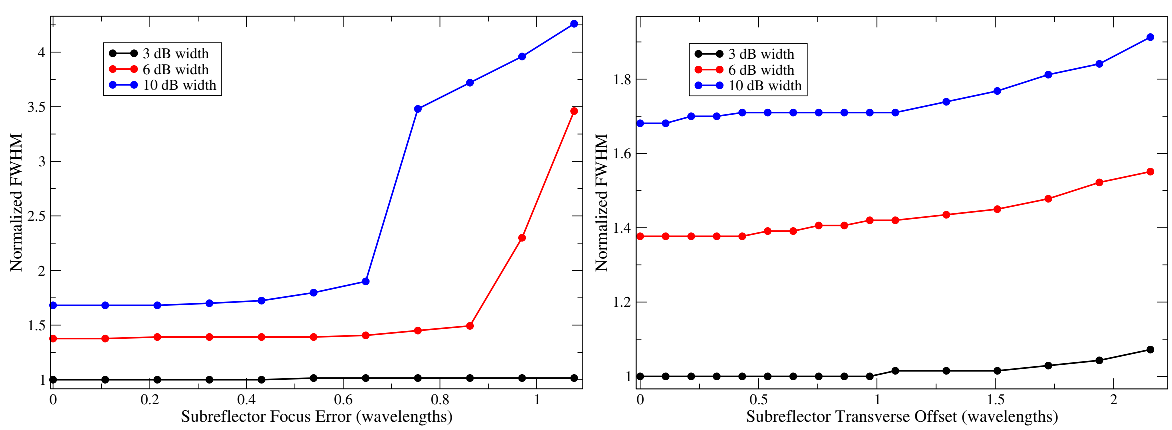

Figure 25: **(Left)** The broadening of the antenna response as a function of a vertical offset (focus) error, at the -3, -6, and -10 dB levels. The dramatic 'jump' in beamwidth at -6 and -10 dB is due to the rise of the unfocussed plateau. **(Right)** The broadening of the antenna response as a function of a transverse offset error, at the -3, -6, and -10 dB levels.

and vertical offsets, the -3 dB (half power) widths are largely unaffected by the scale of offsets considered. The effects on the lower levels are much stronger, which reflects the distinct asymmetry in the beamshapes created by these optics misalignments, as seen in Figure 22.

8.6 Offsetting Distortion Origins?

Although the beam simulations shown above are a very good match to the observed beam asymmetries, the predicted pointing offsets with increasing distortion (i.e., decreasing elevation) are not seen in the observations. For example, an observed 15 dB SLR (observed at Ku-band at 20 degree elevation) could be caused by a 2 degree tilt of the subreflector, or a 1.5 cm offset of the subreflector. But such perturbations would be accompanied by large pointing offsets – 13 arcminutes for the tilt, and 3 arcminutes for the subreflector offset. Such large pointing offsets are never seen – the largest observed is about 0.5 arcminutes.

This makes it clear that there is likely more than one distortion mechanism at work, the combinations of which are offsetting the pointing error, but not the distortion. The simplest explanation is that a tilt of the overall structure – lowering the beam from the nominal pointing position without any 'bending' or distortion is offsetting the pointing change due to a subreflector sag or tilt. A downwards pointing error shortens the path length from source to the upper edge of the antenna (without introducing curvature), while a downward offset of the subreflector lengthens the path (and introduces curvature). Combining the two could be cancelling out the first-order vertical phase gradient. Thus, we feel the likely explanation for the unexpectedly small observed pointing error is a comination of a simple sag of the overall structure partially balanced by a sag of the subreflector w.r.t. the main dish.

9 Subreflector Offset Calibration Tests

The results shown in Section 8 are from simple ideal antenna simulations, using the axisymmetric Ruze model to predict the phase perturbations due to misplaced optics. The VLA's antennas are not ideal – they have quadrupod support legs, tensioning cables, significant central blockage due to the subreflector and Cassegrain feed horns, and utilize a non-axisymmetric geometry. We thus do not expect that the simulations and estimates from the Ruze axisymmetric, unblocked model to accurately reproduce reality. We do, however, expect considerable similarly, with perhaps a simple scaling factor linking the model predictions with the actual system performance. To determine these factors, we have undertaken measurements of changes in the antenna beam characteristics due to known induced displacements of the subreflector. Three different tests were executed in July and August of 2017 – a subreflector vertical (focus – 'z') displacement, and two subreflector lateral offset displacements, one in the horizontal ('x'), the other in the vertical ('y') direction.

9.1 Vertical Displacement (Focus) Calibraton

For the vertical (focus) offset test, the subreflectors for antennas 17, 19, 21, 22, 26 and 28 were displaced by 5mm – positively (upwards) for antennas 22, 26, and 28, and negatively (downwards) for antennas 17, 19 and 21. A small raster (9 x 9, with oversampling of 1.2) was done for these antennas at Ka-band before and after the subreflector was moved. The 'HOLOG' program was then utilized to solve for the displacements, utilizing the phase error patterns described in Section 8. The effect of a subreflector focus error on the data, and the fitted model, are shown in Figure 26 for antenna 19.

The results of the focus fitting for all six antennas are shown in Table 10. The mean of the absolute values

Table 10: **Results from Focus Displacement Test**

Antenna	Displacement	HOLOG Solution
17	-5mm	-4.3mm
19	-5	-4.1
21	-5	-5.9
22	+5	+4.0
26	+5	+5.9
28	+5	+5.2

is 4.9, the dispersion is 0.8mm. The agreement between the known offsets and the HOLOG solutions is quite good. We conclude that HOLOG correctly finds the focus offset with an accuracy of about 1 mm at a frequency of 34 GHz.

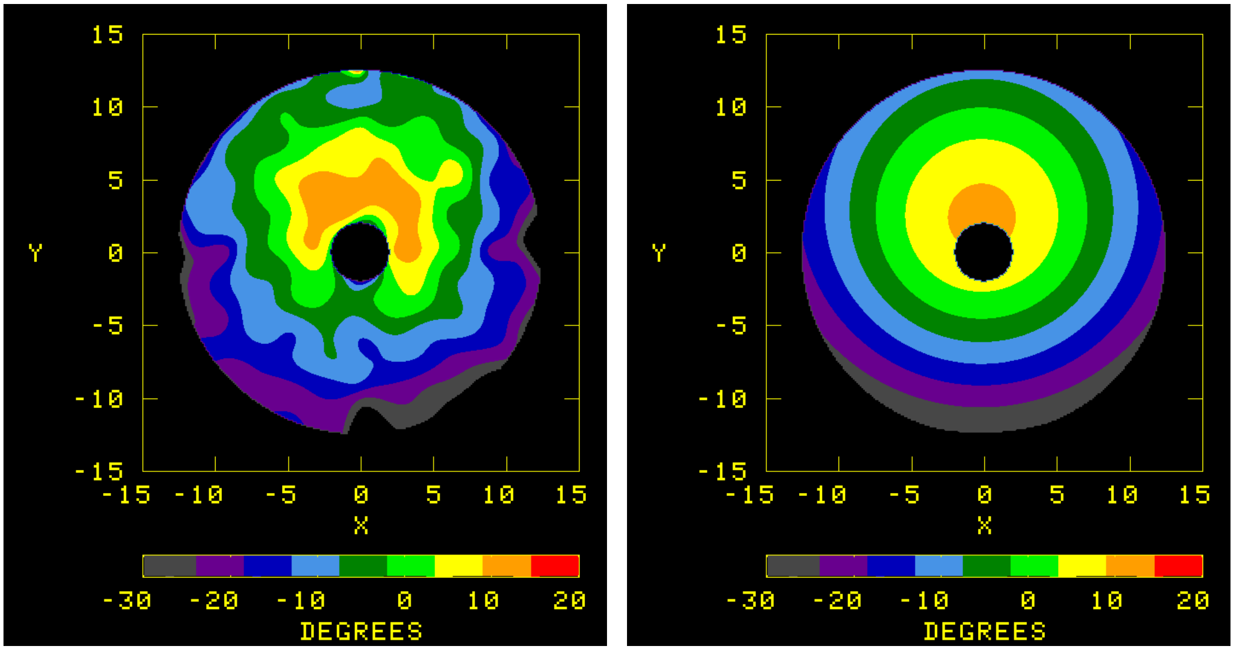

Figure 26: The phase data and model from the HOLOG program. Left Panel: The difference in the phase over the aperture after the subreflector has been moved downwards 5mm. Right Panel: The model phase fitted by HOLOG. The program found a change of -4.1 mm. The offset in the phase pattern is due to a residual pointing offset.

9.2 Lateral Displacement (Nudge) Tests

For this test, on 02 August, 2017, the antenna mechanics displaced the subreflector of ea20 by 8 mm – first in the horizontal (x) direction to the left (as viewed from behind), then (after restoring the x-offset), downwards (y) by the same amount. With the conventions adopted here, both shifts are negative. The effects of these displacements were measured by taking horizontal and elevation cuts through the beam, before and after each 'nudge', at all bands between C and Q. After these measurements, the subreflector was returned to its initial position, and cuts taken through the beam at X and Ku bands to confirm the accuracy of the return.

Additional data were obtained from a +3.5mm horizontal translation of the subreflector of ea05, done on 20 June, 2019. This was a permanent move, as the beam cuts procedures discussed earlier in this memo showed the subreflector required a shift of about this size for the high frequency bands.

Typical horizontal and vertical beam profiles from the two 'nudge' tests are shown in Figure 27, from the observations taken at Ka band. Immediately apparent is that the modest offset of -8 mm results in a dramatic change in the asysmmetry of the innermost sidelobes. Note that the leftward (negative) subreflector shift results in growth of the left-side (lower azimuth) coma lobe. The downward (negative) shift results in the growth of the coma lobe on the left (negative) side of the vertical beam cut. Hence, for both, a negative shift generates a more negative SLR. Thus, to correct an observed negative SLR, a positive (to the right, or upward) move of the subreflector is required. These observed patterns agree with the simulations shown in Figure 22.

The beam cuts give easily-measured values of the innermost sidelobes. The ratios (in dB) of the two sidelobes from the August 2017 test, and the June 2019 move in ea05, are plotted as colored points, as a function of the offset in wavelengths, in the right-hand panel of Figure 24, and show good agreement to the model calculations, shown by the black line. The slope in the linear region is 14 dB per wavelength of lateral offset. It appears that the linear relationship can be used out to an offset of the subreflector of $\sim 0.8\lambda$. For offsets greater than 0.8λ, one sidelobe disappears, so the best measure of the offset is the value of the remaining sidelobe w.r.t. the main beam. The relation in this case is shown by the red curve in the left panel of Figure 24. Here, the slope is 4.0 dB/wavelength, with an offset at zero subreflector offset of -13.7 dB. Using these relations, we can directly compute the subreflector offset causing the imbalance from the beam cut profiles.

Figure 23 (left) shows the calculated beam offset as a function of subreflector offset. From this, we calculate that an 8mm offset should result in an 128 arcsecond offset of the beam. The referenced pointing solutions from the holography observations gave 2.0 arcminutes for both the lateral and vertical displacements, in excellent agreement with the model.

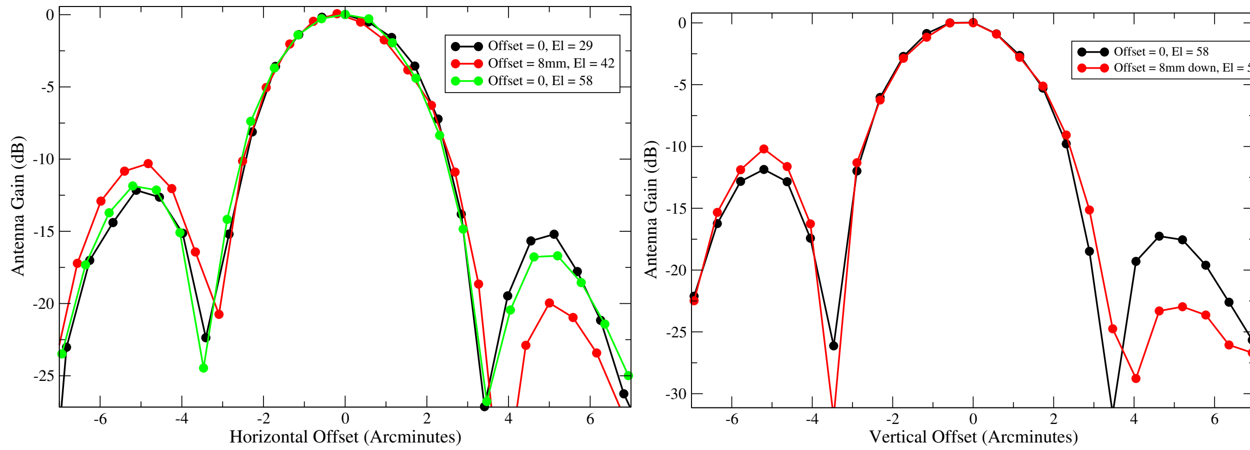

Figure 27: Results from the nudge tests, taken at Ka-band in August, 2017. (Left) Horizontal cuts through the beam with, and without an 8mm lateral offset to the left. The beam is offset to the right by 2 arcminutes, and a coma lobe appears on the left side. (Right) Vertical cuts through the beam with and without an 8mm downward offset. The beam is raised by 2 arcminutes, and a coma lobe appears on the lower side.

We conclude that the Ruze model beam predictions are an excellent match to VLA beam distortions caused by small displacements of the subreflector, so that we can directly relate the beam asymmetries to offsets in the subreflector or feeds.

10 Appendix

Listed here are all the observations utilized in this memo, arranged by band and date. All these observations are backed up on an external drive. The 'SlotID' column refers to the AIPS SlotID number in the catalog on this disk. All data have been backed up as 'FITS' files, and stored under /stash/users/rperley/SubCuts180. The data, in AIPS format, are backed up on my personal dismountable drive 'N'.

Table 11: Observing Log for C-Band Observations

Date	SlotID	RefAnt	Out	El	Nature	Target	Conf	Comments
25-Jul-2017	1	1 9 23	15	66	Az+El	3C345	C	
28-Jul-2017	2	6	15	60	Az+El	3C345	C	Subr. Rotation Off
28-Jul-2017	3	6	15	39	Az+El	3C345	C	
01-Aug-2017	4	many	15	30	Az	J0217	C	Prep. for Nudge Tests
02-Aug-2017	5	many	4 14 15 17	46	Az	3C84	C	ea20 sub 8mm left
02-Aug-2017	6	many	15	56	El	J1220	C	ea20 sub 8mm down
10-Aug-2017	7	3 4 9	15	54	Az+El	3C345	C	check ea20 sub
31-May-2018	8	5 9 19	17	56	Az+El	3C273	A	
22-Nov-2020	197	13 17 21	22	22	Az+El	3C84	B→A	
25-Nov-2020	203	13 17 21	22	75	Az+El	3C84	B→A	
25-Nov-2020	209	13 17 21	22	50	Az+El	3C84	B→A	
30-Nov-2020	212	13 17 21	22	112	Az+El	3C84	B→A	
04-Mar-2021	227	1 14 20	12,23	53	Az+El	3C273	A→D	
09-Mar-2021	233	1 14 20	23	54	Az+El	3C273	A→D	
15-Jun-2021	240	10 11 28	25 26	54	Az+El	3C273	C	

Table 12: Observing Log for X-Band Observations

Date	SlotId	RefAnts	Out	El	Nature	Target	Conf	Comments
25-Jul-2017	9	1 9 23	15	64	Az+El	3C345	C	
28-Jul-2017	10	6	15	35	Az+El	3C345	C	Subreflector Rotation Off
28-Jul-2017	11	6	15	57	Az+El	3C345	C	
01-Aug-2017	12	many	15	29	Az	J0217	C	Prepare for Nudge Tests
02-Aug-2017	13	many	4 14 15 17	44	Az	3C84	C	ea20 sub 8mm left
02-Aug-2017	14	many	15	57	El	J1220	C	ea20 sub 8mm down
04-Aug-2017	15	many	15	59	Az+El	3C84	C	check sub return
10-Aug-2017	16	3 4 9	15	50	Az+El	3C345	C	
10-Aug-2017	17	3 4 9	15	52	3-Rot	3C273	C	Test of 3-Rot
10-Aug-2017	18	3 4 9	5 15	57	3-Rot	3C273	C	Test of 3-Rot
11-Aug-2017	19	3 4 9	15	56	3-Rot	3C345	C	Test of 3-Rot
31-May-2018	20	5 9 19	17	55	Az+El	3C273	A	
23-Jul-2019	21	9 13 16	7 19 26	29	Az+El	3C84	B→A	Oversampled
25-Jul-2019	22	9 13 16	7 19	var	El	3C84	B→A	Seven elevations
29-Jul-2019	23	11 24	7 19 27	51	Az+El	3C273	B→A	
29-Jul-2019	24	11 24	7 19 27	42	Az+El	3C273	B→A	
29-Jul-2019	25	11 24	7 19 27	26	Az+El	3C84	B→A	
29-Jul-2019	26	11 24	7 19 27	40	Az+El	3C84	B→A	
30-Jul-2019	27	11 24	7 19	50	Az+El	3C273	B→A	
27-Jan-2020	28	11 24 27	9 14	57	Az+El	3C273	D	
30-Jan-2020	29	10 21 25 28	8 9	57	Az+El	3C273	D→C	
26-Feb-2020	30	10 25 28	1	58	Az+El	3C273	C	
22-Nov-2020	192	13 17 21	22	40	Az+El	3C84	B→A	
25-Nov-2020	198	13 17 21	22	79	Az+El	3C84	B→A	
25-Nov-2020	204	13 17 21	22	69	Az+El	3C84	B→A	
30-Nov-2020	210	13 17 21	22	108	Az+El	3C84	B→A	
04-Mar-2021	228	1 14 20	12,23	55	Az+El	3C273	A→D	
09-Mar-2021	234	1 14 20	23	56	Az+El	3C273	A→D	
15-Jun-2021	241	10 11 28	25 26	54	Az+El	3C273	C	

Table 13: Observing Log for Ku-Band Observations

Date	SlotID	Refants	Out	El	Nature	Target	Conf	Comments
25-Jul-2017	31	1 9 23	15	61	Az+El	3C345	C	
28-Jul-2017	32	6	15	32	Az+El	3C345	C	Subr. Rotation Off
28-Jul-2017	33	6	15	52	Az+El	3C345	C	
01-Aug-2017	34	many	15	29	Az	J0217	C	Prep for Nudge Tests
02-Aug-2017	35	many	4 14 15 17	43	Az	3C84	C	ea20 sub 8mm left
02-Aug-2017	36	many	15	57	El	J1220	C	ea20 sub 8mm down
04-Aug-2017	37	many	15	55	Az+El	3C84	C	check sub return
10-Aug-2017	38	3 4 9	15	47	Az+El	3C345	C	
15-Aug-2017	39	3 4 8	15	50	3-Rot	3C345	C	
31-May-2018	40	5 9 19	17	53	Az+El	3C273	A	
01-Jun-2018	41	3 4 9	17	56	3-Rot	3C273	A	
07-Jun-2018	42	5 9 19	17	80	3-Rot	BLLac	A	
09-Jun-2018	43	5 9 19	1 17	18	3-Rot	J0217	A	
11-Sep-2018	44	3 4 9	5 17 19 27	52	3-Rot	3C273	A	
11-Sep-2018	45	3 4 9	5 17 19 27	43	3-Rot	3C273	A	
12-Sep-2018	46	3 4 9	5 22 27	52	3-Rot	3C273	A	
13-Sep-2018	47	3 4 9	5 25 27	35	3-Rot	3C273	A	
30-May-2019	48	5 9 19	8 18	47	3-Rot	J0217	B	
31-May-2019	49	3 4 9	8	86	3-Rot	3C286	B	
31-May-2019	50	3 4 9	8	19	3-Rot	J0217	B	
01-Jul-2019	51	3 4 6 7	19 27	24 78	El	J0217, 3C345	BnA	
17-Jul-2019	52	3 6 16	5 19 25 27	var	El	many	BnA	Four elevations
18-Jul-2019	53	3 6 16	5 8 19 27	var	El	var	B→A	Four Elevations
18-Jul-2019	54	11 13 23	5 19 25 27	50	El	3C84	B→A	
23-Jul-2019	55	9 13 16	7 19 26	65	Az+El	3C84	B→A	Oversampled
25-Jul-2019	56	9 13 16	7 19	var	El	3C84	B→A	Seven Elevations
29-Jul-2019	57	11 24	7 19 27	50	Az+El	3C273	B→A	
29-Jul-2019	58	11 24	7 19 27	40	Az+El	3C273	B→A	
29-Jul-2019	59	11 24	7 19 27	27	Az+El	3C83	B→A	
29-Jul-2019	60	11 24	7 19 27	42	Az+El	3C83	B→A	
30-Jul-2019	61	11 24	7 19	48	Az+El	3C273	B→A	
27-Jan-2020	62	11 24 27	9 14	58	Az+El	3C273	D	
30-Jan-2020	63	10 21 25 28	8 9	58	Az+El	3C273	D→C	
26-Feb-2020	64	10 25 28	1	58	Az+El	3C273	C	
20-Mar-2020	65	21 25 28	1	31	Az+El	3C273	C	
29-Mar-2020	66	21 28	24	80	Az+El	3C345	C	
29-Mar-2020	67	21 25 28	24	58	Az+El	3C273	C	
23-Apr-2020	68	7 8 11	all in	57	Az+El	3C273	C	Zero-Points Adjusted
17-May-2020	69	4 13 16	2 19	46	Az+El	3C454.3	C	Zero-Points Adjusted
11-Jul-2020	70	20 23 26	3	51	Az+El	3C345	B	
22-Nov-2020	193	13 17 21	22	36	Az+El	3C84	B→A	
25-Nov-2020	199	13 17 21	22	81	Az+El	3C84	B→A	
25-Nov-2020	205	13 17 21	22	66	Az+El	3C84	B→A	
30-Nov-2020	211	13 17 21	22	105	Az+El	3C84	B→A	
20-Feb-2021	219	7 8 11	all in	58	Az+El	3C273	A	
25-Feb-2021	226	17 24 27	23	57	Az+El	3C273	A	
04-Mar-2021	229	1 14 20	12,23	56	Az+El	3C273	A→D	
09-Mar-2021	235	1 14 20	23	57	Az+El	3C273	A→D	
10-Mar-2021	239	3 16 17	10 12 23	30 58 83	Az+El	3C273 3C286 J0217	A→D	
15-Jun-2021	242	10 11 28	25 26	54	Az+El	3C273	C	

Table 14: Observing Log for K-Band Observations

Date	SlotID	Refants	OutAnts	Elev	Nature	Target	Conf	Comments
28-Jul-2017	71	6	15	49	Az+El	3C345	C	Subr Rot Off
28-Jul-2017	72	6	15	30	Az+El	3C345	C	
01-Aug-2017	73	many	15	28	Az	J0217	C	Prep for Nudge Tests
02-Aug-2017	74	many	4 14 15 17	41	Az	3C84	C	ea20 sub 8mm left
02-Aug-2017	75	many	15	58	El	J1220	C	ea20 sub 8mm down
10-Aug-2017	76	3 4 9	15	44	Az+El	3C345	C	
15-Aug-2017	77	3 4 8	15	40	3-Rot	3C345	C	
31-May-2018	78	5 9 19	17	51	Az+El	3C273	A	
01-Jun-2018	79	3 4 9	17	50	3-Rot	3C273	A	
08-Jun-2018	80	5 9 19	1 17	79	3-Rot	BLLac	A	
09-Jun-2018	81	5 9 19	1 17	18	3-Rot	J0217	A	
28-May-2019	82	5 9 19	8 18 23	49	3-Rot	J0217	B	
30-May-2019	83	5 9 19	8 18	77	3-Rot	J0217	B	
30-May-2019	84	3 4 9	8 18	18	3-Rot	J0217,3C286	B	
01-Jun-2019	85	3 4 9	8	22	3-Rot	3C345	B	
19-Jun-2019	86	3 6 14	8 23	62	3-Rot	BlLac	B	
20-Jun-2019	87	3 6 16	8 23	50	3-Rot	BLLac	B	
20-Jun-2019	88	3 6 16	8 23	27	3-Rot	BLLac	B	
20-Jun-2019	89	3 6 16	8 23	81	3-Rot	BLLac	B	
01-Jul-2019	90	3 4 6 7	19 27	24 78	El	J0217, 3c345	BnA	
03-Jul-2019	91	3 6 16	19 27	23	3-Rot	3C84	BnA	Rotation Off
03-Jul-2019	92	3 6 16	19 27	71	3-Rot	3C454.3	BnA	Rotation Off
03-Jul-2019	93	3 6 16	19 27	71	3-Rot	BLLac	BnA	Rotation Off
04-Jul-2019	94	11 13 16	19 27	var	El	var	BnA	4 elevations
05-Jul-2019	95	2 12 17	19	21 74	El	J0555 J1927	BnA	
17-Jul-2019	96	3 6 16	5 19 25 27	many	El	many	BnA	4 elevations
18-Jul-2019	97	3 6 16	5 8 19 27	var	El	var	B→A	4 elevations
18-Jul-2019	98	11 13 23	5 19 25 27 51	50	El	3C84	B→A	
23-Jul-2019	99	9 13 16	7 19 26	24	Az+El	3C84	B→A	Oversampled
25-Jul-2019	100	9 13 16	7 19	var	El	3C84	B→A	7 Elevations
29-Jul-2019	101	11 24	7 19 27	49	Az+El	3C273	B→A	
29-Jul-2019	102	11 24	7 19 27	38	Az+El	3C273	B→A	
29-Jul-2019	103	11 24	7 19 27	29	Az+El	3C84	B→A	
29-Jul-2019	104	11 24	7 19 27	43	Az+El	3C84	B→A	
30-Jul-2019	105	11 24	7 19	45	Az+El	3C273	B→A	
27-Jan-2020	106	11 24 27	9 14	57	Az+El	3C273	D	
30-Jan-2020	107	10 21 25 28	8 9	58	Az+El	3C273	D→C	
26-Feb-2020	108	10 25 28	1	57	Az+El	3C273	C	
20-Mar-2020	109	21 25 28	1	26	Az+El	3C273	C	
29-Mar-2020	110	21 28	24	83	Az+El	3C345	C	
29-Mar-2020	111	21 25 28	24	58	Az+El	3C273	C	
23-Apr-2020	112	7 8 11	all in	58	Az+El	3C273	C	Zero-Pts Adj
17-May-2020	113	4 13 16	2 19	50	Az+El	3C454.3	C	Zero-Pts Adj
11-Jul-2020	114	20 23 26	3	55	Az+El	3C345	B	
22-Nov-2020	194	13 17 21	22	32	Az+El	3C84	B→A	
25-Nov-2020	200	13 17 21	22	82	Az+El	3C84	B→A	
25-Nov-2020	206	13 17 21	22	62	Az+El	3C84	B→A	
03-Dec-2020	213	9 16 17	4 8 13 21 22	106	Az+El	3C345	B→A	
03-Dec-2020	216	9 16 17	4 8 13 21 22	60	Az+El	3C345	B→A	
20-Feb-2021	220	7 8 11		58	Az+El	3C273	A	
25-Feb-2021	225	17 24 27	23	58	Az+El	3C273	A	
04-Mar-2021	230	1 14 20	12,23	57	Az+El	3C273	A→D	
09-Mar-2021	236	1 14 20	23	58	Az+El	3C273	A→D	
15-Jun-2021	243	10 11 28	25 26	54	Az+El	3C273	C	

Table 15: Observing Log for Ka-Band Observations

Date	SlotID	RefAnts	OutAnts	El	Nature	Target	Conf	Comments
28-Jul-2017	115	6	15	46	Az+El	3C345	C	Subr Rotation Off
28-Jul-2017	116	6	15	26	Az+El	3C345	C	
01-Aug-2017	117	many	15	28	Az	J0217	C	Prep for Nudge Tests
02-Aug-2017	118	many	4 14 15 17	39	Az	3C84	C	ea20 sub 8mm left
02-Aug-2017	119	many	15	58	El	J1220	C	ea20 sub 8mm down
10-Aug-2017	120	3 4 9	15	40	Az+El	3C345	C	
17-Aug-2017	121	3 4 9	3 15	48	3-Rot	3C345	C	Incomplete
18-Aug-2017	122	3 4 9	15	55	3-Rot	3C345	C	
31-May-2018	123	5 9 19	17	49	Az+El	3C273	A	
02-Jun-2018	134	3 4 9	19	51	3-Rot	3C273	A	
08-Jun-2018	125	5 9 19	1 17	80	3-Rot	BLLac	A	
10-Jun-2018	126	5 9 19	1 17	18	3-Rot	J0217	A	
01-Jun-2019	127	9 12 19	8	57	3-Rot	3C273,	B	
01-Jun-2019	128	9 12 19	8	83	3-Rot	3C286	B	
06-Jun-2019	129	9 12 19	8	30	3-Rot	3C345	B	
07-Jun-2019	130	9 12 19	8	54	3-Rot	3C273	B	
07-Jun-2019	131	9 12 19	8	70	3-Rot	3C286	B	
21-Jun-2019	132	5 9	8 19	80	3-Rot	BlLac	B	
24-Jun-2019	133	3 6 16	19	49	3-Rot	J1927	B	
24-Jun-2019	134	3 6 16	19	26	3-Rot	J1153	B	
24-Jun-2019	135	3 6 16	19	77	3-Rot	BLLac	B	
01-Jul-2019	136	3 4 6 7	19 27	24 78	El	J0217, 3c345	BnA	
05-Jul-2019	137	2 12 17	19	21 74	El	J0555 J1927	BnA	
17-Jul-2019	138	3 6 16	5 19 25 27	many	El	many	BnA	Four elevations
18-Jul-2019	139	3 6 16	5 8 19 27	var	El	var	B→A	Four elevations
18-Jul-2019	140	11 13 23	5 19 25 27	49	El	3C84	B→A	
25-Jul-2019	141	9 13 16	7 19	var	El	3C84	B→A	Seven elevations
29-Jul-2019	142	11 24	7 19 27	36	Az+El	3C273	B→A	
29-Jul-2019	143	11 24	7 19 27	31	Az+El	3C273	B→A	
29-Jul-2019	144	11 24	7 19 27	47	Az+El	3C84	B→A	
29-Jul-2019	145	11 24	7 19 27	45	Az+El	3C84	B→A	
30-Jul-2019	146	11 24	7 19	42	Az+El	3C273	B→A	
27-Jan-2020	147	11 24 27	9 14	57	Az+El	3C273	D	
30-Jan-2020	148	10 21 25 28	8 9	58	Az+El	3C273	D→C	
26-Feb-2020	149	10 25 28	1	58	Az+El	3C273	C	
20-Mar-2020	150	21 25 28	1	25	Az+El	3C273	C	
29-Mar-2020	151	21 28	24	82	Az+El	3C345	C	
29-Mar-2020	152	21 25 28	24	58	Az+El	3C273	C	
23-Apr-2020	153	7 8 11	all in	57	Az+El	3C273	C	Zero-Pts Adj
17-May-2020	154	4 13 16	2 19	50	Az+El	3C454.3	C	Zero-Pts Adj
11-Jul-2020	155	20 23 26	3	55	Az+El	3C345	B	
22-Nov-2020	195	13 17 21	22	30	Az+El	3C84	B→A	
25-Nov-2020	201	13 17 21	22	82	Az+El	3C84	B→A	
25-Nov-2020	207	13 17 21	22	58	Az+El	3C84	B→A	
03-Dec-2020	214	9 16 17	4 8 13 21 22	102	Az+El	3C345	B→A	
03-Dec-2020	217	9 16 17	4 8 13 21 22	64	Az+El	3C345	B→A	
20-Feb-2021	221	7 8 11		58	Az+El	3C273	A	
25-Feb-2021	224	17 24 27	23	58	Az+El	3C273	A	
04-Mar-2021	231	1 14 20	12,23	58	Az+El	3C273	A→D	
09-Mar-2021	237	1 14 20	23	58	Az+El	3C273	A→D	
15-Jun-2021	244	10 11 28	25 26	54	Az+El	3C273	C	

Table 16: Observing Log for Q-Band Observations

Date	SlotID	RefAnts	OutAnts	El	Nature	Target	Conf	Comments
28-Jul-2017	156	6	15	44	Az+El	3C345	C	Subr Rot Off
28-Jul-2017	157	6	15	24	Az+El	3C345	C	
01-Aug-2017	158	many	15	28	Az	J0217	C	Prep for Nudge Tests
02-Aug-2017	159	many	4 14 15 17	38	Az	3C84	C	ea20 sub 8mm left
02-Aug-2017	160	many	15	58	El	J1220	C	ea20 sub 8mm down
10-Aug-2017	161	3 4 9	15	37	Az+El	3C345	C	
17-Aug-2017	162	3 4 9	15	51	3-Rot	3C345	C	Incomplete
18-Aug-2017	163	3 4 9	15	42	Az+El	3C345	C	
31-May-2018	164	5 9 19	17	46	Az+El	3C273	A	
02-Jun-2018	165	3 4 9	17	40	3-Rot	3C273	A	
07-Jun-2018	166	5 9 19	17	80	3-Rot	BLLac	A	
10-Jun-2018	167	5 9 19	1 2 17	18	3-Rot	J0217	A	
03-Jun-2019	168	9 12 19	8 20	22	3-Rot	3C345	B	
03-Jun-2019	169	9 12 19	8 20	57	3-Rot	3C273	B	
03-Jun-2019	170	9 12 19	8 20	84	3-Rot	3C286	B	
04-Jun-2019	171	9 12 19	8 22	34	3-Rot	3C84	B	
04-Jun-2019	172	9 12 19	8 22	40	3-Rot	J1927	B	
24-Jun-2019	173	3 6 16	6 15 19 22 24	68	3-Rot	3C84	B	
25-Jun-2019	174	3 6 16	19	49	3-Rot	J1153	B	
25-Jun-2019	175	3 6 16	19	26	3-Rot	J1927	B	
25-Jun-2019	176	3 6 16	19	77	3-Rot	BLLac	B	
01-Jul-2019	177	3 4 6 7	19 27	24 78	El	J0217, 3c345	BnA	
17-Jul-2019	178	3 6 16	5 19 25 27	many	El	many	BnA	Fourelevations
18-Jul-2019	179	3 6 16	5 8 19 27	var	El	var	B→A	Four elevations
18-Jul-2019	180	11 13 23	5 19 25 27	48	El	3C84	B→A	
25-Jul-2019	181	9 13 16	7 19	var	El	3C84	B→A	Seven elevations
27-Jan-2020	182	11 24 27	9 14	57	Az+El	3C273	D	
30-Jan-2020	183	10 21 25 28	8 9	58	Az+El	3C273	D→C	
26-Feb-2020	184	10 25 28	1	58	Az+El	3C273	C	
20-Mar-2020	185	21 25 28	1	25	Az+El	3C273	C	
29-Mar-2020	186	21 28	24	82	Az+El	3C345	C	
29-Mar-2020	187	21 25 28	24	58	Az+El	3C273	C	
23-Apr-2020	188	7 8 11	all in	57	Az+El	3C273	C	Zero-Pts Adj
17-May-2020	189	4 13 16	2 19	50	Az+El	3C454.3	C	Zero-Pts Adj
11-Jul-2020	190	20 23 26	3	55	Az+El	3C345	B	
22-Nov-2020	196	13 17 21	22	26	Az+El	3C84	B→A	
25-Nov-2020	202	13 17 21	22	79	Az+El	3C84	B→A	
25-Nov-2020	208	13 17 21	22	54	Az+El	3C84	B→A	
03-Dec-2020	215	9 16 17	4 8 13 21 22	98	Az+El	3C345	B→A	
03-Dec-2020	218	9 16 17	4 8 13 21 22	68	Az+El	3C345	B→A	
20-Feb-2021	222	7 8 11		57	Az+El	3C273	A	
25-Feb-2021	223	17 24 27	23	57	Az+El	3C273	A	
04-Mar-2021	232	1 14 20	12,23	58	Az+El	3C273	A→D	
09-Mar-2021	238	1 14 20	23	58	Az+El	3C273	A→D	
15-Jun-2021	245	10 11 28	25 26	54	Az+El	3C273	C	